

RHODES UNIVERSITY



**Observations of cosmic re-ionisation with
the Hydrogen Epoch of Reionization
Array: simulations of closure phase spectra**

by

Ntsikelelo Charles

Submitted in fulfillment of the
academic requirements for the degree of

Masters

in

Physics

Rhodes University, Makanda

Supervised by Prof. O. M. Smirnov, Prof. G. Bernardi & Dr. L. Bester

March 12, 2021

Now unto him that is able to do exceeding abundantly above all that we ask or think, according to the power that worketh in us.

~Ephesians 3:20

For in him we live and move and have our being.

~Acts 17:28

Declaration of Non-Plagiarism

I, **Ntsikelelo Charles** declare that

1. The research reported in this thesis, except where otherwise indicated, is my original research.
2. This thesis has not been submitted for any degree or examination at any other university.
3. This thesis does not contain other persons' data, pictures, graphs or other information, unless specifically acknowledged as being sourced from other persons.
4. This thesis does not contain other persons' writing, unless specifically acknowledged as being sourced from other researchers.

Abstract

The 21 cm transition from neutral Hydrogen promises to be the best observational probe of the Epoch of Reionisation. It has driven the construction of the new generation of low frequency radio interferometric arrays, including the Hydrogen Epoch of Reionization Array (HERA). The main difficulty in measuring the 21 cm signal is the presence of bright foregrounds that require very accurate interferometric calibration. [Thyagarajan et al. \(2018\)](#) proposed the use of closure phase quantities as a means to detect the 21 cm signal, which has the advantage of being independent (to first order) from calibration errors and therefore, bypasses the need for accurate calibration. Closure phases are, however, affected by so-called direction dependent effects, e.g. the fact that the dishes - or antennas - of an interferometric array are not identical to each other and , therefore, yield different antenna primary beam responses.

In this thesis, we investigate the impact of direction dependent effects on closure quantities and simulate the impact that primary antenna beams affected by mutual coupling have on the foreground closure phase and its power spectrum i.e. the power spectrum of the bispectrum phase ([Thyagarajan et al., 2020](#)). Our simulations show that primary beams affected by mutual coupling lead to an overall leakage of foreground power in the so-called EoR window, i.e. power from smooth-spectrum foregrounds is confined to low k modes. We quantified this effect and found that the leakage is up to ~ 8 orders magnitude higher than the case of an ideal beam at

$k_{\parallel} > 0.5 h \text{ Mpc}^{-1}$. We also found that the foreground leakage is worse when edge antennas are included, as they have a more different primary beam compared to antennas at the centre of the array. The leakage magnitude is worse when bright foregrounds appear in the antenna sidelobes, as expected.

Our simulations provide a useful framework to interpret observations and assess which power spectrum region is expected to be most contaminated by foreground power leakage.

Acknowledgments

“The Lord is my strength and my shield; My heart trusts in Him, and I am helped ~Psalms 28:7”

This note of thanks is the final touch on my dissertation dedicated to all those whose paths have crossed mine. I want to reflect on the people who supported and helped me throughout my Masters journey.

I thank my supervisors, Prof. Oleg Smirnov, Prof. Gianni Bernardi and Dr Landman Bester for their sound advice, inspiration and encouragements.

The financial assistance of the South African Radio Astronomy Observatory (SARAO) towards this research is hereby acknowledged (www.sarao.ac.za).

I thank the staff of the Rhodes University Physics and Electronics department. My sincere gratitude goes to my colleagues, members of the RATT team and for all their support, discussions, reviews and engaging arguments which gave this work a perfect finish.

Finally, I thank my family for all their support and encouragement.

Contents

Declaration of Non Plagiarism	i
Declaration of Publications	ii
Abstract	ii
Acknowledgments	iv
1 INTRODUCTION	1
2 The Epoch of Re-ionisation	4
2.1 Brief introduction to cosmology	4
2.1.1 Cosmological distances	5
2.1.2 Dynamics of the Universe	5
2.1.3 Comoving distance in a flat Universe	7
2.2 Thermal history of the early Universe	9
2.3 Formation of cosmic structures	10
2.4 Statistical description of cosmic structures	11

2.4.1	Correlation function and the power spectrum	12
2.5	The 21 cm emission from the EoR	13
2.5.1	Cosmology with the 21 cm signal	14
2.5.2	Spatial fluctuations of the 21 cm signal	17
2.6	Current status of observations	19
2.7	The Hydrogen Epoch of Reionization Array	20
3	Observations of the EoR with Closure Phase Quantities	25
3.1	Review of Radio Interferometry and Calibration	25
3.1.1	Van Cittert-Zernike Theorem	26
3.1.2	The Radio Interferometry Measurement Equation (RIME)	27
3.1.3	Direction Independent Effects	28
3.1.4	Direction Dependent Effects	29
3.1.5	Calibration	31
3.2	Power spectrum of the 21 cm signal from inteferometric observations	32
3.3	Foregrounds: an overview	35
3.3.1	Galactic synchrotron emission	35
3.3.2	Extra-galactic foregrounds	37
3.4	Foreground mitigation methods	38
3.4.1	Foreground subtraction	38
3.4.2	Foreground avoidance	39
3.5	Detection of the 21 cm signal using the power spectrum of the bi-spectrum phase	41
3.6	Thesis motivation	44
4	Simulations of foreground closure spectra	47
4.1	Closure spectra of sky models	47
4.2	Closure spectra simulations with direction independent effects	53
4.3	Closure spectra simulations with direction dependent effects	53

5	Simulations of foreground bi-spectrum phase using mutual coupling beams	59
5.1	Simulations with perturbed primary beam	62
5.2	Power spectrum simulations with mutual coupling beams	69
5.3	Power spectrum simulations with realistic foregrounds and mutual coupling beams	74
6	Conclusions	82

CHAPTER 1

INTRODUCTION

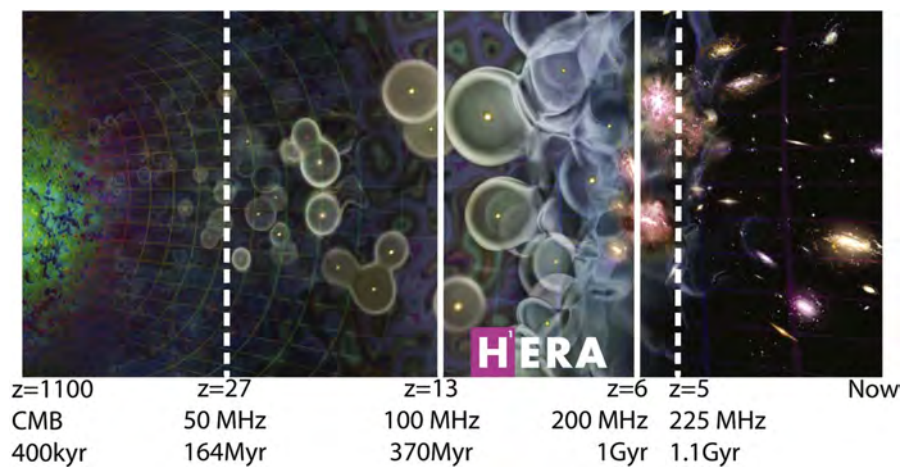


Figure 1.1: Cartoon representation of the cosmic evolution with landmarks corresponding to the most significant transitions in the intergalactic medium (image credit Loeb/Scientific American, taken from [DeBoer et al., 2017](#))

The detection of the redshifted 21 cm emission line from neutral Hydrogen during the Epoch of Reionisation is one of the main goals of (upcoming) low frequency radio telescopes like the

Low-Frequency Array (LOFAR) (Van Haarlem et al., 2013), the Hydrogen Epoch of Reionisation Array (HERA) (DeBoer et al., 2017) and the Square Kilometre Array (SKA) (Koopmans et al., 2015). The Epoch of Reionisation (EoR) is one of the least known areas of cosmology, from an observational point of view. Advancing our understanding of the reionisation will enable us to understand how the first galaxies formed and, ultimately, improve constraints on cosmological parameters (Park et al., 2019, e.g.,).

The Universe was initially dense and hot, with temperatures as high as 10^{32} K (Bennett, 2007). Shortly afterwards, the Universe underwent an exponential expansion (Linde, 2007). After 380000 years $z \approx 1100$, the temperature cooled down sufficiently for neutral hydrogen to form (Fig 1.1). Before Hydrogen recombination, the Universe was opaque to radiation as free electrons caused the light to scatter. After recombination, the Universe became transparent, and photons could travel freely: this is the cosmic microwave background (CMB) radiation that is detected in all directions with an average temperature signal of ~ 2.7 K (Fixsen, 2009).

Measurements of CMB anisotropies (e.g., Mather et al., 1994; Bennett et al., 2013; Planck Collaboration et al., 2018), provide the best constraints on cosmological parameters, however, as the CMB photons no longer interact significantly with the matter after recombination, they do not provide detail information about the formation of the first stars and galaxies.

Cosmological simulations predict first stars and galaxies to form at $z \approx 30$, which, in turn, emitted electromagnetic radiation that heated and, later, ionised the Inter Galactic Medium (IGM) (e.g., Mesinger et al., 2011).

The hyperfine transition from neutral Hydrogen is the most promising probe of structure formation, imprinted in the intergalactic medium. Measurements of the 21 cm signal are challenged by the presence of foreground emission from the Galaxy and extra-galactic sources, which are orders of magnitude brighter (Bernardi et al., 2009). The foreground radiation is mainly constituted by synchrotron radiation and, therefore, smooth with frequency. This is in contrast with the 21 cm emission line which fluctuates rapidly (e.g., Santos et al., 2005). High accuracy in calibration is therefore required in order not to compromise the foreground spectral smoothness (e.g., Wang et al., 2013; Chapman et al., 2014; Sims et al., 2016).

The need for high accuracy calibration required for foreground subtraction has led to alternate

methods, known as *foreground avoidance methods*. As the name suggests, the idea is to avoid the foreground emission rather than subtracting it (e.g., [Parsons et al., 2012](#); [Thyagarajan et al., 2013](#)). The *delay spectrum* is one such method; it makes use of interferometric delays to isolate the power spectrum of the 21 cm emission. Due to the spectral nature of the 21 cm signal, its power spectrum appears at all k modes, whereas the foreground emission is limited to a wedge like region in k -space ([Thyagarajan et al., 2013](#); [Pober et al., 2013](#)).

Yet another alternative method that uses closure quantities was proposed by [Thyagarajan et al. \(2018\)](#). The use of closure phases mitigates the calibration requirements as closure quantities are independent of antenna based corruptions. Closure phase quantities, however, are affected by direction-dependent effects such as varying antenna primary beam responses. In this thesis, we aim to study the impact of antenna primary beams, which are affected by mutual coupling on closure phase quantities.

CHAPTER 2

The Epoch of Re-ionisation

2.1 Brief introduction to cosmology

Cosmology is the study of the origin and evolution of the Universe. The Big Bang theory forms a crucial part of modern cosmology. The Universe was initially thought to be static, however, upon observing the emission spectra of distant galaxies, Edward Hubble noted that their spectral lines appear to be redshifted, i.e. the observed spectra appeared at frequencies lower than their rest frame. Redshift is defined as:

$$z = \frac{\lambda_o - \lambda_r}{\lambda_r}, \quad (2.1)$$

where λ_o and λ_r are the observed and rest frame wavelengths respectively. Edward Hubble also noted that galaxies further away were much more red-shifted than closer galaxies. From this, he concluded that all galaxies were receding from each other and that the velocity of the recession is proportional to the physical distance between the galaxies. This formulated the famous *Hubble law* (Hubble, 1929):

$$v = H_0 r, \quad (2.2)$$

where v is the recession velocity, H_0 is the Hubble constant and r is the distance. The current value of the Hubble constant is dispute between the value obtained from supernovae, $H_0 = 74.24 \pm 1.82 \text{ km s}^{-1} \text{ Mpc}^{-1}$ (Riess et al., 2019), and the CMB measurements, $H_0 = 67.4 \pm 0.5 \text{ km s}^{-1} \text{ Mpc}^{-1}$ (Planck Collaboration et al., 2018). The Hubble constant is therefore normally expressed as:

$$H_0 = 100h \text{ km s}^{-1} \text{ Mpc}^{-1}, \quad (2.3)$$

where h is parameterisation factor.

2.1.1 Cosmological distances

There are two distances that are commonly used in cosmology; the *comoving* and the *proper* distance. Comoving distances are distances measured in the frame comoving with the Universe's expansion, whereas proper distances are measured by specific observers (us for example) and therefore, change with the Universe's expansion. The proper distance r is related to the comoving distance x as:

$$r(t) = a(t)x, \quad (2.4)$$

where $a(t)$ is the expansion factor. The expansion factor is normalised to unity today, i.e. $a_0 = 1$.

The redshift z can be related to expansion coefficient as:

$$1 + z \propto \frac{1}{a(t)}. \quad (2.5)$$

2.1.2 Dynamics of the Universe

In cosmology, the Universe is assumed to be homogeneous and isotropic on large scales. With this assumption, the Universe in general relativity is described as a *perfect fluid*. The metric describing the space-time of the Universe is the *Friedmann-Lemaître-Robertson-Walker metric* defined as:

$$ds^2 = c^2 dt^2 - a^2 \left[\frac{dx^2}{1 - Kx^2} + x^2(d\theta^2 + \sin^2 \theta d\phi^2) \right], \quad (2.6)$$

where x, θ and ϕ are the comoving spherical coordinates. The curvature parameter K takes only three values $+1, 0$ and -1 . The different allowed values of K describe the different possible space-time geometries.

- when $K = +1$, the space-time geometry is a sphere, which represents a *Closed Universe*
- when $K = 0$, the space-time geometry is Euclidean, which represents a *Flat Universe*
- when $K = -1$, the space-time geometry is a hyperboloid, which represents an *Open Universe*

The *Hubble parameter* $H(t)$ is defined in cosmology as:

$$H(t) = \frac{\dot{a}(t)}{a(t)}, \quad (2.7)$$

where $\dot{a}(t)$ denotes the time derivative of $a(t)$ and $H(t_0) = H_0$.

The general solutions to the Einstein's equations describing the expansion of the Universe are given by *Friedmann equations* (Smeenk & Ellis, 2017) and can be expressed in terms of the expansion coefficient a :

$$\dot{a}^2 = \frac{8\pi G\rho}{3}a^2 - Kc^2 \quad (2.8)$$

and

$$\ddot{a} = -\frac{4\pi G}{3}\left(\rho + \frac{3p}{c^2}\right)a, \quad (2.9)$$

where G is the gravitational constant, ρ and p are the energy density and the pressure of the fluid respectively, K is the curvature parameter and c is the speed of light. By introducing a *critical density* of the Universe defined ρ_c as:

$$\rho_c(t) = \frac{3H^2(t)}{8\pi G}. \quad (2.10)$$

and a *density parameter*

$$\Omega(t) = \frac{\rho(t)}{\rho_c(t)}. \quad (2.11)$$

Friedmann's equations can be written as:

$$H^2(1 - \Omega)a^2 = -Kc^2. \quad (2.12)$$

The perfect fluid is made up of three main components.

- *Matter*. This is a non-relativistic fluid made of baryonic matter and non-baryonic dark matter. The pressure exerted by matter is nearly negligible $p \approx 0$ and its density ρ_m evolves as:

$$\rho_m = \rho_{0,m} (1 + z)^3, \quad (2.13)$$

where $\rho_{0,m}$ is the matter density at present time.

- *Radiation*. This relativistic fluid made of non-degenerate particles, such as photons or neutrinos, with a pressure given by:

$$p_\gamma = \frac{1}{3} \rho_\gamma c^2; \quad (2.14)$$

where ρ_γ is the radiation density.

- *Dark Energy*. This is an exotic fluid associated with a cosmological constant Λ , which has a pressure given by:

$$p_\Lambda = -\rho_\Lambda c^2. \quad (2.15)$$

The negative pressure means that it can produce an accelerated expansion of the Universe since $\ddot{a} > 0$ (see equation 2.9).

2.1.3 Comoving distance in a flat Universe

Let us assume that the origin of the observer coordinate system is oriented in such a way that the path length between the two points is both constant in θ and ϕ direction. The measured distance is then given by:

$$r(t) = \int_0^x a \frac{dx'}{(1 - Kx'^2)^{1/2}} = af(x), \quad (2.16)$$

where values of the function $f(x)$ depend upon the geometry of space-time:

$$f(x) = \begin{cases} \sin^{-1} x, & \text{for } K = +1 \\ x, & \text{for } K = 0 \\ \sinh^{-1} x, & \text{for } K = -1 \end{cases} \quad (2.17)$$

Using equation 2.4, the comoving distance is therefore given by:

$$x = \frac{r(t)}{a} = f(x). \quad (2.18)$$

Now if we consider a photon emitted by a comoving source at a time t observed by an observer placed at the origin of the coordinate system. The photon travels along space-time paths satisfying the condition $ds^2 = 0$, known as *light-like paths*. Using this condition and equation 2.6 the comoving distance travelled by the photon in a flat Universe ($K = 0$), is given by:

$$x = \int_t^{t_{obs}} \frac{cdt'}{a}. \quad (2.19)$$

Using equation 2.5 and 2.7, it can be shown that the comoving distance as a function redshift z is given by:

$$x = c \int_{z_{obs}}^z \frac{dz'}{H(z')}, \quad (2.20)$$

where

$$H(z) = H_0 \sqrt{\Omega_\gamma(1+z)^4 + \Omega_m(1+z)^3 + \Omega_K(1+z)^2 + \Omega_\Lambda}, \quad (2.21)$$

where Ω_γ , Ω_m , Ω_K and Ω_Λ are the total radiation energy density, the total matter density, the dark energy density the curvature of the universe respectively. Densities are defined as:

$$\Omega_i = \frac{\rho_i}{\rho_c}, \quad (2.22)$$

where $i = \gamma, m, \Lambda$ and are such that:

$$\Omega_0 = \Omega_\gamma + \Omega_m + \Omega_\Lambda, \quad (2.23)$$

with the curvature of the universe Ω_K is given by:

$$\Omega_K = 1 - \Omega_0. \quad (2.24)$$

The most recent values of these parameters are tabulated in Table 2.1. The right-hand side of equation 2.12 is a constant, and thus we can evaluate the left-hand side at any epoch. Evaluating the left-hand side at the present time t_0 sets the value of the constant K to:

$$K = \frac{H_0^2(1 - \Omega_0)a_0^2}{c^2} = \frac{H_0^2(1 - \Omega_0)}{c^2}, \quad (2.25)$$

where $\Omega_0 = \Omega(t)$

From the measured values, it can be concluded the geometry of the Universe is flat as $\Omega_K \approx 0$, i.e $K = 0$ (see equation 2.25). The *Lambda Cold Dark Matter* (Λ CDM) is the widely accepted cosmological model, where the Universe is geometrically flat, and the dark energy component is associated with cosmological constant Λ and dark matter formation is dominated by Cold Dark Matter (CDM) component (discussed in Sect 2.3).

$\Omega_\gamma \cdot 10^5$	Ω_m	Ω_K	Ω_Λ
9.3 ± 0.2	0.315 ± 0.007	-0.009 ± 0.006	0.685 ± 0.007

Table 2.1: Density parameters from [Planck Collaboration et al. \(2018\)](#) for the Λ CDM model. All values are given at a confidence level of 68 %, except for Ω_K , which is calculated at 95 % confidence level.

2.2 Thermal history of the early Universe

The Universe is said to have originated from the Big Bang after *Planck time* $t_p \approx 10^{-43}$ s. Prior to Planck time, the Universe is very dense, and as a consequence, quantum and gravitational effects are manifest and therefore a sufficient study of the Universe before Planck time requires a theory that combines Quantum Mechanics and General Relativity, and as of yet, we do not have a solid quantum-gravity theory. However, near the Planck time at a temperature of about 10^{32} K, the Friedmann equations are valid ([Bennett, 2007](#)). At this temperature, all four interactions; gravitational force, electromagnetic force, weak and strong nuclear force are combined as one "super force" according to the Grand Unified Theory (GUT) ([Buras et al., 1978](#)). Eventually, the temperature drops below 10^{32} K, this allowed the gravitational force to separate from the other forces, and the Universe reaches a temperature of about 10^{29} K, 10^{-38} s after the Big Bang. This is followed by the separation of the electroweak (electromagnetic and weak nuclear force) and strong nuclear force, and this separation releases an enormous amount of energy in a span 10^{-36} s, causing a sudden acceleration, known as *inflation*, the Universe expanded by a factor

of $\approx 10^{60}$ (Linde, 2007). Approximately 10^{-10} s after the Big Bang, the electromagnetic force separates from the weak nuclear force and elementary particles, such as photons, gluons and quarks, are formed.

At 10^{-5} s, the temperature of the Universe reaches 10^{12} K, allowing the formation of hadrons. Proton and Neutrons begin to fuse, forming heavier nuclei, initiating *primordial nucleosynthesis* (Fuller et al., 1988). Fusion ceases at approximately 300 s after the Big Bang, at temperature of 10^9 K. Baryonic matter in the Universe at this time was made up of 75% protons, and the rest was helium nuclei and electrons with traces of lithium and deuterium. Electrons constantly scatter photons via *Thompson scattering*. The strong interaction between baryons and radiation prevents the formation of neutral atoms until the Universe is 380 000 years old, at a temperature of about 3000 K, marking the beginning of *recombination* at $z_{rec} \approx 1100$ (Kamionkowski, 2007; Bennett, 2007). During recombination, electrons bind to protons forming neutral hydrogen atoms (Peebles, 1968; Zeldovich, 1972). As a result, matter and radiation decouple and thus photons are finally able to propagate, making the Universe transparent. This relic radiation is seen today as the *Cosmic Microwave Background (CMB)* with a temperature today of $T_{0,\gamma} \approx 2.73$ K. The CMB temperature changes as a function redshift as:

$$T_{\gamma}(z) = T_{0,\gamma}(1 + z), \quad (2.26)$$

whilst the gas constituted by the newly formed neutral atoms starts to cool faster than the CMB such that the kinetic temperature T_k evolves as:

$$T_k \propto (1 + z)^2. \quad (2.27)$$

The gas thermally decouples from CMB at $z_{dec} \approx 200$.

2.3 Formation of cosmic structures

The accepted model of structure formation is based on the collapse of baryonic matter within dark matter halos. Dark matter halos are generated from the growth of small perturbations in the primordial matter density distribution of the Universe. Dark matter does not absorb, scatter or

emit electromagnetic radiation. This means we can probe its existence only through gravitational effects. The first evidence of dark matter was inferred by [Zwicky \(1933\)](#) through dynamical studies of the Coma galaxy cluster. Since then, evidence of the presence of dark matter has been supported by studies of velocity dispersions in elliptical galaxies ([Loewenstein & White, 1998](#)), rotation curves ([Fuchs, 2001](#)) and gravitational lensing ([Li et al., 2016](#)).

Currently accepted models distinguish between *Hot Dark Matter* (HDM) and *Cold Dark Matter* (CDM) depending on the thermal speed of particles at the decoupling time. In the early Universe, all particles were coupled to the radiation fluid and hence were relativistic. The time at which a particle of mass m becomes non-relativistic is given by the equilibrium condition between thermal and rest energy:

$$k_B T_\gamma = mc^2 \quad (2.28)$$

where k_B is Boltzmann's constant. Hence, more massive particles become non-relativistic before less massive ones, since T_γ scales down with redshift. This is the case for CDM. Contrary to HDM, where low mass particles, such as relativistic neutrinos form first at the decoupling time. CDM model, rather than the HDM has been observed as being the driving mechanism for dark matter formation in the Universe ([Wang et al., 2016](#)), i.e. massive dark matter particles form first. Lastly, the decoupling between radiation and a given particle is determined by the collision time scale. For dark matter particles, the interaction with photons is very small, resulting in a high collision timescale, and thus dark matter decoupling occurs well before baryonic matter and radiation decoupling, i.e. at $z \gg z_{dec}$ ([Planck Collaboration et al., 2018](#)).

2.4 Statistical description of cosmic structures

Density fluctuations of matter in the Universe can be described by the *over-density field*. The over-density field is defined as:

$$\delta(\mathbf{x}) = \frac{\rho(\mathbf{x}) - \langle \rho(\mathbf{x}) \rangle}{\langle \rho(\mathbf{x}) \rangle}, \quad (2.29)$$

where $\langle \rangle$ indicates a volume average. The over-density field $\delta(\mathbf{x})$ is the deviation of the density field $\rho(x)$ from the average $\langle \rho(\mathbf{x}) \rangle$ (also referred to as the mean background density) at some

position \mathbf{x} . Positive values of $\rho(\mathbf{x})$ describe regions that are over-dense and negative values describe are regions that are under-dense.

Perturbations in the Universe are initially small, i.e. $|\delta| \ll 1$, and they evolve in the *linear regime*. If we consider an over-dense region, i.e. where $\delta > 0$; now because of its self-gravity, the over-dense region will expand slower than the expansion of the Universe and hence the over-density will increase with time. Eventually, the over-density reaches $\delta \approx 1$, at this point, the evolution of δ can no longer be described analytically; it enters the *non-linear regime*. The over-dense region starts to collapse as a consequence of gravity and becomes a *varialised system*, a bound structure known as a *dark matter halo*. These halos form before baryon and radiation decoupling z_{dec} . This means that at z_{dec} , the baryon density perturbations follow up on dark matter perturbations, and after a certain time, they grow together.

2.4.1 Correlation function and the power spectrum

The *correlation function* of the density field $\xi(\mathbf{x})$, at a point \mathbf{x} , is a volume average product of the density fluctuations at two different points separated by a distance \mathbf{x} :

$$\xi(x) = \langle \delta(\mathbf{r})\delta(\mathbf{r} + \mathbf{x}) \rangle. \quad (2.30)$$

where $x = |\mathbf{x}|$ and the average is done over \mathbf{r} . The correlation function in this sense is a two-point auto-correlation function that describes the excess probability of finding two over-dense regions separated by distance \mathbf{x} , relative to a uniform probability distribution. The over-density function can be described in frequency space by taking a Fourier transform:

$$\delta(\mathbf{x}) = \frac{1}{(2\pi)^3} \int \tilde{\delta}(\mathbf{k}) e^{i\mathbf{k}\mathbf{x}} d^3k, \quad (2.31)$$

where \mathbf{k} is Fourier conjugate of \mathbf{x} and $\tilde{\delta}(\mathbf{k})$ is the density perturbation function given by:

$$\tilde{\delta}(\mathbf{k}) = \int \delta(\mathbf{x}) e^{-i\mathbf{k}\mathbf{x}} d^3x. \quad (2.32)$$

The *power spectrum* of over-density field is defined as:

$$P(k) \delta_D(\mathbf{k} + \mathbf{k}') (2\pi)^3 = \langle \tilde{\delta}(\mathbf{k}) \tilde{\delta}(\mathbf{k}') \rangle, \quad (2.33)$$

where $k = |\mathbf{k}|$ and δ_D is the Dirac delta function.

Substituting $\delta(\mathbf{r})$ and $\delta(\mathbf{r} + \mathbf{x})$ in equation 2.30 yields:

$$\xi(x) = \left\langle \frac{1}{(2\pi)^3} \int \tilde{\delta}(\mathbf{k}) e^{i\mathbf{k}\mathbf{r}} d^3k \frac{1}{(2\pi)^3} \int \tilde{\delta}(\mathbf{k}') e^{i\mathbf{k}'(\mathbf{r}+\mathbf{x})} d^3k' \right\rangle, \quad (2.34)$$

and with simplification

$$\xi(x) = \frac{1}{(2\pi)^6} \int d^3k \int \langle \tilde{\delta}(\mathbf{k}) \tilde{\delta}(\mathbf{k}') \rangle e^{i\mathbf{k}(\mathbf{r}+\mathbf{x}) + i\mathbf{k}'\mathbf{r}} d^3k', \quad (2.35)$$

if $\mathbf{k} = -\mathbf{k}'$, this simplifies to

$$\xi(x) = \frac{1}{(2\pi)^6} \int \langle \tilde{\delta}(\mathbf{k}) \tilde{\delta}(\mathbf{k}') \rangle e^{i\mathbf{k}\mathbf{x}} d^3k. \quad (2.36)$$

Therefore the power spectrum is related to the correlation function by a Fourier transform:

$$\xi(x) = \frac{1}{(2\pi)^3} \int P(k) e^{i\mathbf{k}\mathbf{x}} d^3k. \quad (2.37)$$

Hence, large scale fluctuations of the over-density field have their power at low spatial frequencies and small scales at high frequencies.

2.5 The 21 cm emission from the EoR

The hydrogen hyperfine transition spectral line, with a rest frame frequency of 1420 MHz (21 cm) promises to be a very useful probe for studying the evolution of the IGM during EoR (Furlanetto, 2006; Mesinger et al., 2011). The evolution of the IGM can be marked by three distinct phases. The first phase, called the *Dark Ages*, is the period of time between the thermal decoupling of the gas from CMB at $z_{dec} = 200$ and the formation of the first stars.

The second phase, known as the *Cosmic Dawn*, begins with the formation of the first stars and galaxies at $z \approx 20 - 30$. Radiation from first stars and galaxies initially heated the IGM. However, as the star formation process continued, the radiation began to ionise the IGM, this marked the beginning of the third phase, *Epoch of Reionisation* (EoR).

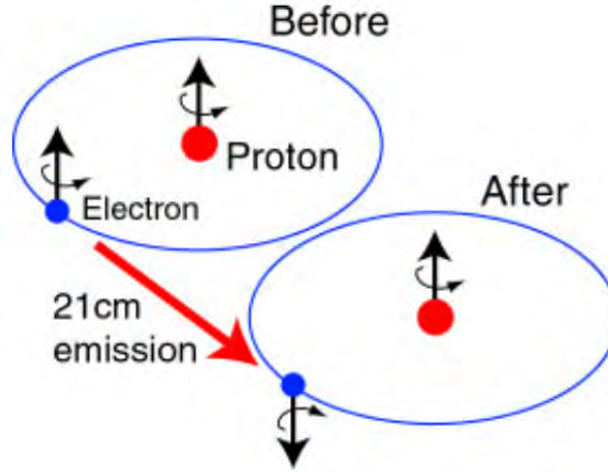


Figure 2.1: Illustration of the hyperfine transition in the Hydrogen atom giving rise to the 21 cm line. Credit: The Origins of Radio Astronomy

2.5.1 Cosmology with the 21 cm signal

The Hydrogen hyperfine transition occurs when an electron aligns its intrinsic spin to a proton spin, and this configuration state denoted as $1_1S_{1/2}$, has higher energy than the state when the spins are anti-parallel $1_0S_{1/2}$ (Storey et al., 1994). The hyperfine transition is a strongly forbidden transition, it has a very weak Einstein A coefficient, and this means it has a very long lifetime in the excited state, of order 1×10^7 years (Furlanetto, 2006). Figure 2.1 and 2.2 show a schematic representation of the hyperfine transition and the relevant quantum energy states, respectively.

The radiative transfer equation that describes how radiation passes through a cloud of neutral hydrogen with a uniform excitation (*spin*) temperature T_s . In the Rayleigh-Jeans limit (discussed in Sect 3.1), the emergent brightness temperature at frequency ν is given by:

$$T_b = T_s (1 - e^{-\tau_\nu}) + T_\gamma e^{-\tau_\nu}, \quad (2.38)$$

where τ_ν is the cloud optical depth, and T_γ is the brightness temperature of the background radiation (CMB) incident on the cloud. The first term of equation 2.38 describes the 21 cm emission that is emitted and re-absorbed by the gas and the second term is the absorption of the background radiation.

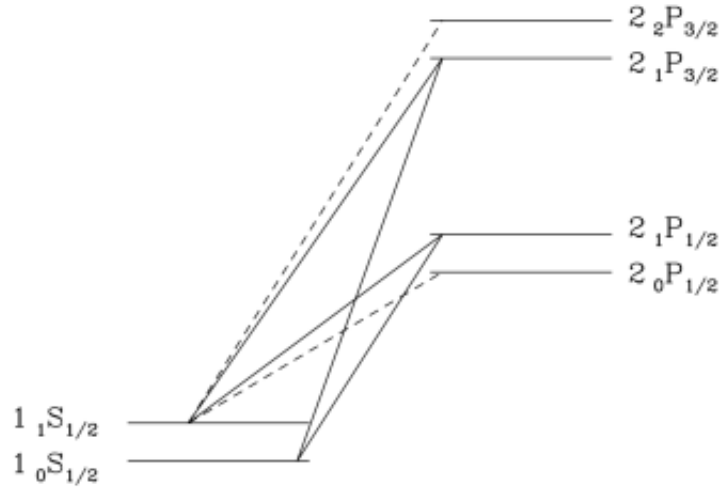


Figure 2.2: Hyperfine splitting of the 1 S and 2 P levels of the neutral Hydrogen atom. Solid lines represent transitions relevant for the Wouthuysen-Field effect, since they mix the population of the ground state Hyperfine levels, while the dashed lines represent forbidden transitions (Furlanetto, 2006).

The spin temperature quantifies the relative number densities of atoms n_1 in the hyperfine level with respect to the ground state:

$$\frac{n_1}{n_0} = 3 e^{-E_{10}/k_B T_s}, \quad (2.39)$$

where E_{10} is the energy split between the two energy levels. In most astrophysical applications, the exponent is very close to zero, i.e. three atoms are expected to be in the hyperfine level for each atom in the fundamental level (Furlanetto, 2006).

The brightness temperature of the 21 cm emission line relative to the CMB is given by (Furlanetto, 2006):

$$\delta T_b = T_b - T_\gamma = 9x_{H1}(1 + \delta)(1 + z)^{\frac{1}{2}} \left[1 - \frac{T_\gamma(z)}{T_s} \right] \left[\frac{H(z)/(1 + z)}{dv_{||}/dr_{||}} \right] \text{mK}, \quad (2.40)$$

where δ is the baryon over-density, x_{H1} the Hydrogen neutral fraction, $H(z)$ is the Hubble parameter at redshift z , $dv_{||}/dr_{||}$ is the gradient of the proper velocity along the line of site between the observer and the patch of IGM.

From equation 2.40, we can see that when $T_s \gg T_\gamma$, δT_b is positive, i.e. $\delta T_b > 0$, whereas is negative when $T_s \ll T_\gamma$. Therefore, how the 21 cm transition is observed relies upon the spin temperature, which dictates whether the 21 cm signal will appear in emission, absorption, or not at all (if $T_\gamma = T_s$). Figure 2.3 shows the theoretical evolution of the 21 cm signal.

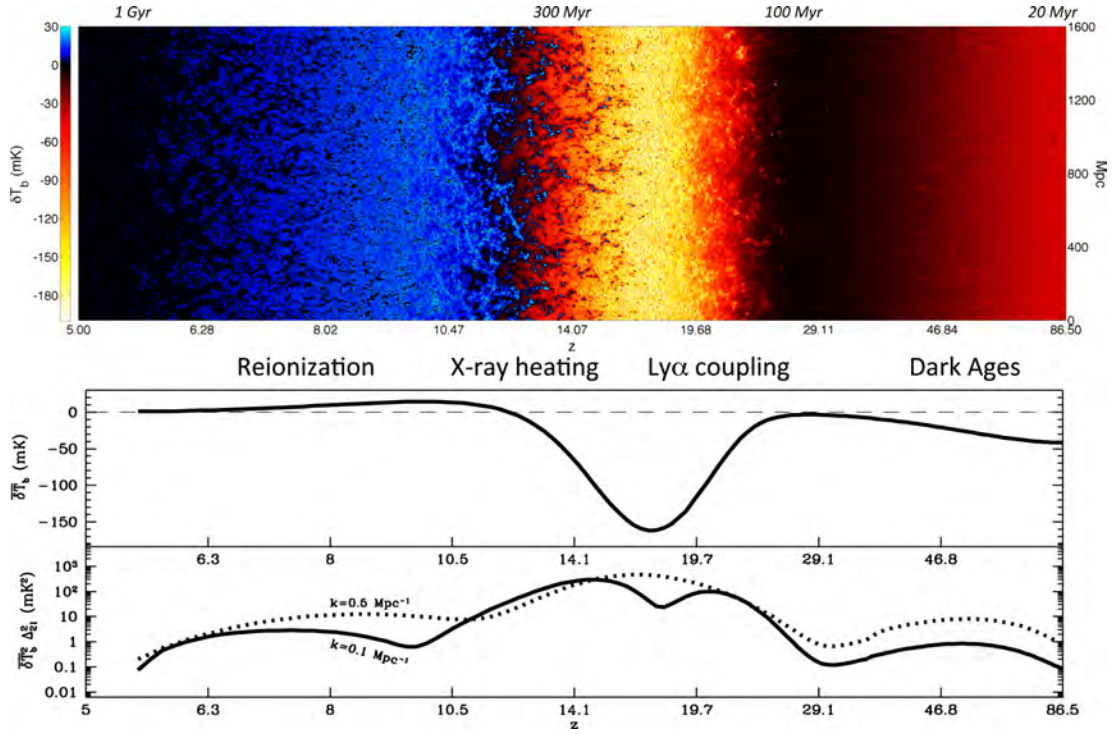


Figure 2.3: Evolution of the 21 cm signal. The top panel shows the evolution of the brightness temperature contrast δT_b with redshift z . The middle panel shows the corresponding sky-averaged signal (i.e. global signal, solid line). The dotted line denotes global signal $\overline{\delta T_b} = 0$ (see equation 2.42). The bottom panel shows the evolution of the power spectrum amplitude at $k = 0.1 \text{ h Mpc}^{-1}$ (solid line) and $k = 0.5 \text{ h Mpc}^{-1}$ (dotted line) (from Mesinger et al., 2016).

The spin temperature is set by three competing mechanisms:

- Absorption of CMB photons by neutral Hydrogen atoms, setting the spin temperature to CMB temperature ($T_s \rightarrow T_\gamma$);
- Collisions between neutral Hydrogen atoms set the spin temperature to the gas temperature ($T_s \rightarrow T_k$).

- Lastly, the resonant scatter of UV photons by neutral Hydrogen atoms or Wouthuysen-Field (WF, [Wouthuysen, 1952](#)) effect. Figure 2.2 shows the WF effect, this phenomenon occurs when a Ly α photon is absorbed by a neutral Hydrogen atom in the ground state $1S$, the electron can jump to either of the $2P$ states, following the quantum selection rules. At this point, the electron can decay from the $2P$ state to the fundamental triplet $1_1S_{1/2}$ rather than the singlet $1_0S_{1/2}$, allowing for a 21 cm photon to be emitted.

Figure 2.4 shows a fiducial model by [Mesinger et al. \(2011\)](#), showing the evolution of the spin temperature. Before the formation of the first luminous sources, neutral Hydrogen atoms absorb and re-emit CMB photons setting the spin temperature to the CMB temperature ($T_s \rightarrow T_\gamma$). At $z \approx 200$, baryons and the CMB decouple, and the gas temperature starts to cool down faster than CMB, while collisions couple the spin temperature to the gas temperature. At $z \approx 35$, the Universe has expanded sufficiently such that collisions are no longer efficient at coupling the spin temperature to the gas temperature.

When first stars form at $z \approx 30$, they emit background radiation of UV photons that drives the spin temperature to the gas temperature thanks to the WF effect. From this moment onward, the WF effect is the main coupling mechanism, and the spin temperature is coupled to the gas temperature. Eventually, star formation proceeds and X-ray sources form and begin to heat the gas well above the CMB temperature $z \approx 21$, $T_s \gg T_\gamma$. This transition is referred to as the *spin temperature saturation*, as the evolution of the 21 cm brightness contrast essentially no longer depends upon the spin temperature T_s (see equation 2.40).

2.5.2 Spatial fluctuations of the 21 cm signal

The spatial fluctuation of the 21 cm signal can be characterised by its power spectrum $P(k)$ (e.g., [Furlanetto, 2006](#)). A quantity analogous to the over-density field δ , the *factional brightness temperature contrast* is defined as:

$$\delta_{21}(\mathbf{x}) = \frac{\delta T_b(\mathbf{x}) - \overline{\delta T_b}}{\overline{\delta T_b}}, \quad (2.41)$$

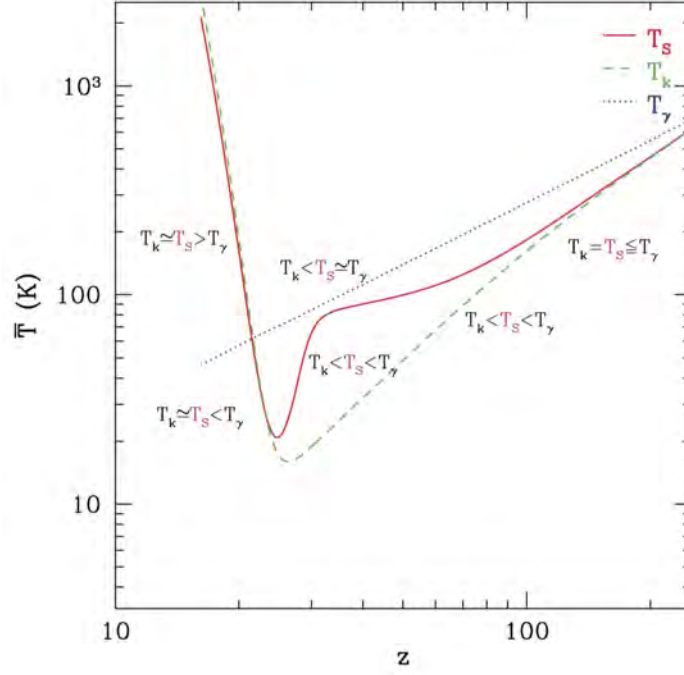


Figure 2.4: Fiducial evolution of the spin temperature T_s (red solid line), gas T_k (green dashed line) and CMB T_γ (blue dotted line) temperature, respectively (from [Mesinger et al., 2011](#)).

where

$$\overline{\delta T_b} = \frac{\int \delta T_b(\mathbf{x}) d\Omega}{\int d\Omega}, \quad (2.42)$$

is the volume averaged brightness temperature contrast i.e. *global signal*. The 21 cm power spectrum is therefore given by:

$$P(k) \delta_D(\mathbf{k} + \mathbf{k}') (2\pi)^3 = \langle \tilde{\delta}_{12}(\mathbf{k}) \tilde{\delta}_{12}(\mathbf{k}') \rangle, \quad (2.43)$$

where $\tilde{\delta}_{12}(\mathbf{k})$ is the Fourier transform of $\delta_{21}(\mathbf{x})$. The 21 cm power spectrum normally has units of $\text{mK}^2 (h^{-1} \text{Mpc})^3$, however, a dimensionless power spectrum is often used in literature:

$$\Delta_{21}^2 = \frac{k^3}{2\pi^2} P_{21}(k). \quad (2.44)$$

Figure 2.5 shows the power spectrum of the 21 cm signal, for various redshifts that mark significant stages of the IGM evolution.

At $z \sim 30$, the first luminous sources form, and their UV radiation begins to couple the spin temperature to the gas temperature, at this time the gas is colder than the CMB. Brightness

temperature fluctuations are driven here by fluctuations in Ly α radiation field (Furlanetto, 2006). At $z \sim 21$, star formation proceeds and the first X-ray sources form, radiating X-rays which begin to heat the surrounding environment, while most of the IGM remains cold. Brightness temperature fluctuations are driven here by the gas temperature fluctuations (Furlanetto, 2006).

At $z \sim 18$ X-ray heating has heated the gas well above the CMB, $T_s \gg T_\gamma$, almost everywhere in the IGM, saturating the spin temperature. The power spectrum is fainter here as the main source of fluctuations are large scale density fluctuations (Barkana & Loeb, 2007). Lastly, at $z \sim 10$, localised regions around the bright sources are ionised, and the averaged neutral fraction has dropped to $\sim 50\%$. Fluctuations are essentially driven by the fluctuations in the neutral fraction x_{H1} (Furlanetto, 2006).

2.6 Current status of observations

There are two main 21 cm observables, its spatial fluctuations or its sky-averaged (global) signal. Interferometric arrays are used to detect spatial fluctuations, whereas single dipole antennas probe the global signal.

Progress has been made in measuring spatial fluctuations of the 21 cm signal, the Giant Meterwave Radio Telescope (GMRT) was the first instrument to provide an upper limit of the 21 cm power spectrum during the EoR (Paciga et al., 2011, 2013). The Precision Array for Probing the Epoch of Reionisation (Parsons et al., 2010), followed and provided several upper limits (Parsons et al., 2014; Ali et al., 2015; Kolopanis et al., 2019). The Murchison Widefield Array (MWA) also provided the best upper limits at $z = 7$ (Barry et al., 2019) and $z = 6.5$ (Trott et al., 2020). The LOw-Frequency ARay (LOFAR) probed the Cosmic dawn at high redshift ($20 < z < 25$) (Gehlot et al., 2019) and also the provided best power spectrum upper limits in the $8 < z < 10.5$ range (Patil et al., 2017; Mertens et al., 2020). Results are all shown in Fig 2.6 and compared to a power spectrum of a fiducial, theoretical 21 cm model (Mesinger et al., 2011).

Progress has also been made in global signal experiments. The Shaped Antenna measurement of background RAdio Spectrum (SARAS) constrained the duration of the EoR to $6 < z < 10$

(Singh et al., 2017, 2018). SARAS observations also disfavored a class of models with weak X-ray heating and rapid reionisation.

Bowman et al. (2018) were the first to report the detection of a 21 cm absorption profile centred at 78 MHz ($z \approx 18$), with a width at half-maximum of approximately 19 MHz and an amplitude of about 500 mK. The result is very controversial as the amplitude is a factor two larger than the brightest models (e.g., Cohen et al., 2017). Various scenarios have been explored to account for this discrepancy. Fialkov & Barkana (2019) argued that the observed absorption profile could be explained if the baryon-photon decoupling occurs at a greater redshift or by the presence of excess radiation (Fialkov & Barkana, 2019). Natwariya & Bhatt (2020) argued that the α -effect (Brandenburg & Subramanian, 2007) which is caused by gas turbulence, twisting and enhancing magnetic field lines at the cost of gas energy, can lower of the gas temperature to 3.2 K at $z \approx 17$.

Several authors have, instead, questioned the results themselves. Singh & Subrahmanyan (2019) used a different data analysis method and found results that are consistent with the standard theoretical model. Hills et al. (2018) performed an analysis of EDGES result and found nonphysical parameters for the foreground model. They also pointed out that the Bowman et al. (2018) solution is not unique, as they were able to find alternative, simpler formulations of the signal that were different in shape. They also pointed out that Bowman et al. (2018) solution is not unique, as they were able to find other simple formulations of the signal that were different in shape. Competing experiments like the Large Aperture to Detect the Dark Ages (Bernardi et al., 2015; Price et al., 2018) and Probing radio Intensity at high-Z from Marion (Philip et al., 2019) will need to confirm their findings.

2.7 The Hydrogen Epoch of Reionization Array

The Hydrogen Epoch of Reionisation Array (HERA) is an instrument designed to measure the 21 cm signal in the $6 < z < 30$ range (DeBoer et al., 2017). It is currently under construction in the Karoo radio-quiet area in South Africa. At the time of writing, it consists of 144, 14 m-diameter parabolic dishes (Fig 2.7), reaching 350 dishes out to ~ 1 km when fully built. The

HERA layout is a split-core hexagonal grid with the smallest spacing between two antennas being 14.6 m (DeBoer et al., 2017) in order to achieve a maximally redundant configuration. Two baselines are defined as redundant if they have the same orientation and length.

Redundant arrays have poor imaging performances but maximum sensitivity on a certain number of k modes and are, therefore, a promising strategy to detect the 21 cm signal (Parsons et al., 2012). Redundancy also offers a diagnostic to investigate the instrumental response/performances (Carilli et al., 2018).

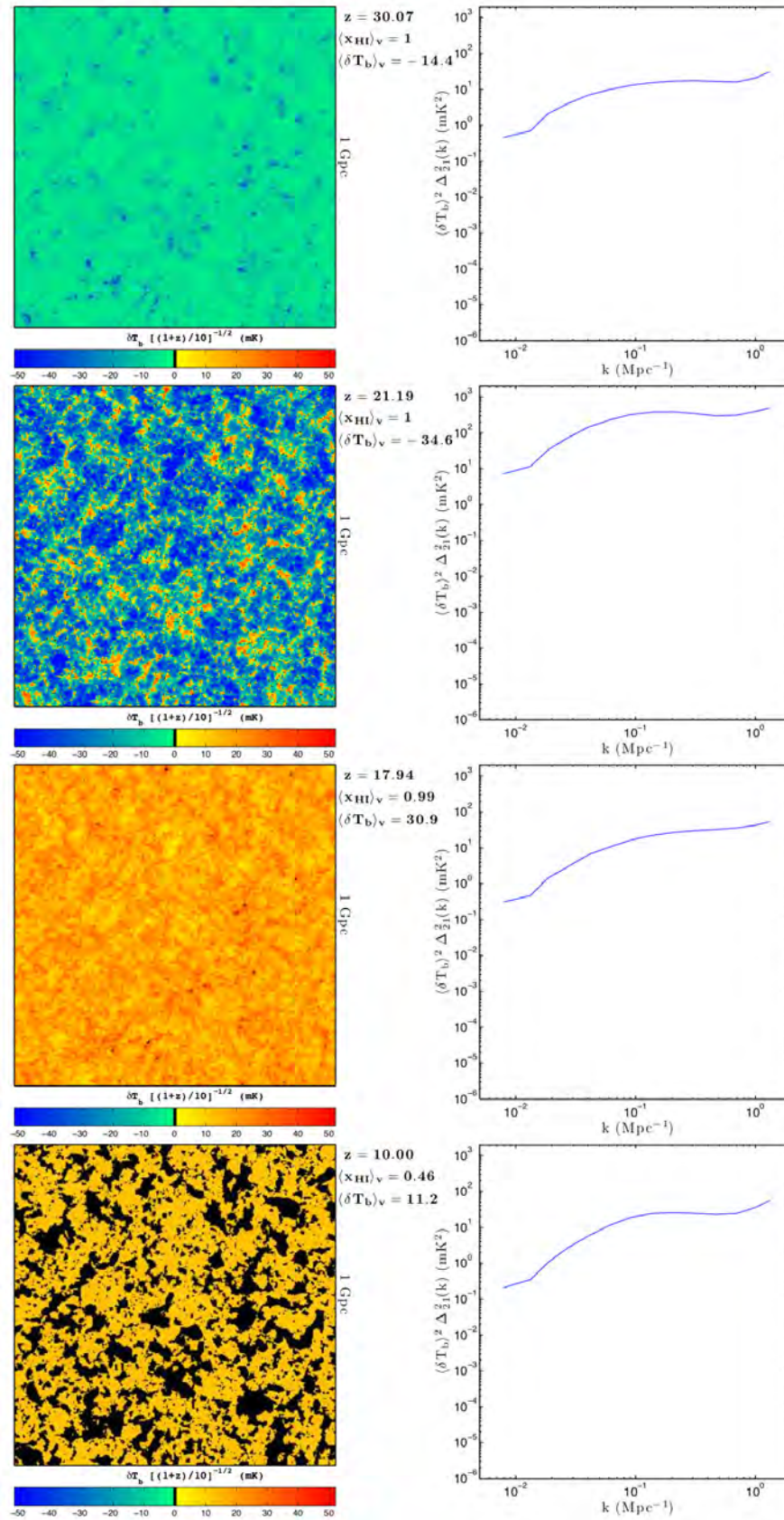


Figure 2.5: Left panels: slices from 21 cm simulation at redshifts $z = 30.1, 21.2, 17.9$ and 10.0 (top to bottom). Boxes are 1 Gpc wide and 3.3 Mpc deep. Right panels: corresponding dimensionless power spectra (see equation 2.44; from Mesinger et al., 2011).

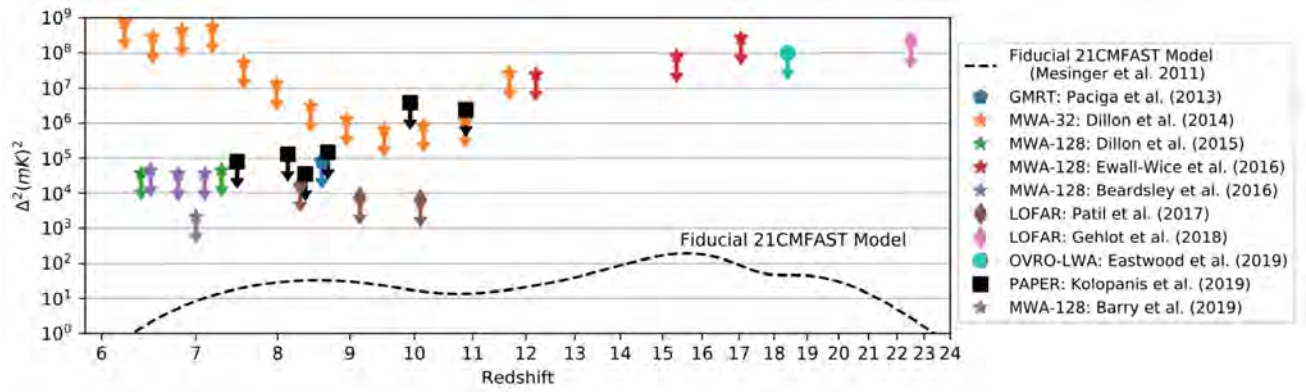


Figure 2.6: Current upper limits on the EoR power spectrum for values in the $0.1 < k < 1 \text{ Mpc}^{-1}$ range. The dashed line is a simulated fiducial model (from Liu & Shaw, 2020).

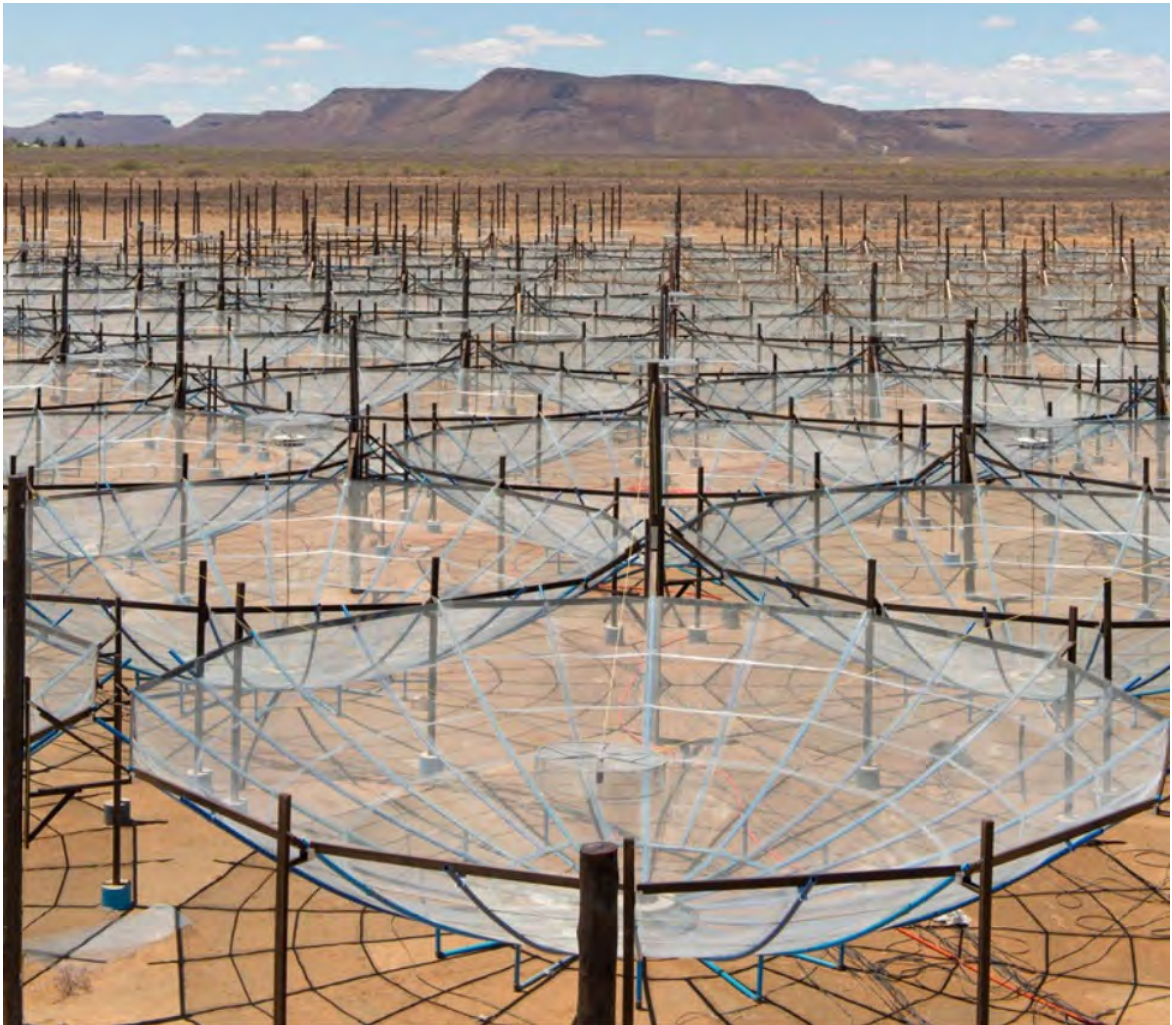


Figure 2.7: HERA array composed of 14 m parabolic transit dish antennas. credit: *South African Radio Astronomy Observatory (SARAO)*.

Observations of the EoR with Closure Phase Quantities

3.1 Review of Radio Interferometry and Calibration

We start the discussion by first reviewing the basic concepts of radio astronomy following [Thompson et al. \(2008\)](#). A radio interferometer is an ensemble of two or more radio antennas, whose signals are combined to form an interference pattern. A radio antenna is a device designed to detect electromagnetic waves at radio frequencies. An ideal antenna measures a quantity known as the flux density of a radio source. The flux density of a radio source is defined to be:

$$S_\nu = \int_{\Omega} \cos \theta I_\nu(\Omega') d\Omega', \quad (3.1)$$

where Ω is the solid angle subtended by the source, and θ is the angle between the source centre and the element of solid angle $d\Omega$. I_ν is the source brightness at a frequency ν , i.e. the intensity per solid angle, unit time and frequency, measured in $[\text{Hz}^{-1} \text{s}^{-1} \text{sr}^{-1}]$.

The source brightness is associated with the brightness temperature T_ν , which is defined to be the temperature of a black-body with an intensity B_ν such that $B_\nu = I_\nu$. Planck's law of black

body radiation states that:

$$B_\nu(\nu, T_\nu) = \frac{2h\nu^3}{c^2} \frac{1}{e^{\frac{h\nu}{k_B T_\nu}} - 1}, \quad (3.2)$$

where k_B is Boltzmann's constant. To first order approximation, B_ν at low frequencies (radio waves) where $h\nu \ll k_B T_\nu$ i.e. the Raleigh-Jeans limit is:

$$B_\nu(\nu, T_\nu) = \frac{2\nu^2 k_B T_\nu}{c^2}. \quad (3.3)$$

3.1.1 Van Cittert-Zernike Theorem

The simplest radio interferometer is the two-element interferometer where signals measured from a pair of antennas (p, q) are cross-multiplied and averaged in time. This operation is known as *correlation* and leads to the fundamental quantity measured in radio interferometry, the *visibility function* V_{pq} . The *Van Cittert-Zernike theorem* states that the correlation of signals from the (p, q) pair is related to the sky brightness $I(l, m, \nu)$ by a Fourier transform:

$$V_{pq}(u, v, \nu) = \iint I(l, m, \nu) e^{2\pi i(ul+vm)} dl dm, \quad (3.4)$$

where (u, v) are the components (normally expressed in wavelength units) of the baseline vector \mathbf{b} that connects antenna p to antenna q . The coordinates (l, m) are cosine coordinates, typically centred on the observed source. A schematic representation of a two element interferometer is shown in Fig 3.1.

The sky brightness can in principle be obtained from the visibility function $V(u, v)$ by taking the Fourier transform. An interferometer has a finite number of antennas and thus only samples the visibility function at specific (u, v) points. The sampling function $S(u, v)$ depends on the array layout, the observing frequency and time. Equation 3.4 can be inverted to obtain the so-called dirty image I_D :

$$I_D(l, m, \nu) = \int V(u, v, \nu) S(u, v) e^{-2\pi i(ul+vm)} du dv = I(l, m, \nu) * \tilde{S}(l, m), \quad (3.5)$$

where $*$ is the convolution operator and \tilde{S} is the Fourier transform of the sampling function, also known as the *Point Spread Function* (PSF). The interferometer has an angular resolution that

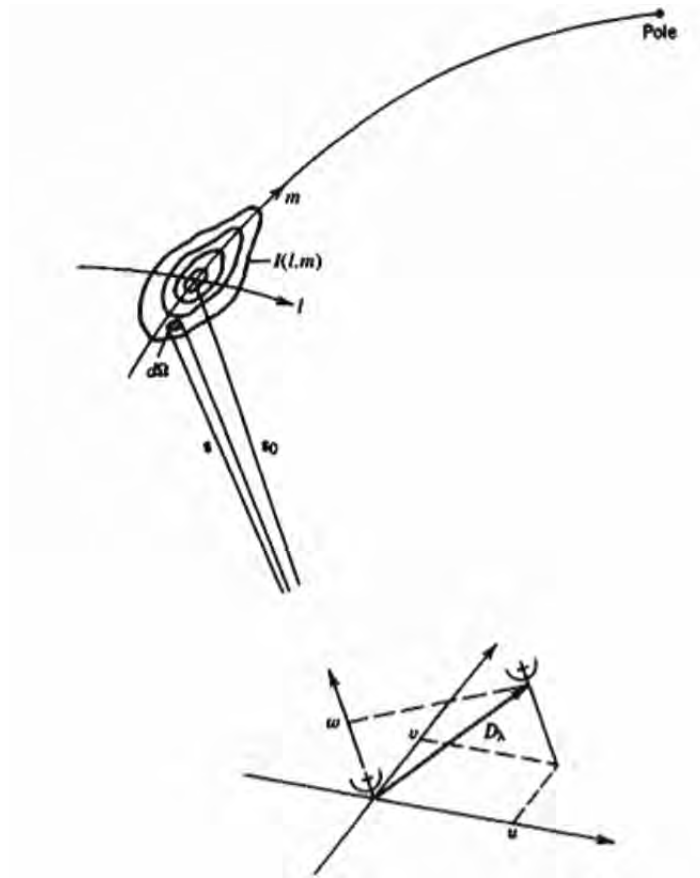


Figure 3.1: Schematic representation of an two-element interferometer observation (from Bruyn, 2008).

corresponds approximately to the longest baseline $|\mathbf{b}_{\max}|$:

$$\theta_{res} \approx \frac{\lambda}{|\mathbf{b}_{\max}|}, \quad (3.6)$$

where λ is the wavelength corresponding to the frequency ν .

3.1.2 The Radio Interferometry Measurement Equation (RIME)

In ideal conditions and with ideal antennas, the sky brightness is related to the measured visibilities by a Fourier transform (equation 3.4). However, real antennas are not perfect, and the electromagnetic radiation from a radio source passes through the atmosphere/ionosphere before reaching the antenna. The signal is thus corrupted. The *Radio Interferometry Measurement*

Equation (RIME) describes the various propagation effects that corrupt the signal.

Let us consider two antennas p, q that measure voltages $v_p = \mathbf{J}_p \mathbf{e}_p$ and $v_q = \mathbf{J}_q \mathbf{e}_q$ sourced by a point on sky propagating along two orthogonal polarisations (x, y) . Visibilities from the two antennas can be cast in a 2×2 matrix \mathbf{V}_{pq} :

$$\mathbf{V}_{pq} = 2 \left\langle \begin{bmatrix} v_{px} \\ v_{py} \end{bmatrix} \begin{bmatrix} v_{qx}^* & v_{qy}^* \end{bmatrix} \right\rangle, \quad (3.7)$$

where $\langle \rangle$ indicates a time average. The basic form of the RIME is given by (Smirnov, 2011):

$$\mathbf{V}_{pq}(t, \nu) = 2 \mathbf{J}_p \langle \mathbf{e}_p \mathbf{e}_q^H \rangle \mathbf{J}_q^H, \quad (3.8)$$

where \mathbf{J}_p and \mathbf{J}_q are the 2×2 Jones matrices describing propagation effects along the signal path to antenna p and q respectively, $(\mathbf{e}_p, \mathbf{e}_q)$ are the incident electric field vectors on antennas p and q and H is the Hermitian operator. The term $\langle \mathbf{e}_p \mathbf{e}_q^H \rangle$ is often referred to as the source brightness matrix \mathbf{B} :

$$\mathbf{B} = 2 \begin{bmatrix} \langle e_x e_x^* \rangle & \langle e_x e_y^* \rangle \\ \langle e_y e_x^* \rangle & \langle e_y e_y^* \rangle \end{bmatrix} = \begin{bmatrix} I + Q & U + iV \\ U - iV & I - Q \end{bmatrix}, \quad (3.9)$$

where (I, Q, U, V) are the Stokes parameters. The RIME can therefore be written as:

$$\mathbf{V}_{pq} = \mathbf{J}_p \mathbf{B} \mathbf{J}_q^H. \quad (3.10)$$

Jones matrices are classified in two types: direction independent, when they are only function of time and frequency, i.e. $\mathbf{J}(t, \nu)$, and direction dependent, when they also depend upon position in the sky, i.e. $\mathbf{J}(t, \nu, l, m)$. Direction independent effects are antenna based corruptions that can still vary with time and frequency, but remain constant across the field of view. Direction dependent effects vary, instead, also along different lines of sight.

For an extended region of the sky, the RIME can be written as (Smirnov, 2011):

$$\mathbf{V}_{pq}(t, \nu) = \mathbf{J}_p(t, \nu) \left(\int \int \mathbf{J}_p(t, \nu, l, m) \mathbf{B}(l, m) \mathbf{J}_q^H(t, \nu, l, m) dl dm \right) \mathbf{J}_q^H(t, \nu). \quad (3.11)$$

3.1.3 Direction Independent Effects

In this section we will describe some direction independent effects. The ideal frequency response of the instrument would be unity within the observing band and zero outside. However, in reality

the system response always shows deviations from this behaviour. These effects can be described by a bandpass Jones matrix \mathbf{B} given by:

$$\mathbf{B}(\nu) = \begin{bmatrix} b_x(\nu) & 0 \\ 0 & b_y(\nu) \end{bmatrix}. \quad (3.12)$$

To a first approximation, the bandpass is fairly stable with time and therefore a function of frequency only.

Another typical direction independent corruption is related to the receiver gain that is needed to amplify the sky signals and its time deviation from the ideal response. This effect can be modelled by a Jones matrix \mathbf{G} :

$$\mathbf{G}(t) = \begin{bmatrix} g_x(t) & 0 \\ 0 & g_y(t) \end{bmatrix}. \quad (3.13)$$

3.1.4 Direction Dependent Effects

Examples of direction dependent effects are the antenna primary beam and ionospheric distortions. The ionospheric direction dependent effect is very significant at low frequencies and is caused by the differential delay that the signal experiences in reaching each antenna, due to the different Total Electron Content (TEC) along the lines of sight. Ionospheric effects can be expressed by a scalar Jones term Z_p :

$$Z_p(l, m, \nu, t) = e^{i\Theta_p(l, m, \nu, t)}, \quad (3.14)$$

where $\Theta_p(l, m, \nu, t) \sim T(l, m, t) \nu^{-1}$ and T is the TEC along the line-of-sight. The TEC determines the degree of refraction (Intema et al., 2009). Phase delays can reach values up to 10^4 rad at lower frequencies, with variations on short timescales, making it a severe direction dependent effect (Lonsdale, 2005). The ionosphere also introduces excess path length that ranges between a maximum of 350 m during the night to a maximum 3500 m during the day, with a frequency dependence of ν^{-2} (Thompson et al., 2008). Four different regimes characterize the type of ionospheric distortions. The four regimes depend upon three quantities; the array size A , scale size of the ionospheric phase fluctuations S and the field of view V (Lonsdale, 2005).

In *isoplanatic* conditions where the field of view is small ($V \ll S$), the ionospheric phase delay per antenna does not vary with the line of sight (Intema et al., 2009). Phase delays are effectively constant across the field of view resulting in a mere direction independent effect that can be absorbed into antenna based gains during calibration (Smirnov, 2011). This is both valid for compact ($A < S$) and large arrays ($A > S$) and these regimes are labelled 1 and 2 respectively.

Under *anisoplanatic* conditions ($V > S$), the ionospheric delays vary over the field of view. For compact arrays, the phase delays are varying linearly across the array, with a gradient that varies with pointing direction. As a result, the apparent position of sources changes with time and pointing direction (regime 3). However, if the array size is large, sources in the field of view can appear structurally deformed (regime 4), i.e. appear in a different shape. In both cases a single-phase correction per antenna is no longer sufficient, i.e. the ionospheric effect is direction dependent.

In this study, we are, however, particularly interested in the direction dependent Jones matrices \mathbf{E} that describes the antenna primary beam response. An antenna is not an isotropic receiver but has a degree of directivity, i.e. its sensitivity varies across the sky. The unpolarized primary beam response is described by a diagonal Jones matrix (Smirnov, 2011):

$$\mathbf{E}(l, m, t, \nu) = \begin{bmatrix} e_x(l, m, t, \nu) & 0 \\ 0 & e_y(l, m, t, \nu) \end{bmatrix}, \quad (3.15)$$

indicating its dependence upon looking direction, frequency and time - the latter normally due to the rotation of the sky with respect to the feed orientation.

Although antennas are designed to be identical to each other as far as possible, they are never so in practice. This difference can be expressed with a RIME of the form:

$$\mathbf{V}_{pq}(t, \nu) = \int \int \mathbf{E}_p(t, \nu, l, m) \mathbf{B}(l, m) \mathbf{E}_q^H(t, \nu, l, m) dl dm, \quad (3.16)$$

where the primary beams of the two antennas are different, i.e. $\mathbf{E}_p \neq \mathbf{E}_q$. If the sky is composed of only a certain number of point sources N_s , equation 3.16 becomes:

$$\mathbf{V}_{pq}(t, \nu) = \sum_{s=1}^{N_s} \mathbf{E}_{s,p}(t, \nu) \mathbf{K}_{s,p} \mathbf{B}_s \mathbf{K}_{s,q} \mathbf{E}_{s,q}(t, \nu)^H = \sum_{s=1}^{N_s} \mathbf{E}_{s,p} \mathbf{X}_{s,pq} \mathbf{E}_{s,p}^H, \quad (3.17)$$

where \mathbf{K} is the geometric delay Jones matrix (Smirnov, 2011):

$$\mathbf{K}_p = \begin{bmatrix} e^{-2\pi i \phi_p} & 0 \\ 0 & e^{-2\pi \phi_p} \end{bmatrix}, \quad (3.18)$$

where ϕ_p is the phase delay of antenna p . The geometric delay term captures the delays associated with signal arrival time to the different antennas in the array. We define the source *coherency matrix* as:

$$\mathbf{X}_{s,pq} = \mathbf{K}_{s,p} \mathbf{B}_s \mathbf{K}_{s,q}. \quad (3.19)$$

Equation 3.17 will be used in this thesis work to simulate the impact of different primary beams on a foreground sky model.

3.1.5 Calibration

Calibration is the process of solving for the various Jones terms, given a brightness source model. Calibration has often been divided into three levels: first, second and third generation calibration. The first and second generation calibration solves for direction independent gains, that is essentially always possible as the system of equations is over-determined, given N unknowns and $N(N - 1)/2$ visibility measurements. Third generation calibration solves for direction dependent gains (Smirnov, 2011).

First generation calibration requires the observation of an unresolved source with a known spectrum. Observations of calibration sources are normally interspersed with observations of the target field. This is done so that calibration observations track changes in the system such as antenna gains. Gain solutions from the calibrator source are interpolated and applied to the target field to obtain corrected visibilities $\mathbf{V}_{pq}^c(t, \nu)$:

$$\mathbf{V}_{pq}^c(t, \nu) = \mathbf{J}_p^{-1}(t, \nu) \mathbf{V}_{pq}^m(t, \nu) (\mathbf{J}_q^H)^{-1}(t, \nu), \quad (3.20)$$

where $\mathbf{V}_{pq}^m(t, \nu)$ are the measured visibilities and \mathbf{J}_p^{-1} , \mathbf{J}_q^{-1} are inverse Jones matrices of antennas p and q , with $\mathbf{J}_p = \mathbf{B}_p(\nu) \mathbf{G}_p(t)$, typically.

After performing first generation calibration, an image of the target field is made. The image - and therefore the calibration - quality is often measured by the dynamic range DR :

$$DR = \frac{I_p}{\sigma_I}, \quad (3.21)$$

where I_p is the image peak and σ_I is the image rms noise. A better dynamic range is often a consequence of an improved calibration, for example, *second generation* calibration or self-calibration (Smirnov, 2011; Zhao et al., 2019). Self-calibration is an iterative process that begins with finding an initial sky model that is then used to solve for time-variable antenna gains. Re-calibrated visibilities are then imaged and deconvolved to improve the sky model. The process is repeated until a target dynamic range is reached or if further improvement of the image is not possible.

The last step in the calibration process is to perform *third generation calibration*, where the self-calibrated image is corrected for direction dependent effects. The process of correcting for the various direction dependent effects is at the frontier of modern interferometric calibration and we defer the reader to Smirnov (2011) for a more detailed description.

3.2 Power spectrum of the 21 cm signal from inteferometric observations

Fluctuations of the 21 cm brightness temperature $T(\boldsymbol{x})$ can be measured by its power spectrum $P(k)$ (Furlanetto, 2006):

$$\langle \tilde{T}(\boldsymbol{k}) \tilde{T}(\boldsymbol{k}')^* \rangle = (2\pi)^3 \delta_D(\boldsymbol{k} - \boldsymbol{k}') P(k), \quad (3.22)$$

where $\tilde{T}(\boldsymbol{k})$ is the Fourier transform of the 21 cm brightness temperature $T(\boldsymbol{k})$ * indicates the complex conjugate, $\langle \rangle$ the ensemble average and δ_D the Dirac operator.

An interferometer already performs a two dimensional Fourier transform of the brightness temperature $T(\boldsymbol{x})$ (see equation 3.3 and 3.4):

$$V(u, v) = \frac{2k_B}{\lambda^2} \int \int T_\nu(l, m) e^{2\pi i(ul+vm)} dl dm. \quad (3.23)$$

The three dimensional power spectrum can be obtained by Fourier transforming the visibilities along the frequency axis at a given redshift. The frequency axis is directly related to distances along the pointing direction or line of sight (see equation 2.20). The Fourier transform of the visibility along its frequency axis is known as the *delay transform* (Parsons et al., 2012):

$$\tilde{V}_{pq}(\tau) = \int V_{pq}(\nu) W(\nu) e^{-2\pi i\nu\tau} d\nu, \quad (3.24)$$

where τ is the Fourier conjugate variable of ν , $W(\nu)$ is spectral weighting function and

$$V_{pq} = \int \int E_p(l, m, \nu) E_q^*(l, m, \nu) I(l, m, \nu) e^{-2\pi i(u_{pq}l + v_{pq}m)} dl dm. \quad (3.25)$$

Figure 3.2 illustrates the delay spectrum from a single baseline for two flat-spectrum sources. The two sources have different geometric delays τ_g , this being a result of their relative positions to the baseline. As both sources are flat-spectrum, their delay spectra are peaked at the corresponding τ_g , i.e. they are a delta-like function centred at source delays $\delta(\tau - \tau_g)$ convolved with the primary beam $E(\nu)$ and the window function $W(\nu)$.

If we consider a narrow field of view, such that $l \approx \theta_x$ and $m \approx \theta_y$, the quantities $(\theta_x, \theta_y, \nu)$ can be directly related to cosmological distance $\mathbf{x} = (x_\perp, x_\parallel \hat{\mathbf{z}})$, where x_\perp and $x_\parallel \hat{\mathbf{z}}$ are the comoving position vectors perpendicular and parallel to the line of sight, respectively (Parsons et al., 2012). The comoving distance between the present time $z_{obs} = 0$ and the redshift z is given by equation 2.20 as:

$$x(z) = c \int_0^z \frac{dz'}{H(z')}. \quad (3.26)$$

The radial comoving distance corresponding to a redshift interval Δz centred at a particular epoch of redshift z can therefore be expressed as:

$$\Delta x_\parallel(z) = \frac{c\Delta z}{H_0 E(z)} = \frac{cB_{\text{eff}}(1+z)^2}{\nu_{21} H_0 E(z)}, \quad (3.27)$$

where $\nu_{21} = 1402$ MHz is the frequency of the 21 cm hyperfine transition, and Δz is the change in redshift corresponding to the frequency bandwidth B_{eff} :

$$B_{\text{eff}} = \int_{\nu_1}^{\nu_2} W(\nu) d\nu. \quad (3.28)$$

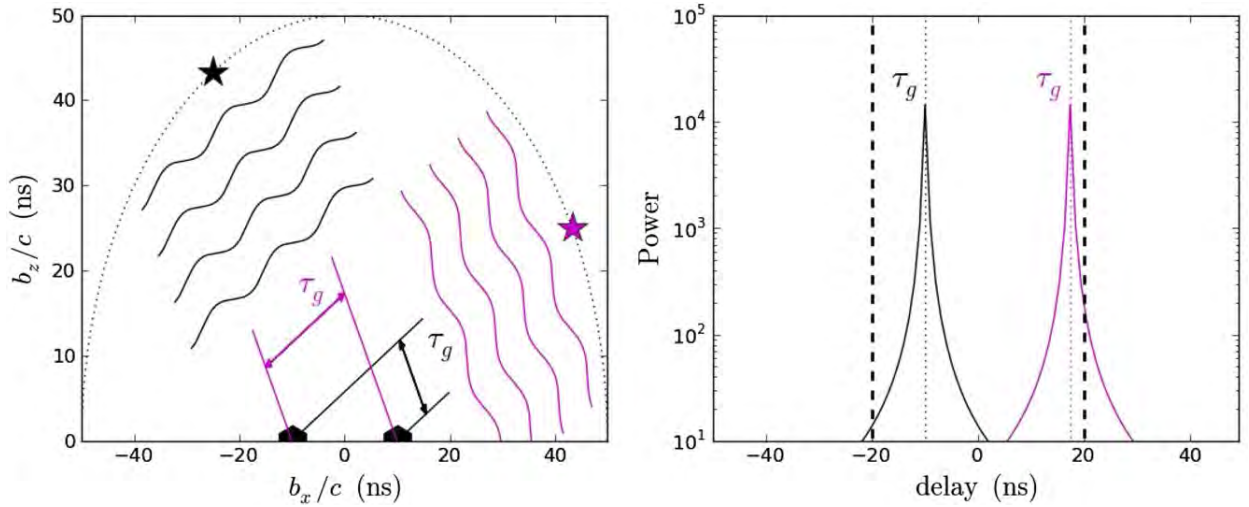


Figure 3.2: Cartoon representation of the delay transform: two sources with identical spectra having differing geometric delays τ depending upon their position in the sky (left). Their delay spectra (right) are peaked at the corresponding geometrical delays and bound by the horizon limit, defined as the maximum allowed delay, i.e. the delay corresponding to the horizon (from Parsons et al., 2012).

where the frequency range $B = \nu_2 - \nu_1$ is often chosen such that $B_{\text{eff}} \approx 10\text{MHz}$. The cosmic evolution limits the largest bandwidth to about 10 MHz, since for larger bandwidths the evolution of the Universe begins to impact the result as there are significant changes in IGM morphology over the studied period (Thyagarajan et al., 2013).

In the small angle approximation, the comoving transverse distance is given by $\mathbf{x}_\perp = x(z)\boldsymbol{\theta}$, where $\boldsymbol{\theta} = (\theta_x, \theta_y)$. If $\theta_x = \theta_y = \theta$ then the components of \mathbf{x}_\perp are given by:

$$D_c = x(z)\theta. \quad (3.29)$$

The radial distances are measured relative to the central value of the observing bandwidth, and thus we can replace Δx_\parallel and $\Delta\nu$ with just x_\parallel and ν respectively. The spacial frequency of the power spectrum $\mathbf{k} = (k_\parallel, \mathbf{k}_\perp)$ corresponding to position vector $\mathbf{x} = (x_\parallel, \mathbf{x}_\perp)$ can be expressed as (Thyagarajan et al., 2013):

$$k_\parallel = \frac{2\pi\nu_{12}H_0E(z)}{c(1+z)^2}\tau, \quad (3.30)$$

and

$$\mathbf{k}_\perp = \frac{2\pi\nu}{cD_c} \mathbf{b}. \quad (3.31)$$

Considering the change of variables from τ to $k = |\mathbf{k}|$ the three dimensional power spectrum from visibility measurements can be finally expressed as (Thyagarajan et al., 2013):

$$P(k) = |\tilde{V}(\tau)|^2 \left(\frac{\lambda^2}{2k_B} \right)^2 \left(\frac{D_c^2 \Delta D_c}{B_{eff}} \right) \left(\frac{1}{\Omega B_{eff}} \right) \quad (3.32)$$

where λ is the center wavelength of observing bandwidth, $\Delta D_c = \Delta x_{||}$ and Ω the field of view solid angle. The units of equation 3.32 are $\text{mK}^2 (h^{-1} \text{Mpc})^3$.

3.3 Foregrounds: an overview

The biggest challenge in the measurement of the redshifted 21 cm signal is the presence of foregrounds which are a few orders of magnitude brighter than the cosmological signal (e.g., Bernardi et al., 2010). In Fig 3.3, we show the brightness temperature of foregrounds compared to the 21 cm signal. The Galactic component dominates at large angular scales and account for $\sim 70\%$ of the total power, while extra-galactic sources are relevant at small angular scales and accounts for the remaining $\sim 30\%$ (Santos et al., 2005). The knowledge of foreground properties is important in order to separate them from the 21 cm signal.

3.3.1 Galactic synchrotron emission

Synchrotron radiation occurs when a relativistic electron is accelerated in a magnetic field. Accelerated charged particles generate electromagnetic waves with a radiation power given by (Rybicki & Lightman, 1979):

$$\frac{dE}{dt} \propto \gamma^2 H^2 \sin^2(\theta_p), \quad (3.33)$$

where γ , H and θ_p are the Lorentz factor, the magnetic field strength and the pitch angle between the electron velocity and the magnetic field, respectively. The peak intensity of the radiation occurs at a critical frequency ν_{cr} :

$$\nu_{cr} \propto \gamma^2 H, \quad (3.34)$$

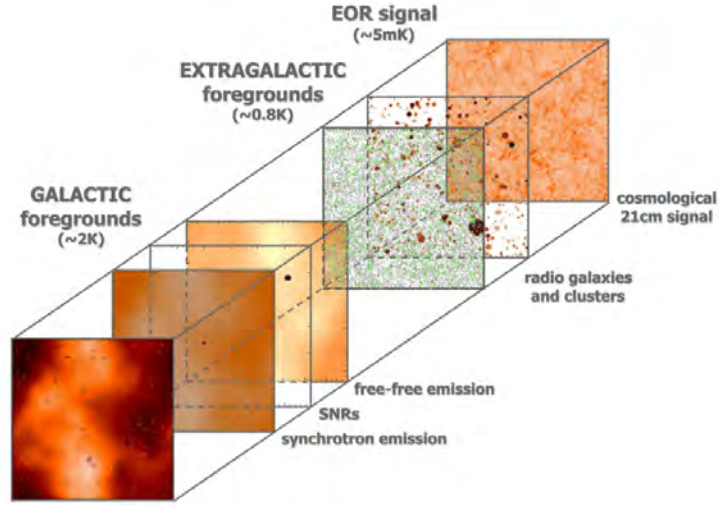


Figure 3.3: Illustrations of the various foreground components and their relative brightness temperature in contrast to the 21 cm signal (from Jelić et al., 2008).

i.e., the more energetic the electron, the higher the frequency of the emitted radiation. In the Milky Way, relativistic electrons with $\gamma = 10^4$ are essentially produced by supernovae in the Galactic plane and spiral around the Galactic magnetic field, which has a strength of about $10 \mu\text{G}$ (Haverkorn, 2015).

Relativistic electrons have a broad distribution in energy and, therefore, span a range of critical frequencies. As a result, the observed synchrotron spectrum $I(\nu)$ can be approximated by a power law:

$$I(\nu) \propto N_e B_{\perp}^{(\Theta+1)/2} \nu^{-(\Theta-1)/2}, \quad (3.35)$$

where N_e is the electron number density, B_{\perp} is the magnetic field component perpendicular to the line of sight, Θ is the power law index of the electron spectral distribution (Pacholczyk, 1970). The spectral index of a source α is defined such that flux density $S(\nu)$ at frequency ν is given by:

$$S(\nu) \propto \nu^{-\alpha}, \quad (3.36)$$

thus the spectral index of the Galactic synchrotron emission is $\alpha = (\Theta - 1)/2$. Measurements of Galactic synchrotron radiation are often expressed in terms of brightness temperature $T(\nu)$:

$$T(\nu) \propto \nu^{\beta}, \quad (3.37)$$

where $\beta = -2 + \alpha$.

One of the best templates of Galactic synchrotron emission is the 408 MHz all-sky map with a resolution of 56 arcmin (Fig 3.4; Haslam et al., 1982). Beuermann et al. (1985) interpreted the 408 MHz as the combinations of the emission from a thin disk (10%) and a thick disk (90%) that extends over several kpc, where relativistic electrons and magnetic fields are likely dynamically coupled to the hot Galactic halo.

The Galactic synchrotron radiation is expected to have smooth frequency spectra. It has, however, complex spatial morphology with spatial variations down at 13 arcmin (e.g., Bernardi et al., 2010). These spatial fluctuations can couple to frequency structure when measured with an interferometer (Bernardi et al., 2010; Parsons et al., 2012).

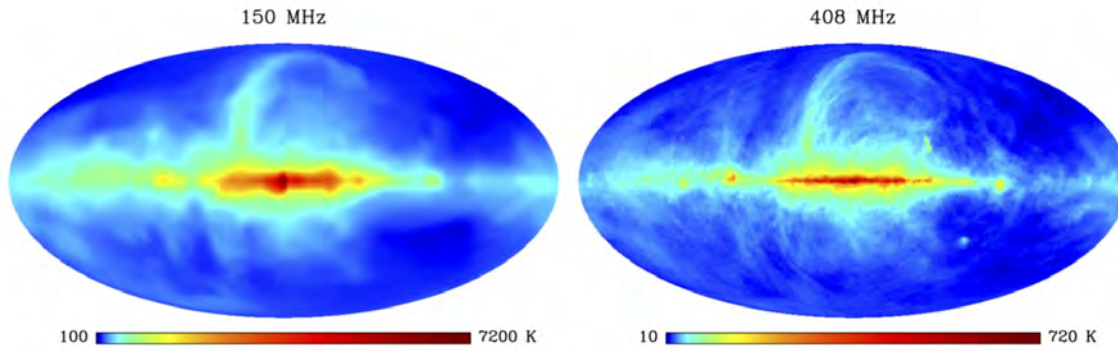


Figure 3.4: Comparison between the 150 MHz (left, Landecker & Wielebinski, 1970) and the 408 MHz maps (right, Haslam et al., 1982). We note the similar morphologies between the two frequencies.

3.3.2 Extra-galactic foregrounds

Extra-galactic foreground emission mostly comes from Active Galactic Nuclei that accrete material on a central black hole (e.g., Krolik, 1998). Relativistic jets can be emitted by the black hole and emit synchrotron radiation. Most extra-galactic sources show a power law spectrum, with a median spectral index of $\alpha = 0.8$ (De Breuck et al., 2000). Deviations from the spectral smoothness are expected at low-frequencies as a consequence of *synchrotron self-absorption*.

Synchrotron self-absorption occurs when the source density is high and re-absorption of the radiation occurs by the plasma itself. This phenomenon becomes important as it leads to an inverted spectral index $\alpha = -0.5$ below a turnover frequency. The turnover frequency is generally between 10 MHz and 1 GHz (Kellermann & Pauliny-Toth, 1969).

Current surveys, however, do not show strong evidence for synchrotron self-absorption. A study of sources in the Galactic and Extragalactic All-sky MWA (GLEAM Hurley-Walker et al., 2017) survey by Callingham et al. (2017), found that only $\sim 5\%$ of the sources show a turnover between 72 MHz and 1.4 GHz.

3.4 Foreground mitigation methods

The problem of mitigating (or separating) the 21 cm signal from foregrounds is one of the most active research lines. Foreground mitigation strategies can be broadly divided into subtraction and avoidance methods. We review both methods in this section, also discussing their strengths and limitations.

3.4.1 Foreground subtraction

Foreground subtraction methods attempt to model and subtract foregrounds from 21 cm observations. The process generally begins with the subtraction of bright, compact sources. The subtraction is normally done in visibility space (e.g., Yatawatta, 2010) often including direction dependent calibration (Yatawatta et al., 2013; Smirnov, 2011). After bright source subtraction, the sky brightness is dominated by the diffuse foreground emission (i.e., Bernardi et al., 2010). The modelling and subtraction of diffuse foreground emission is generally performed in two ways:

- *Parametric Fitting*: In this method, a foreground spectral model is assumed, and its coefficients are fitted to the data on an image pixel basis (e.g., Wang et al., 2006; Bowman et al., 2009; Liu et al., 2009). For example, a polynomial function is fitted for each pixel of the observed image cube (Bowman et al., 2009).

- *Non-parametric Fitting*: In this method, the functional form used to model foregrounds is not fixed a priori, but foreground properties and their statistics are assumed (e.g., [Harker et al., 2009](#)). A recent method uses a statistical model for extra-galactic sources and Galactic synchrotron emission ([Trott et al., 2016](#)).

[Chapman et al. \(2014\)](#) performed a series of simulations showing that foreground avoidance methods enable better recovery of the 21 cm signal at $k_{\perp} > 0.6 \text{Mpc}^{-1}$, while foreground removal methods are able to recover significantly more signal at small values of k_{\parallel} in both current and future experiments. [Chapman et al. \(2014\)](#) also found that if foreground spectra are unsmooth both methods perform well at low k_{\parallel} modes, however, at high k_{\parallel} modes foreground subtraction methods are able to recover more signal.

Some of the brightest sources can have complicated, extended morphologies: failures in their accurate modelling and subtraction can leave residual foreground contamination that may prevent the 21 cm detection. Over-fitting diffuse emission may equally lead to 21 cm signal loss (e.g., [Wang et al., 2013](#)).

3.4.2 Foreground avoidance

The need for high accuracy calibration and modelling required in foreground subtraction has led to alternate methods of detecting the 21 cm signal, e.g. methods that attempt to *avoid* foregrounds rather than subtracting them. We illustrate this concept in the following.

In Sect 3.2 we expressed the power spectrum in terms of the delay spectrum. We defined the delay spectrum of a single baseline as:

$$\tilde{V}_{pq}(\tau) = \int_{\nu_1}^{\nu_2} V_{pq}(\nu) W(\nu) e^{-2\pi i \nu \tau} d\nu, \quad (3.38)$$

where

$$V_{pq} = \int \int E_p(l, m, \nu) E_q^*(l, m, \nu) I_{\nu}(l, m, \nu) e^{-2\pi i (u_p l + v_p m)} dl dm. \quad (3.39)$$

Note that, by looking at the power spectrum in frequency, we are actually measuring the power spectrum along the line of sight distance through the Universe (see Sect 3.2). For a flat spectrum

point source, the delay spectrum of a single baseline is a Dirac delta function centred on the geometric delay of the source τ_s . However, if the source spectrum is not flat, its delay transform will have a range of values centred on the geometrical delay (see Fig 3.2). As long as the sky emission remains smooth in frequency, it is expected that the delay spectrum is bound to a maximum delay set by the horizon limit τ_{\max} (Parsons et al., 2012):

$$\tau_{\max} = \frac{|\mathbf{b}|}{c}. \quad (3.40)$$

Smooth-spectrum foreground emission is therefore bound to a maximum delay that is baseline dependent. The delay spectrum from four baselines with varying length is shown in Fig 3.5. The baseline length is proportional to k_{\perp} , therefore, the foreground power spectrum is expected to be confined to a specific region which assumes a wedge-like shape in k space defined as:

$$k_{\parallel} \leq \frac{H(z)D(z)}{c(1+z)}k_{\perp}, \quad (3.41)$$

and this represents the k_{\parallel} horizon limit (Fig 3.6). The EoR signal is fluctuating on scales of a few MHz (Parsons et al., 2012; Thyagarajan et al., 2013; Pober et al., 2013) and is, therefore, expected to extend beyond the horizon limit, the so-called *EoR window*. The principle behind avoidance indeed is that the EoR power spectrum can be measured in the EoR window without foreground contamination and without the need to model foreground sources.

In practice, smooth spectrum foregrounds are corrupted by instrumental effects. The calibration process is an attempt to correct for these corruptions. As we have discussed in Sect 3.1.5, the calibration process makes use of a sky model to correct for instrumental effects (Smirnov, 2011). Sky models are built from catalogues of compact sources of known properties, and often cover an area larger than the field of view of the array (Yatawatta et al., 2013; Pober et al., 2016). The sky model ideally should contain the entire sky emission. However, sky models remain incomplete as source catalogues are insufficient at fully characterising their properties (Grobler et al., 2014; Wijnholds et al., 2016). Errors in calibration due to incomplete sky models lead to an overall leakage of foreground power into the EoR window (Ewall-Wice et al., 2017).

In a transit array, the pointing direction of the array is defined by digitally introducing different delays to antenna measurements. The resulting primary beam has noticeable changes over

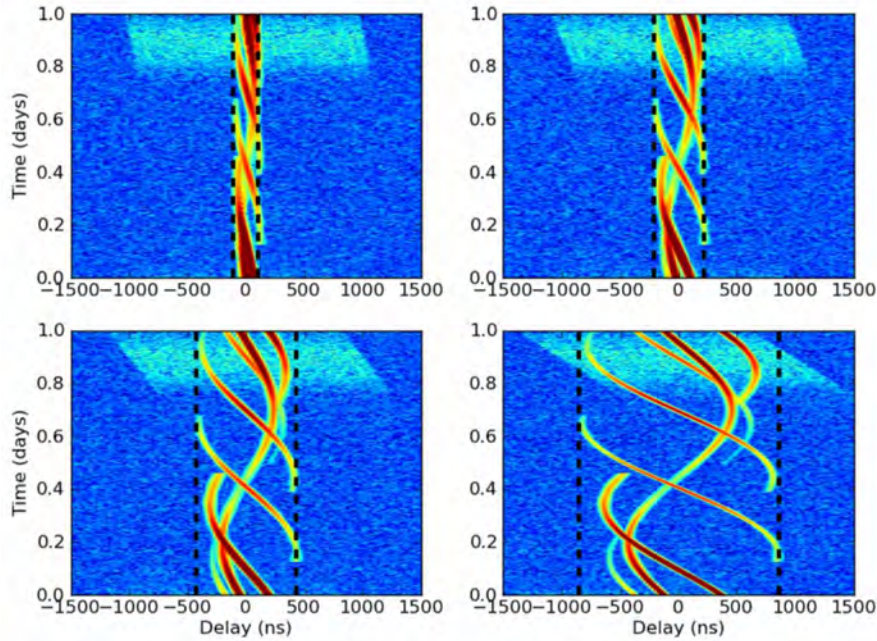


Figure 3.5: Simulated delay spectra for four baselines with differing lengths: 32 m (top left), 64 m (top right), 128 m (bottom left) and 256 m (bottom right). The dashed-lines correspond to the maximum geometric delay. Smooth-spectrum foreground emission is bound to the horizon limits, whereas the EoR signal (light blue regions) extends beyond them (from [Parsons et al., 2012](#)).

the observing time. This results in an apparent variable sky, with large variations occurring away from the pointing direction, due to variable side lobes ([Bhatnagar et al., 2008](#); [Bernardi et al., 2015](#)). If the primary beams are different, side lobe variations can be as large as large as 30% in some cases ([Neben et al., 2016](#)). And if the primary beam effects are not sufficiently corrected for, it can bias the calibration solution, thus corrupting foreground spectra.

3.5 Detection of the 21 cm signal using the power spectrum of the bi-spectrum phase

In the previous section, we discussed how instrumental effects (including calibration errors) corrupt intrinsic smooth foregrounds and may invalidate the assumptions behind avoidance. [Thya-](#)

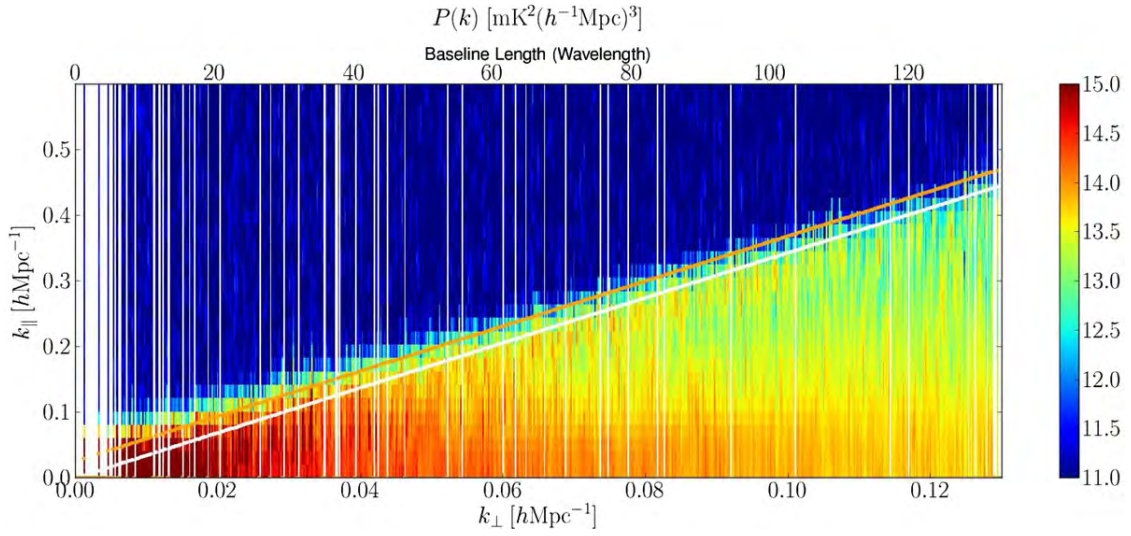


Figure 3.6: Example of foreground wedge in $(k_{\parallel}, k_{\perp})$ space, from a 150 MHz observation (Pober et al., 2013). We can see that most of the power is confined below the horizon (white) line, which is proportional to the baseline length. Beyond the horizon, in the EoR window, the power drops by ~ 4 orders of magnitude. We also note that the foreground power leaks slightly beyond the horizon - the orange line indicates a 50 ns delay beyond the horizon.

garajan et al. (2018) propose to detect the 21 cm signal using *closure phases*. The idea behind the use of closure quantities is that they are insensitive to direction independent calibration effects and, therefore, circumvent the problem of corrupting foreground properties - at least in principle.

The bispectrum C_{ijk} is defined as the triple product of three visibilities from baselines (ij, jk, ki) :

$$C_{ijk} = V_{ij}V_{jk}V_{ki}, \quad (3.42)$$

where indices i, j, k are antenna labels. The closure phase is defined as the complex phase of the bispectrum. In this section, we will consider single-polarization visibilities and assume that gains can be factored into antenna-based gains, and that they are not baseline-based. If we define g as a complex number that is the inverse of the antenna gain, calibrated visibilities V can be written as:

$$V_{ij} = g_i V_{ij}^O g_j^* = |g|_i e^{i\phi_i} |V_{ij}^O| e^{i\phi_{ij}^O} |g|_j e^{-i\phi_j}, \quad (3.43)$$

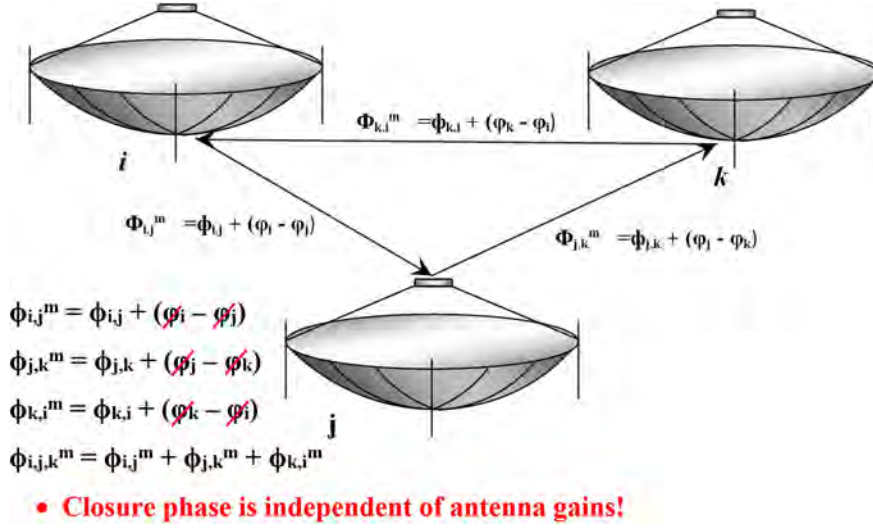


Figure 3.7: Schematic representation of the closure phase.

where V^O is the observed visibility (i.e. the correlator output). The bispectrum then becomes:

$$\begin{aligned}
 C_{ijk} &= |g_i| e^{i\phi_i} |g_j| e^{i\phi_j} |g_k| e^{i\phi_k} |V_{ij}^O| e^{i\phi_{ij}^O} |V_{jk}^O| e^{i\phi_{jk}^O} |V_{ki}^O| e^{i\phi_{ki}^O} |g_j| e^{-j\phi_j} |g_j| e^{-i\phi_j} |g_k| e^{-i\phi_k} \\
 &= |g_i|^2 |g_j|^2 |g_k|^2 |V_{ij}^O| |V_{jk}^O| |V_{ki}^O| e^{i(\phi_{ij}^O + \phi_{jk}^O + \phi_{ki}^O)},
 \end{aligned} \tag{3.44}$$

as the antenna-gain phases cancel out in the second step.

The closure phase is defined as the phase term (exponent) of the visibility bispectrum:

$$\phi_{\nabla} = \phi_{ij}^O + \phi_{jk}^O + \phi_{ki}^O, \tag{3.45}$$

and we have shown the well-known property that it is independent of calibration (Fig 3.7).

Although closure quantities are immune to calibration errors, their foreground contribution still needs to be separated from the cosmological signal. [Thyagarajan et al. \(2018\)](#) performed simulations of closure spectra that include foregrounds and a fiducial 21 cm signal. They simulated a 14.6 m baseline including an idealized HERA primary beam and found that closure spectra remain relatively smooth across most of the HERA observing band (Fig 3.8). Conversely, the EoR closure spectrum highly fluctuates along frequency. This analogy with the behaviour of the delay transform suggested that an avoidance-like approach may be able to separate the foreground closure spectra from the 21 cm closure spectra. They, therefore, defined the delay

transform Ξ :

$$\Xi(\tau) = \int \xi_{\nabla}(\nu) W(\nu) e^{2\pi i \nu \tau} d\nu, \quad (3.46)$$

where ξ is the complex closure spectrum:

$$\xi_{\nabla}(\nu) = e^{i\phi_{\nabla}(\nu)}, \quad (3.47)$$

and $W(\nu)$ is a window function (typically a Blackman-Harris function, [Parsons et al., 2012](#); [Thyagarajan et al., 2013](#)).

The power spectrum of the bispectrum phase P_{∇} can therefore be defined as ([Thyagarajan et al., 2018](#)):

$$P_{\nabla}(k_{\parallel}) = \Re e \left\{ \Xi_{\nabla}(\tau) \Xi_{\nabla'}^*(\tau) \right\} \left(\frac{\Delta D}{B_{\text{eff}}^2} \right), \quad (3.48)$$

where $\Delta D = \Delta D(z)$ is the comoving depth along the line of sight corresponding to B_{eff} , $\Re e$ denotes the real part and ∇ denotes a triad. As in section 3.4, by looking at the power spectrum of the bispectrum phase in frequency, we are actually measuring the power spectrum along the line of sight distance through the Universe. The units of the power spectrum of the bispectrum phase are h^{-1} Mpc.

Figure 3.9 shows that the 21 cm power spectrum of the bispectrum phase can be separated from foregrounds at $|k_{\parallel}| \geq 0.5 h \text{ Mpc}^{-1}$ for the bands centred at $z = 8.5$ and $z = 7.1$. At $z = 10.4$, the foreground bispectrum phase seems to have too much structure to be separated from the 21 cm signal.

In summary, [Thyagarajan et al. \(2018\)](#) offer an alternative way to detect the 21 cm signal using the bispectrum phase. This method has the appealing feature of avoiding the need for accurate calibration and is expected to work as long as the foreground closure spectra remain smooth in frequency.

3.6 Thesis motivation

As we discussed in the Sect 3.4, foreground separation (either in the form of subtraction or avoidance) is hindered by instrumental effects. Such errors can be in the form of direction independent

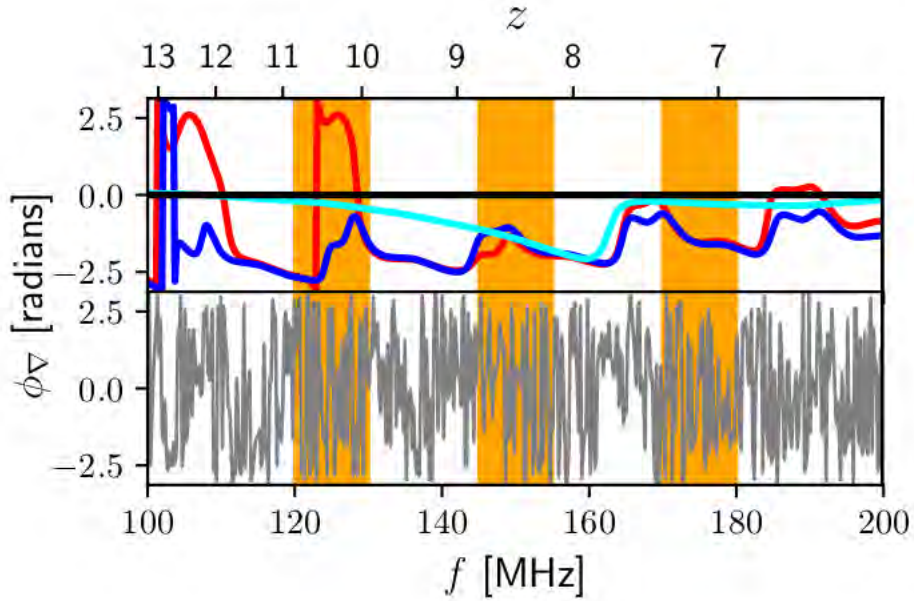


Figure 3.8: Closure spectra of various sky components: a single point source (black line), point sources only (cyan), diffuse emission (blue), diffuse emission and point sources (red), and the 21 cm signal (gray). The orange bands denote the frequency sub-bands centred on 125, 150 and 175 MHz respectively. Each sub-band is 10 MHz wide (from [Thyagarajan et al., 2018](#)).

calibration errors ([Trott et al., 2016](#); [Barry et al., 2016](#); [Procopio et al., 2017](#)), or direction dependent errors like, for example, poorly known or inaccurate primary beams ([Neben et al., 2016](#); [Ewall-Wice et al., 2017](#); [Dillon et al., 2018](#)). While closure phases are unaffected by direction independent calibration errors, they are not immune to direction dependent effects. In the HERA case, a prominent source of direction dependent errors may be due to primary beams that can be different from dish to dish, due to mutual coupling effects generated by the closely packed configuration.

In this thesis, we used simulations of HERA primary beams that include mutual coupling effects ([Fagnoni et al., 2019](#)) to quantify their impact on the detection of the 21 cm signal through the power spectrum of the bispectrum phase.

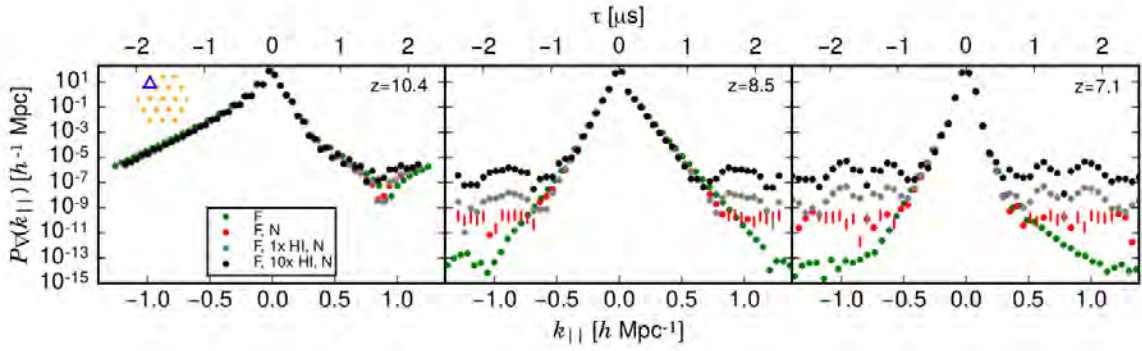


Figure 3.9: Power spectrum of the bispectrum phase of the main components shown in Fig 3.8: foregrounds only (green circles), foregrounds and instrumental noise (red), foregrounds, instrumental noise and a fiducial 21 cm signal (grey), foregrounds, instrumental noise and an optimistic 21 cm signal (black). A coherent average of $N_m \sim 10^6$ measurements of a 14.6 m triad (highlighted on a HERA-19 layout on the top left corner) was considered. For a detailed review of the simulations see Thyagarajan et al. (2018). Left panel is centred at $z = 10.5$, central panel at $z = 8.5$ and right panel at $z = 7.1$. The detection of the bispectrum phase of a fiducial EoR model is expected to be possible at $z = 8.5$ and $z = 7.1$ respectively (from Thyagarajan et al., 2018).

Simulations of foreground closure spectra

In this chapter, we study closure spectra using different sky models. We study how closure spectra vary as sky models become more realistic. We show the independence of the closure spectra from antenna based corruptions. We eventually study the impact of the primary beams on closure spectra.

4.1 Closure spectra of sky models

We simulate sky models composed of point sources centred at right ascension (RA) $\alpha = 3^{\text{h}}20^{\text{m}}06^{\text{s}}$ and declination (DEC) $\delta = -30^{\circ}46'51''$. Positions and flux density values are taken from the GaLactic and Extragalactic All-sky MWA (GLEAM) survey catalogue ([Hurley-Walker et al., 2017](#)). The GLEAM catalogue covers the HERA bandwidth, i.e. 100 – 200 MHz, it is also the most complete catalogue with the largest sky area at low frequencies to date. To keep our sky models simple, we limit the field to $30^{\circ} \times 30^{\circ}$, and use only sources brighter 5 Jy at 151 MHz. Our simulated sky patch, therefore, contains a total of 29 sources.

We use equation [3.17](#) to simulate sky models, but we remove the effect of the primary beam

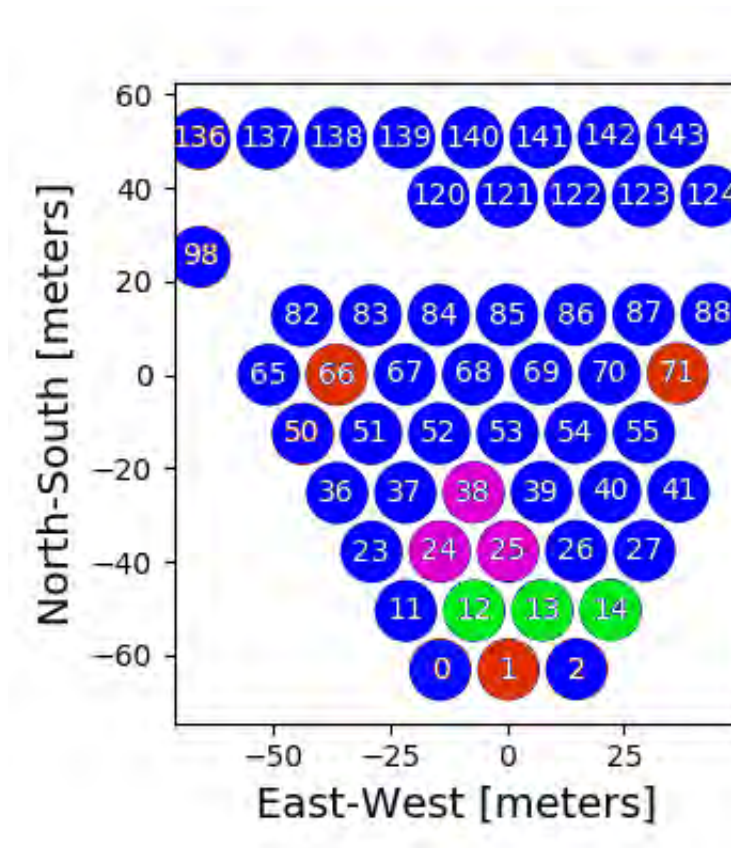


Figure 4.1: HERA array configuration used in this thesis. The number denote dishes in the array. Colours denote antenna in simulated triads: 72 m equilateral triad (red), 14 m equilateral triad (purple) and 29 m linear triad (green).

Model	Number of sources
Model 1	1
Model 2	2
Model 3	5
Model 4	10
Model 5	20
Model 6	29

Table 4.1: Number of point sources included in each simulated sky model.

Triad type	$f(^{\circ})$ [degrees]
14 m Equilateral triad	7.84
29 m Linear triad	3.95
72 m Equilateral triad	1.58

Table 4.2: Resolution of the largest baseline in each triad type.

by setting $\mathbf{E}_p = \mathbf{E}_q = 1$. Simulated visibilities are given by:

$$\mathbf{V}_{pq}(t, \nu) = \sum_{s=1}^{N_s} \mathbf{X}_{s,pq}. \quad (4.1)$$

We study the closure spectra of different sky models, with a varying number of sources. We simulate a total of six sky models labelled 1, 2, 3, 4, 5 and 6. Figure 4.1 shows the array layout used in simulations, and Fig 4.2 shows a dirty image of each model, made using *clean* in the (*Common Astronomy Software Application*) (CASA, McMullin et al., 2007). Images have a size 256×256 with a pixel resolution of $10 \text{ arcmin pixel}^{-1}$. In Table 4.1, we also show the number of sources for each sky model. We simulate closure spectra from three triads: 14 m equilateral triad (14EQ), 29 m linear triad (29LN) and 72 m (72EQ) equilateral triad. The EQ14 triad consist of antennas [24, 25, 38], 29LN [12, 13, 14] and 72EQ [1, 66, 71], shown in Fig 4.1. The corresponding closure spectra are shown in Fig 4.3.

Before discussing these results, we consider a simple example of a sky model with a point source located at σ_0 with a brightness I_0 . The brightness of the source can be described by a Dirac delta function $I_{\nu}(\sigma) = I_0\delta(\sigma - \sigma_0)$ and the measured visibility by antennas a, b are:

$$V_{ab} = I_0 e^{-2\pi i \mathbf{d}_{ab} \cdot \sigma_0}. \quad (4.2)$$

The visibilities measured by antenna b, c and c, a are given by:

$$V_{bc} = I_0 e^{-2\pi i \mathbf{d}_{bc} \cdot \sigma_0}. \quad (4.3)$$

$$V_{ca} = I_0 e^{-2\pi i \mathbf{d}_{ca} \cdot \sigma_0}. \quad (4.4)$$

The bi-spectrum is therefore given by (see equation 3.44):

$$C_{abc} = I_0^3 e^{-2\pi i (\mathbf{d}_{ab} + \mathbf{d}_{bc} + \mathbf{d}_{ca}) \cdot \sigma_0}. \quad (4.5)$$

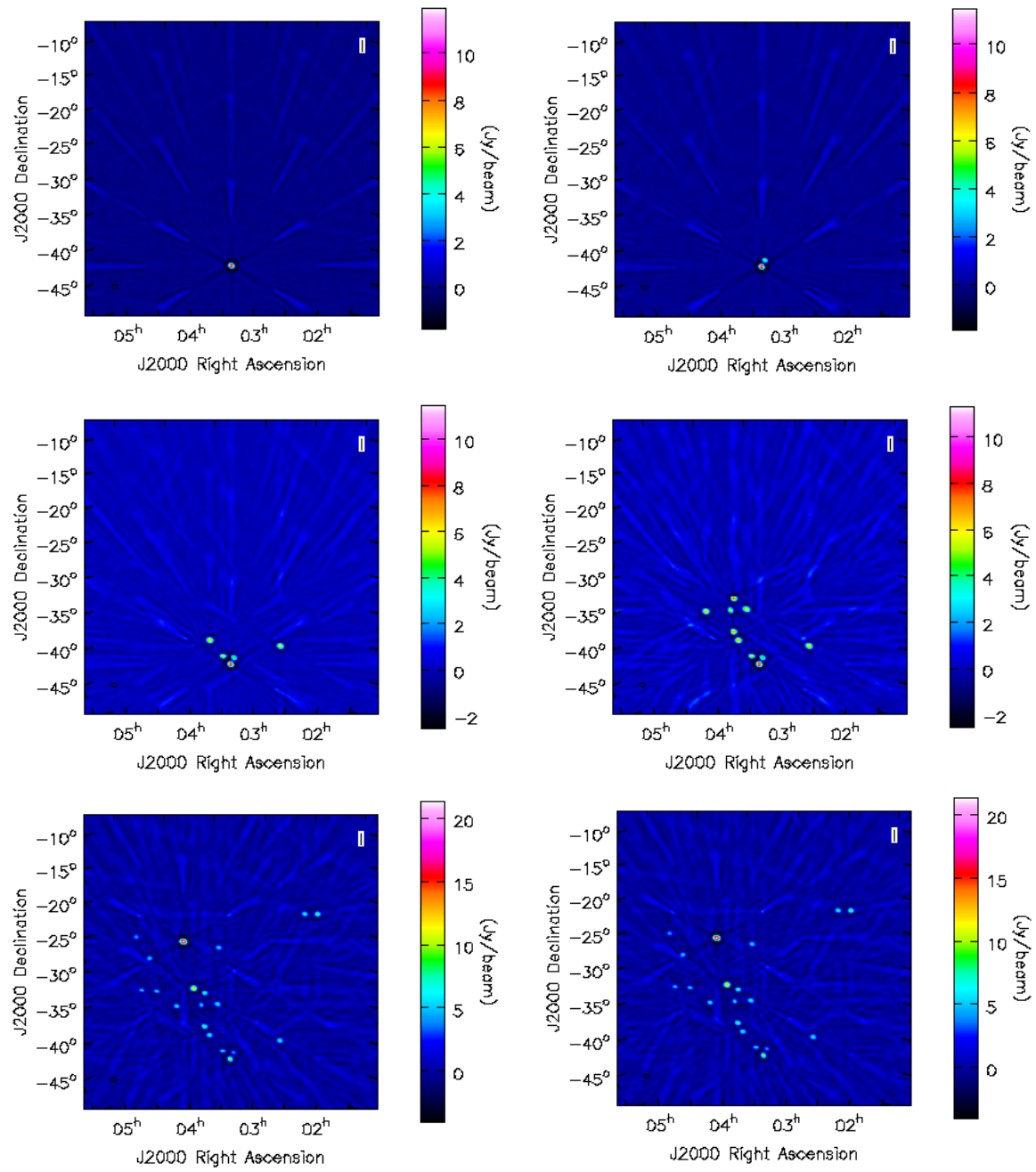


Figure 4.2: Dirty images of simulated sky models at 150 MHz: model 1 (top left), model 2 (top right), model 3 (left centre), model 4 (right centre), model 5 (left bottom) and model 6 (right bottom).

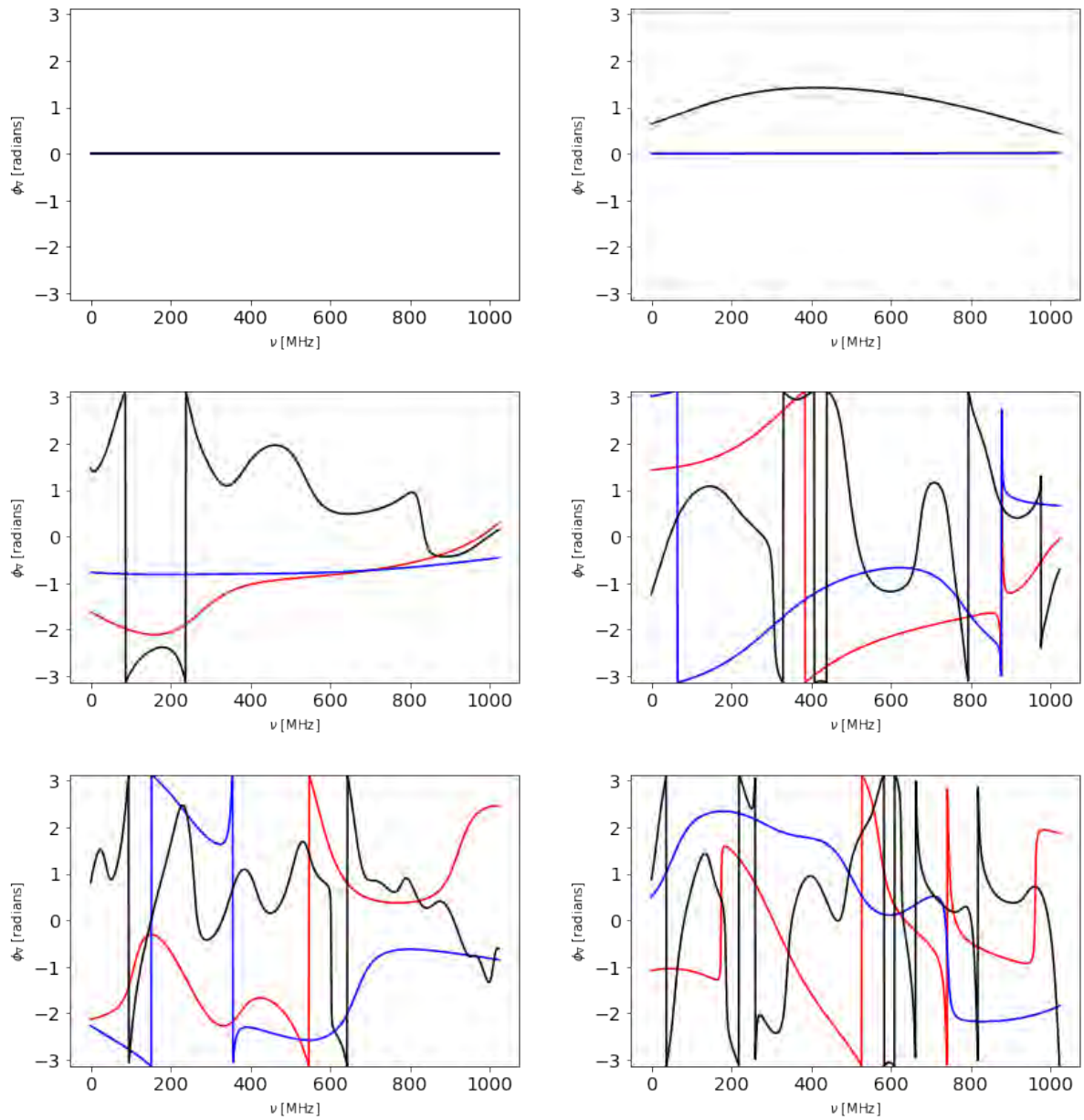


Figure 4.3: Simulated closure spectra of sky models (see Fig 4.2) from the three triad types shown in Fig 4.1. Top left panel: model 1, top right panel: model 2, left centre panel model 3, right centre panel: model 4, left bottom panel: model 5 and right bottom panel model 6. The black line shows the closure spectra from the 72 m equilateral triad (EQ72), the red line shows the closure spectra from the linear triad (LN29), and the blue line shows the closure spectra from the 14 m equilateral triad (EQ14).

The vectors \mathbf{d}_{ab} , \mathbf{d}_{bc} , \mathbf{d}_{ca} form a triangle and therefore their sum is a null vector. The bi-spectrum is given by:

$$C_{abc} = I_0^3. \quad (4.6)$$

This shows that the closure phase of a point source is zero, irrespective of source position and triad type. For an asymmetric sky model, for example, a model with two or more sources with different flux densities, the closure phase will not be zero and depend upon the source orientation.

From the results in Fig 4.3, we can see that closure spectra of model 1 are zero for all simulated triads, as expected. For model 2, however, we find the closure spectra from the 72EQ triad deviate from zero unlike those from 14EQ and 29LN triad. We interpret this as an effect due to the different baseline separation. Each baseline is sensitive to spatial scales comparable to f i.e. the resolution of the baseline, given by:

$$f \propto \frac{\lambda}{|\mathbf{b}|}, \quad (4.7)$$

where λ is the observing wavelength and $|\mathbf{b}|$ is baseline length, for review see [Thompson et al. \(2008\)](#). Table 4.2 shows the value of f , for the largest baseline in each triad at 150 MHz. The 72EQ triad is sensitive to smaller scales compared to baselines in other triads. 14EQ and 29LN triads are not sensitive to the distance between point sources in model 2. When we consider closure spectra of model 3, we find that the closure spectra from triads with the longest baseline (EQ 72), has more frequency structure than triads with smaller baselines (EQ14 and LN 29). Lastly, the closure spectra of complex sky models (model 6), i.e. large number of point sources, shows a pronounced frequency structure compared to simple sky models (model 3).

4.2 Closure spectra simulations with direction independent effects

In this section, we validate our simulations against the independence of closure spectra to antenna based corruptions. We make use of calibration solutions that were generated using the absolute calibration pipeline developed by Kern (2018). The model visibility data was corrupted using antenna gain solutions $B(\nu)$, G_p^{phase} , G_p^{amp} and K_p derived from actual HERA observations (Kern, 2018). The corrupted model visibilities V^c are obtained as:

$$V_{pq}^c(\nu) = B_p(\nu) G_p^a G_p^p k_q V_{qp}^m(\nu) (B_q(\nu) G_q^a G_q^p K_q)^*, \quad (4.8)$$

where (p, q) indicate the antenna pair, V^m and V^c the model and corrupted model visibilities respectively and $B(\nu)$, G^a , G^p , K_q are the per-antenna bandpass, gain amplitude and phase and delays respectively.

Figure 4.4 shows the visibility amplitude and phase for the 14 m baseline [11,12] i.e. antenna 11 and 12 (see Fig 4.1) for model and corrupted visibilities, respectively. As expected, visibilities from model and corrupted model data differ largely in phase and in amplitude. The closure spectra from both model and corrupted model visibilities are shown in Fig 4.5. Indeed as expected closure spectra from both model and corrupted model visibility is exactly the same for all triads. Thus we show through our simulations the independence of the closure spectra on antenna based gains.

4.3 Closure spectra simulations with direction dependent effects

In this section, we study the impact of the primary beam on closure spectra. Before we begin, we first define some relevant quantities used in the following. We use a normalised primary beam pattern to simulate observations. The normalised primary beam pattern at a frequency ν is given

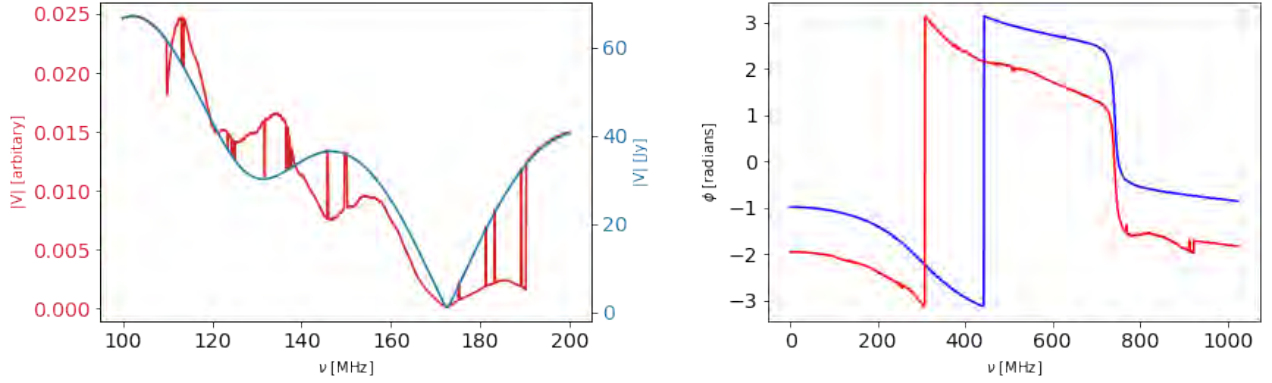


Figure 4.4: Left: Comparison between model (blue) and corrupted (red) visibility amplitude $|V|$ from 14 m baseline pair [11, 12]. Right: same as left but for the visibility phase.

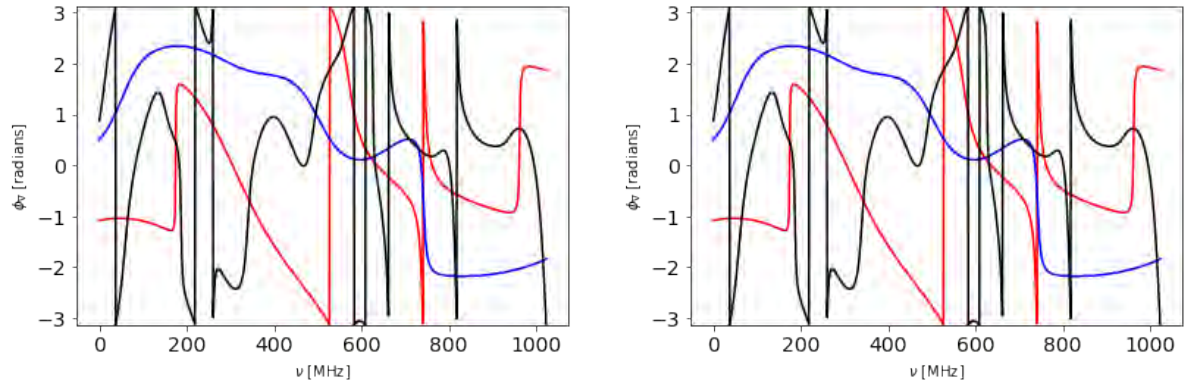


Figure 4.5: Simulated closure spectra for model 6: closure spectra from corrupted (left) and model (right) visibilities. The black line shows the closure spectra from the 72 m equilateral triad (EQ72), the red line shows the closure spectra from the linear triad (29LN), and the blue line shows the closure spectra from the 14 m equilateral triad (EQ14).

by:

$$E_n(\theta, \phi) = \frac{E(\theta, \phi)}{\max(|E(\theta, \phi)|)}, \quad (4.9)$$

where

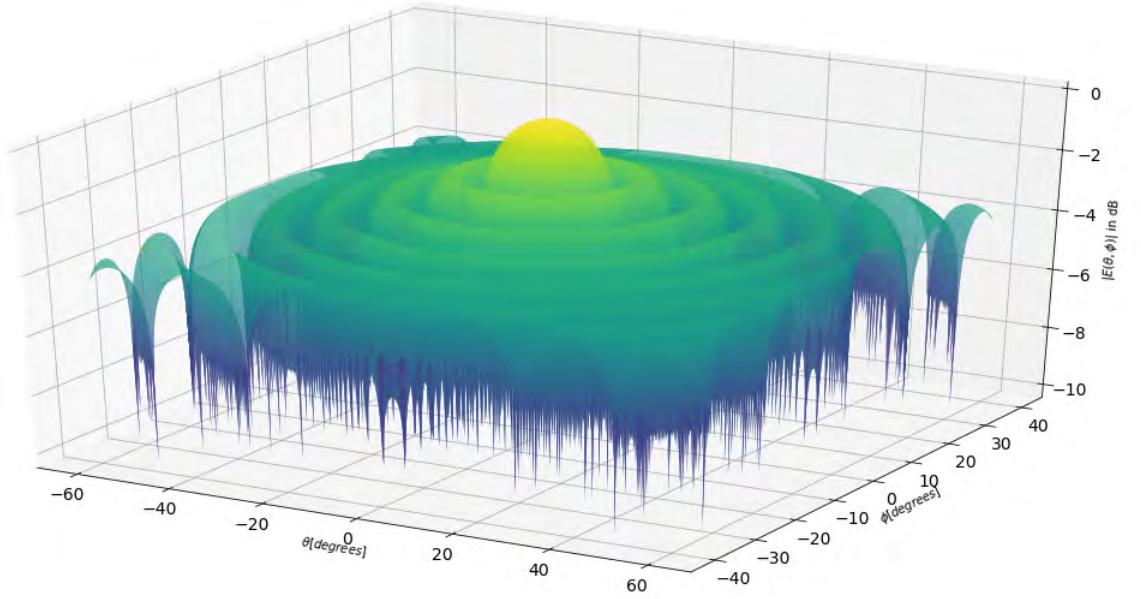


Figure 4.6: Normalised Airy power pattern in dB in units.

$$\theta = \alpha - \alpha_0, \quad (4.10)$$

$$\phi = \delta - \delta_0, \quad (4.11)$$

with α_0 and δ_0 are RA and DEC coordinates of the pointing direction. We also define the dB gain of the primary beam as:

$$G_{dB}(\theta, \phi) = 10 \log E_n^2(\theta, \phi). \quad (4.12)$$

As the HERA dish has an approximately circular aperture (see Fig 2.7) we model its primary beam using an *Airy power pattern*. The intensity I_ν of an Airy power pattern is given by:

$$I_\nu(\gamma) = I_0 \left[\frac{2J_1(k\rho \sin \theta)}{k\rho \sin \theta} \right] \quad (4.13)$$

where $\gamma = \sqrt{\theta^2 + \phi^2}$, is the radial distance from pointing direction, I_0 is the maximum intensity, ρ is the aperture radius, $k = 2\pi\nu/c$ is the wavenumber, and J_1 is the Bessel function of the first

kind. The nulls of J_1 occur at values $x = [3.8317, 7.0156, 10.1735\dots]$, hence the first null occurs at

$$k\rho \sin \gamma = 3.8317, \quad (4.14)$$

and for small values of γ this becomes

$$\gamma \approx \frac{3.83}{k\rho} = \frac{3.83c}{2\pi\nu\rho}. \quad (4.15)$$

Thus, the null positions decreases with increasing frequency. For our simulated Airy power pattern beam the first null is at $\gamma \approx 20^\circ$ at $\nu = 100$ MHz. The normalised Airy power pattern beam is shown in Fig 4.6.

We simulate four sky models A1, A2, A3 and A4 whose sources are distributed on a $110^\circ \times 70^\circ$ field of view. We first place sources on the main lobe of the beam and progressively add sources positioned on the sidelobes, and we apply the primary beam to simulated sky models. Figure 4.7 shows the distribution of sources in each model on the beam. All simulated point sources have a flux density of 1 Jy and a spectral index $\alpha = 0.7$. We simulate observations with a 14 m equilateral triad. Note that, the direction dependent effects i.e. antennas primary beam are the same for all simulated antennas in this section.

Figure 4.8 shows the closure spectra from simulated sky models with and without the primary beam. We find the closure spectra of models A1, A2, A3 with beam applied (red) to have simple frequency structure compared to sky models without beam (blue). This is because, sources located on sidelobes are attenuated by the beam, and their contribution to the overall closure spectra is reduced. As a result sources on the main lobe dominate the closure spectra.

Closure spectra for model A4 have notably more frequency structure, though sources are attenuated by the beam. In this case, individual sources have a significant contribution to closure spectra, and thus influence the frequency structure in the closure spectra. In addition, the spectral response of the beam at sidelobes also introduces frequency structure. These two effects combined results in the observed frequency structure in closure spectra of model A4 (red). Most notably as well, due to beam attenuation, the closure spectra of model A4 with beam applied varies in the range $[-0.01, 0.01]$, which is 100 times smaller than the range of closure spectra from the same sky model without beam (blue).

In conclusion, in this chapter we have learnt that closure spectra of complex sky models typically show a pronounced frequency structure. This is also true for triads with large baselines. Lastly, we have also learnt that the primary beam effectively attenuates sources on the sidelobes, and thus minimises their impact on the closure spectra, and that this results in smooth closure spectra. However, in the case that there are only sources on the sidelobes, the closure spectra has a pronounced frequency structure, due to first, the significant contribution of each source to the closure spectra as well as the spectral response of the beam at the sidelobes.

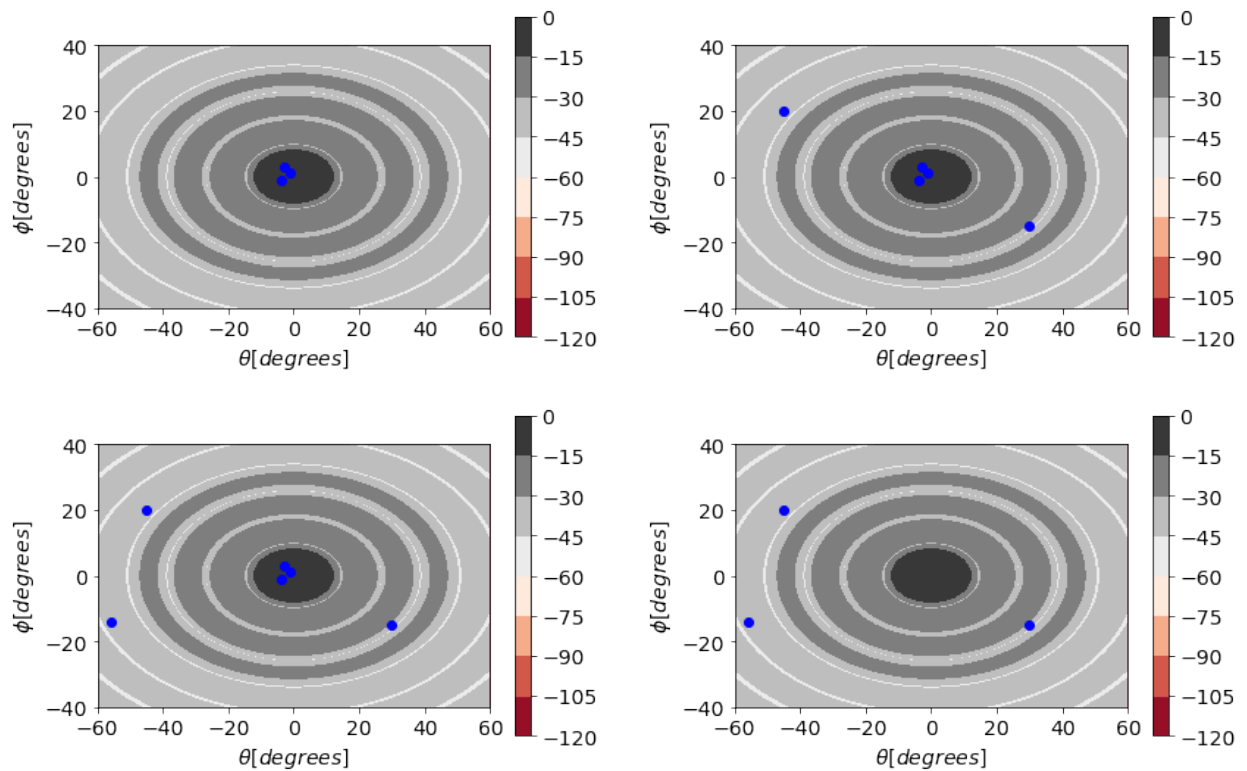


Figure 4.7: Airy power pattern at $\nu = 100$ MHz (dB units). Blue dots mark the point source position for each sky model considered. Model 1A (top left), Model 2A (top right), Model 3A (bottom left) and Model 4A (bottom right).

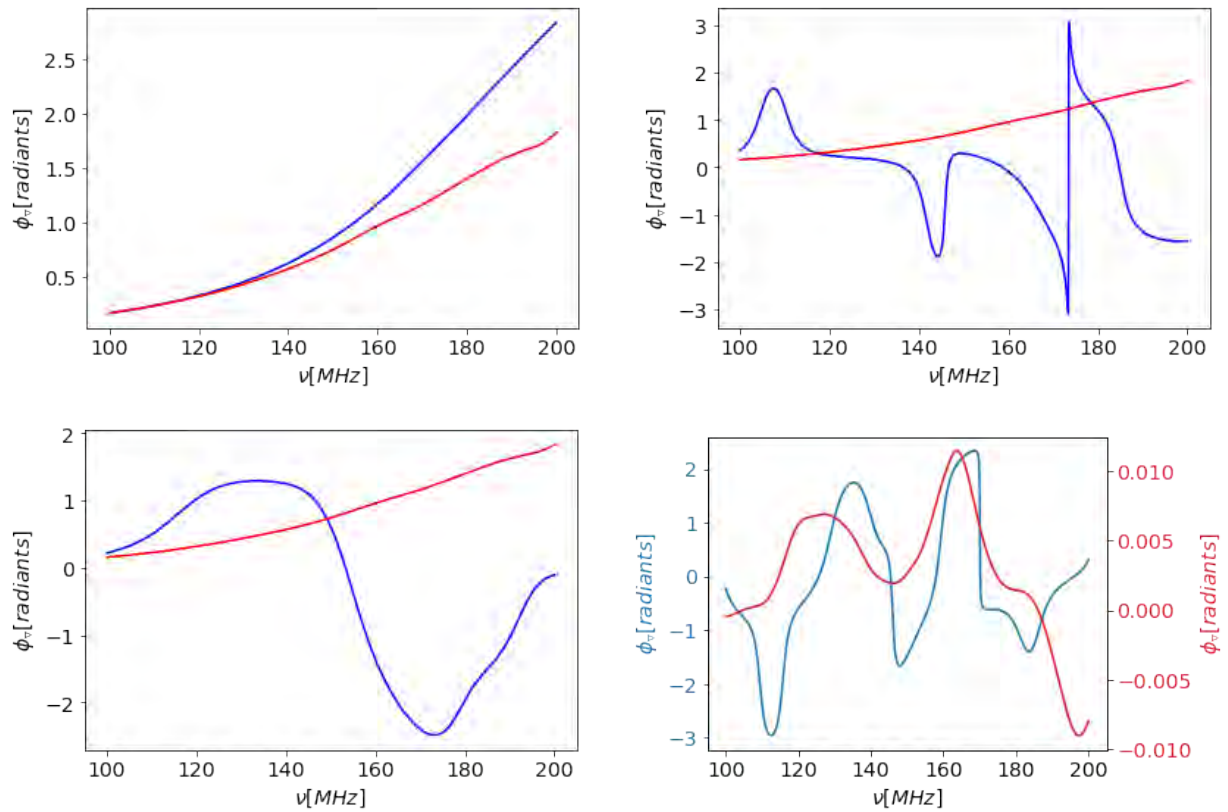


Figure 4.8: Simulated closure spectra from 14EQ of four sky models shown in Fig 4.7. Model 1A (top left), Model 2A (top right), Model 3A (bottom left) and Model 4A (bottom right). Red and blue lines show closure spectra for sky model with and without primary beam, respectively.

Simulations of foreground bi-spectrum phase using mutual coupling beams

In this section, we study the impact of primary beams affected by mutual coupling on the power spectrum of the bispectrum phase. We recall that when we consider primary beams in the RIME, visibilities V_{pq}^m measured by the antenna are defined as:

$$\mathbf{V}_{pq}(t, \nu) = \sum_s^{N_s} \mathbf{E}_{s,p}(t, \nu) \mathbf{B}_s(\nu) \mathbf{E}_{s,q}^H(t, \nu), \quad (5.1)$$

and the closure spectra depends on the brightness of the source \mathbf{B} and antenna primary beam patterns \mathbf{E}_p and \mathbf{E}_q . If the antenna primary beams are different from each other, i.e. $\mathbf{E}_p \neq \mathbf{E}_q$, the phase of complex beams does not cancel out. *Mutual coupling* amongst antennas introduces variations in the antenna primary beam response that depend upon the position of the antenna in the array, and we expect closure spectra to be dependent - amongst other things - on the phase of each primary beam in this case.

Mutual coupling describes the interactions between antennas in an array (e.g., [Craeye & González-Ovejero, 2011](#)). These interactions include multi-path propagation as a consequence

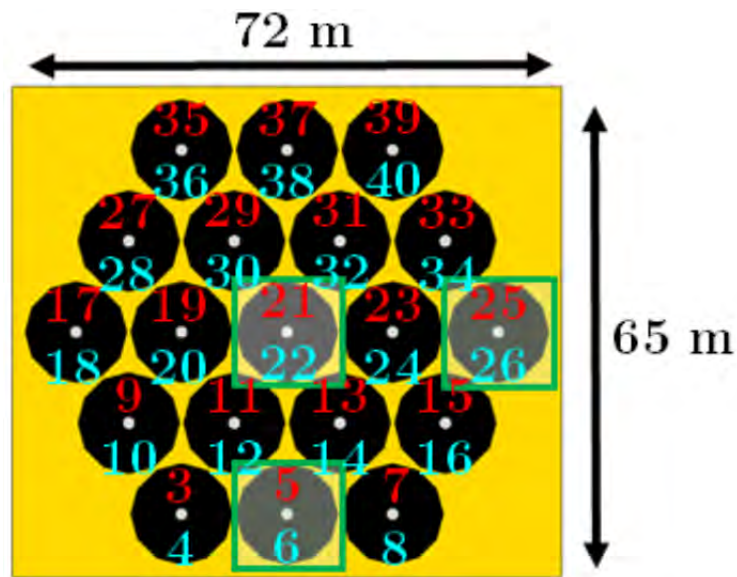


Figure 5.1: HERA 19 array layout. In this work, we used the simulated primary beam pattern corresponding to label 22, i.e. the Y polarization (North-South) for a central dish and a beam pattern that corresponds to the Y polarisation of an edge antenna like label 26 (from [Fagnoni et al., 2019](#)).

of signals reflected by neighbouring antennas. [Fagnoni et al. \(2019\)](#) carried out simulations of HERA dishes which included the receiving system and the effects of mutual coupling for two polarisations, i.e. X and Y , for the antenna layout shown in Fig 5.1.

[Fagnoni et al. \(2019\)](#) showed that mutual coupling eventually introduces extra sidelobe ripples and increases the sidelobe level by 2 – 4 dB (Fig 5.2 and 5.3). It also changes the gain at zenith as a function of frequency up to ~ 0.3 dB (Fig 5.3) with respect to the unperturbed beams. The beam value at zenith oscillates with a periodicity of about 20 MHz, which corresponds to reflections occurring at 15 m, approximately the distance between the centre of two dishes. These effects lead to further deviations from the smooth ideal beam response. Lastly, antennas may experience a varying degree of mutual coupling and, as a consequence, an antenna at the edge array has an asymmetric primary beam pattern since one side of antenna experiences more mutual coupling, i.e. side facing other stations, than the other side where there are no stations (Fig 5.3).

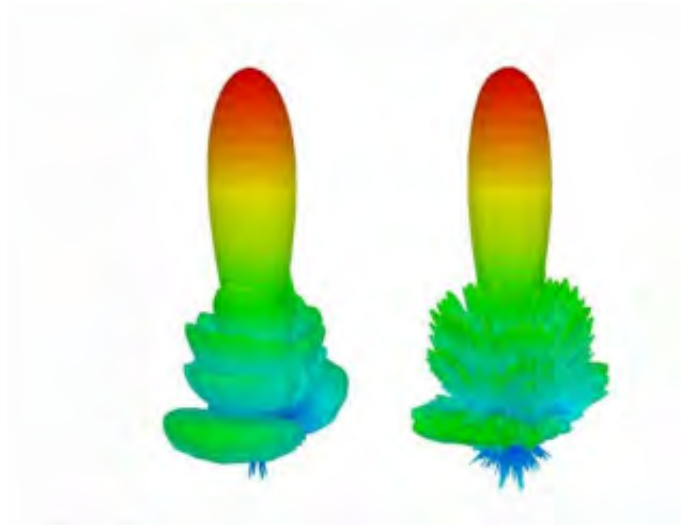


Figure 5.2: 3D primary beam pattern of a HERA dish without (left) and with (right) mutual coupling (from [Fagnoni et al., 2019](#)). The increased sidelobe structure is particularly visible.

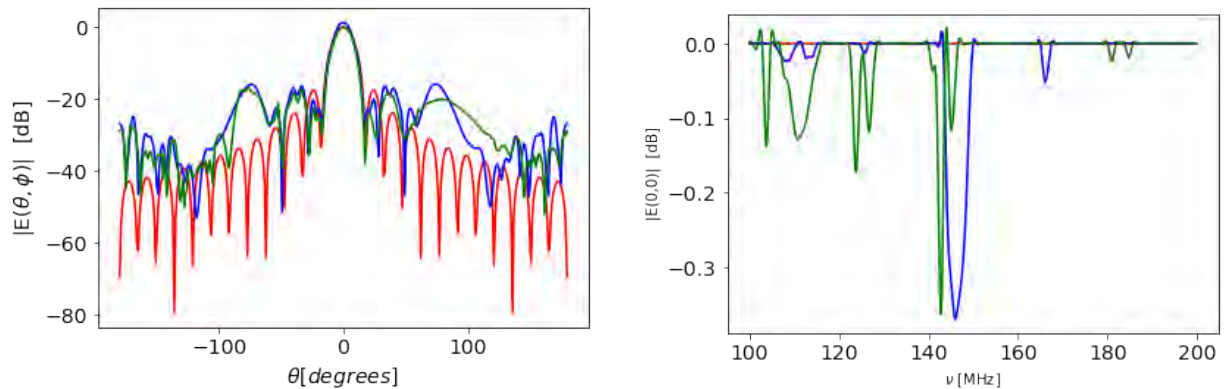


Figure 5.3: Left panel: beam profiles at $\nu = 100$ MHz: Airy power pattern (red), dish 22 beam (blue) and dish 26 beam (green, see Fig 5.1), for the Y polarisation (North-South) of a HERA dish. Right panel: gain variation at zenith, i.e. $(\theta = 0, \phi = 0)$ as a function of frequency for mutual coupling beams, in comparison to an Airy power pattern, which has a constant gain of 0 dB across frequency. We note the extra frequency structure introduced by mutual coupling across the observing bandwidth even within the main lobe of the beam

5.1 Simulations with perturbed primary beam

Before using the mutual coupling beams simulated by [Fagnoni et al. \(2019\)](#), we simulate an Airy power pattern, which we perturb to have similar features to the HERA mutual coupling beams. This exercise aims to decouple the various mutual coupling effects and gain a clearer intuition of their impact on closure spectra and power spectrum of the bispectrum phase. We first simulate the impact of enhanced sidelobe ripples and then the magnitude increase in sidelobe level.

We use *Gaussian Processes* (GP) to perturb the Airy power pattern beam. Before we proceed, we briefly review GP. We can draw sample functions $f(x)$ normally distributed around a *mean function* $m(x)$ with a *covariance function* $k(x, x')$. Gaussian processes are normally written as:

$$f(x) \sim GP(m(x), k(x, x')). \quad (5.2)$$

The mean function and the covariance function are defined as:

$$m(x') = \langle f(x') \rangle, \quad (5.3)$$

and

$$k(x, x') = \langle [(f(x) - m(x))(f(x') - m(x')))] \rangle, \quad (5.4)$$

respectively, where $\langle \rangle$ denotes the expectation value. Gaussian processes in this form are appropriate for continuous functions; however, in this thesis work, we make use of functions defined on a discrete domain, given by a vector \mathbf{x} . To generate sample functions $\mathbf{y} = f(\mathbf{x})$, normally distributed around a mean \mathbf{m} and covariance matrix \mathbf{K} :

$$\mathbf{y} \sim N(\mathbf{m}, \mathbf{K}), \quad (5.5)$$

we use a scalar Gaussian generator. We first compute the Cholesky decomposition i.e. the matrix square root \mathbf{L} of a positive definite symmetric covariance matrix $\mathbf{K} = \mathbf{L}\mathbf{L}^T$. Then we generate samples \mathbf{u} by making multiple calls to a normal distribution scalar generator:

$$\mathbf{u} \sim N(\mathbf{0}, \mathbf{I}), \quad (5.6)$$

where \mathbf{I} is the identity matrix. Sample functions \mathbf{y} are generated as follows:

$$\mathbf{y} = \mathbf{m} + \mathbf{L}\mathbf{u}, \quad (5.7)$$

which has a mean \mathbf{m} and covariance matrix $\mathbf{L}\langle[\mathbf{u}\mathbf{u}^T]\rangle\mathbf{L}^T = \mathbf{L}\mathbf{L}^T = \mathbf{K}$, since elements of \mathbf{u} are independent.

We use a *squared exponential* (SE) covariance matrix given by:

$$\mathbf{K}(x_a, x_b) = \sigma^2 e^{-\frac{(x_a - x_b)^2}{2l}} \quad (5.8)$$

where σ^2 is the variance, x_a and x_b are points on the domain \mathbf{x} , and l is the parameter that determines the characteristic length scale of variations. Small values of l , will result in high frequency variations of drawn sample functions \mathbf{y} on the domain \mathbf{x} . For an extensive review of Gaussian process and their wide applications see [Rasmussen & Williams \(2005\)](#).

We use GP to simulate beam models with varying frequency ripples, i.e. the number of ripples across the sidelobe region. We simulate three different sky models (Fig 5.4), where we randomly place 100 point sources in the main lobe and another 100 across the beam sidelobes. All sources have a 1 Jy flux density at 150 MHz and a spectral index $\alpha = 0.7$. We perturb the Airy power pattern sidelobes values, stored in vector $\mathbf{b} = \mathbf{E}(\nu_n, \theta_s, \phi_s)$ at positions (θ_s, ϕ_s) corresponding sky model sources shown in the top right panel of Fig 5.4 (sources only across sidelobes). That is, at each angular position the beam is perturbed at all frequencies and this perturbation is uncorrelated with different sky positions. We use equation 5.7 to obtain perturbed values $\mathbf{b}' = \mathbf{E}'(\nu_n, \theta_s, \phi_s)$:

$$\mathbf{b}' = \mathbf{b} + \mathbf{L}(\nu_{n,a}, \nu_{n,b}) \mathbf{u}, \quad (5.9)$$

where $\nu_{n,a}, \nu_{n,b}$ are points on a discrete frequency domain ν_n and $\nu_n = \nu/150$ MHz. We use $\sigma = 0.001$, and this sets the amplitude of the perturbations, i.e. the amplitude of the sidelobe ripples. We simulate two perturbed beam models E'_H and E'_L , where the characteristic length scale of variations was chosen to be $l = 0.001$ and $l = 1$ respectively. The resulting beams are shown in Fig 5.5.

We simulate noiseless visibilities for a 14 m equilateral triad, centred at 175 MHz ($z = 7.1$) with a $B = 30.77$ MHz, corresponding to an effective bandwidth $B_{eff} = 9.77$ MHz. The channel width is $df = 97.66$ kHz, i.e. same observing setup as HERA. We simulate three different triads ∇_{HHH} , ∇_{LLL} and ∇_{AAA} corresponding to primary beams E'_H , E'_L and E_A respectively, the

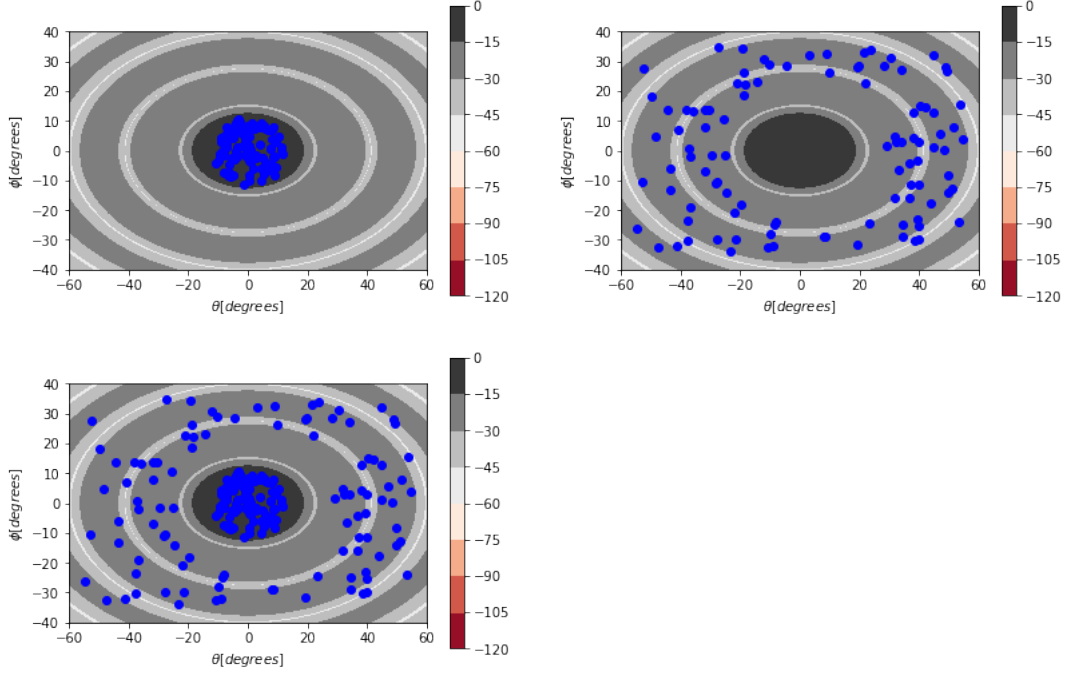


Figure 5.4: Airy power pattern beam at $\nu = 100$ MHz (dB units). Blue dots mark point source positions within the beam. The top left panel shows a sky model where sources are randomly distributed within the main lobe. The top right panel shows a sky model where sources are randomly distributed only across sidelobes. The bottom panel shows the combination of the two sky models, i.e. where sources appear both in the main lobe and in the sidelobes.

latter being the Airy power pattern. We quantify our results using closure spectra and the power spectrum of the bispectrum phase (Thyagarajan et al., 2018):

$$P_{\nabla}(k_{||}) = |\Xi_{\nabla}(\tau)|^2 \left(\frac{\Delta D}{B_{eff}^2} \right), \quad (5.10)$$

where we take the absolute value rather than the real part of the delay closure spectra as our simulations are noiseless.

Figure 5.6 shows the corresponding closure spectra and power spectra. Let us first consider closure spectra and power spectra for sky models with sources only across sidelobes. Due to sidelobe ripples, the closure spectra from triads with perturbed beams (∇_{HHH} and ∇_{LLL}) show a pronounced frequency structure in contrast to triad with the unperturbed beam (∇_{AAA}). Indeed,

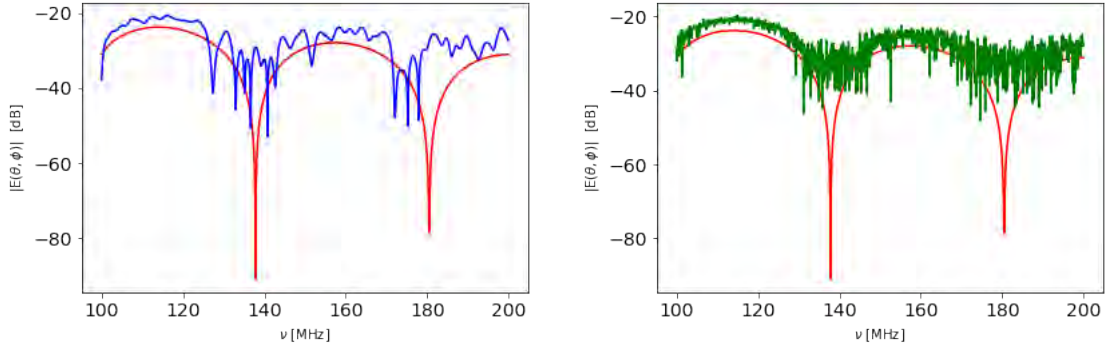


Figure 5.5: Left: gain amplitude as a function of frequency of the perturbed beam $E'(\nu, \theta_p, \phi_p)$ with $l = 1$ (blue line) and the Airy power pattern beam $E'_L(\nu, \theta_p, \phi_p)$ at the $(\theta_p, \phi_p) = (-18.9^\circ, 26.0^\circ)$ position. Right: same as left, but for the perturbed beam $E'_H(\nu, \theta_p, \phi_p)$ with $l = 0.001$ (green line). We note that ripples are much closely spaced with respect to the $l = 1$ case.

as expected, the ∇_{HHH} closure spectra shows more frequency structure compared to ∇_{LLL} .

Power spectra from triads ∇_{HHH} and ∇_{LLL} are also fairly different than the ∇_{AAA} case. The sidelobe frequency structure turns into a high power level at almost all k values. In particular, the power spectrum from triad ∇_{LLL} is 4 – 7 orders of magnitude higher than the power spectrum from triad ∇_{AAA} at $|k_{\parallel}| > 0.5 h \text{ Mpc}^{-1}$. The power spectrum from triad ∇_{HHH} has even more power at $|k_{\parallel}| > 0.5 h \text{ Mpc}^{-1}$, an approximately constant level that is ~ 10 orders of magnitude higher than the power spectrum from triad ∇_{AAA} . In other words, if the foreground rejection/suppression for the ideal Airy beam is about twelve orders of magnitude (ratio between the peak and the $k_{\parallel} \sim 1 h \text{ Mpc}^{-1}$ value), such rejection is reduced to only five or even two orders of magnitude in the presence of perturbed beams. This result is in qualitative agreement with previous works that showed that the effects of non-ideal primary beams are to leak foreground power into the EoR window (Bhatnagar. et al., 2008; Parsons et al., 2012; Pober et al., 2013; Ewall-Wice et al., 2017).

Results for the model where sources are distributed across the whole primary beam are rather different. Closure spectra are very similar for all the three different beam models, indicating that

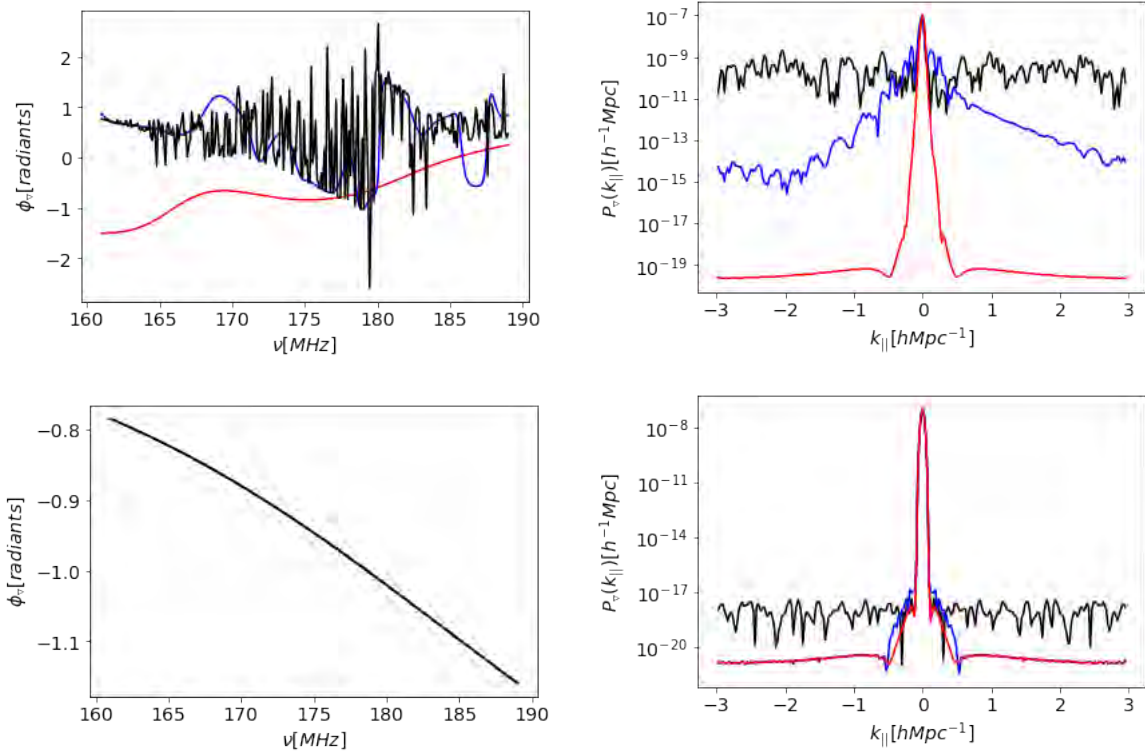


Figure 5.6: Top panels: Simulated closure spectra (left) and power spectra of the bispectrum phase (right) of sky models with sources only across sidelobes (sky model shown on the top right panel of Fig 5.4) for triads that include the Airy beam pattern (red), the perturbed beams E'_L (blue) and E'_H (black) respectively. Bottom panels: same as top but for a sky model with sources distributed across the whole sky patch (sky model shown on the bottom panel of Fig 5.4).

they are mostly dominated by in-beam sources where all the beams have a similar frequency dependence. This is reflected in power spectra too, where the power spectrum from triad ∇_{LLL} is essentially similar to the one from the Airy beam. The power spectrum for triad ∇_{HHH} still shows deviation at $|k_{\parallel}| > 0.5 h \text{ Mpc}^{-1}$, although the foreground rejection remains at the level of approximately ten orders of magnitude. In other words, the presence of in-beam sources makes the contribution from sidelobe sources fairly negligible, leading to a small leakage of power in the EoR window.

Lastly, we study the impact of increased sidelobe level on the closure spectra and power

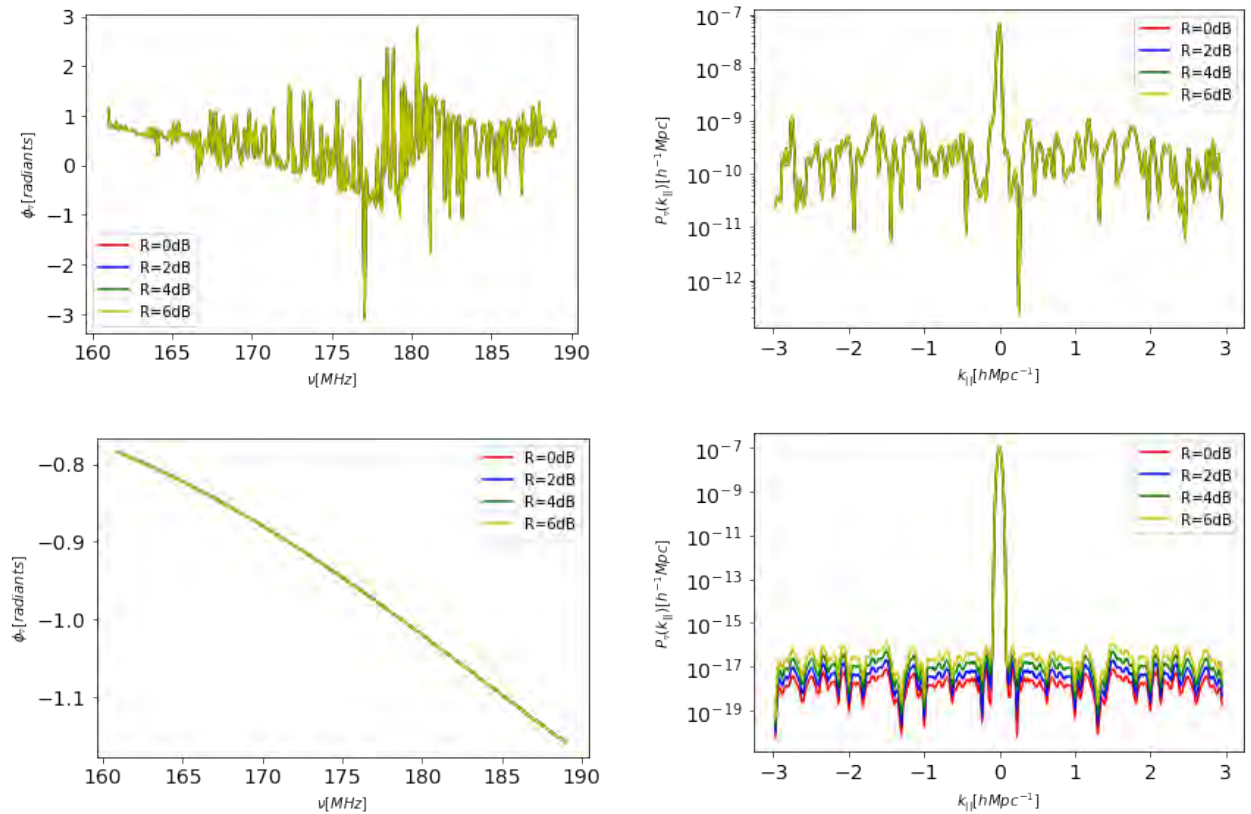


Figure 5.7: Top panels: Simulated closure spectra (left) and power spectra of the bi-spectrum phase (right) of sky models with sources only on sidelobes (see Fig 5.4) for triads that include the Airy beam pattern (red), the perturbed beams $E_{2\text{dB}}$ (blue), $E_{4\text{dB}}$ (green) and $E_{6\text{dB}}$ (yellow) respectively. Bottom panels: same as top but for a sky model with sources distributed across the whole sky patch (Fig 5.4).

Beam model	relative [dB] increase (R)
$E_{0\text{dB}}$	0
$E_{2\text{dB}}$	2
$E_{4\text{dB}}$	4
$E_{6\text{dB}}$	6

Table 5.1: Relative dB gain of four simulated beam models (see equation 5.11).

spectra. We simulate four primary beam models by increasing the E'_H sidelobe amplitude level (Table 5.1). Each beam model E_i was obtained as:

$$10 \log |E_i(\theta_s, \phi_s)|^2 = R + 10 \log |E'_H(\theta_s, \phi_s)|^2, \quad (5.11)$$

where $i = 0, 2, 4, 6$ dB denotes simulated beam models, θ_s and ϕ_s are coordinates of sources located on sidelobes (top right panel of Fig 5.4). $R = [0, 2, 4, 6]$ are the corresponding sidelobe dB level increase relative to E'_H . We apply the perturbed beams E_i to the sky models shown in Fig 5.4, with sources on the main and sidelobes of the beam (top left panel) and a sky model with sources only on the sidelobes (bottom left). Figure 5.7 shows the corresponding closure and power spectra.

We first consider the sky model with sources outside the beam main lobe. The closure spectra from all simulated beams are largely the same, with only small differences and, as a consequence, the corresponding power spectra also show similar features with variations much smaller than $\sim 10^{-10} h^{-1} \text{ Mpc}$ at $|k_{\parallel}| > 0.5 h \text{ Mpc}^{-1}$ than the typical power spectrum leakage level (see Fig 5.6 and 5.7). This is also true for the sky model with sources both within the main beam and across sidelobes. Differences in the power spectra are of the order of $\sim 10^{-17} h^{-1} \text{ Mpc}$. Thus the increase of sidelobe level, up to 6 dB, has negligible impact on the closure and power spectra. In summary, the largest contribution to foreground power leakage into the EoR window are sidelobe ripples of the primary beam.

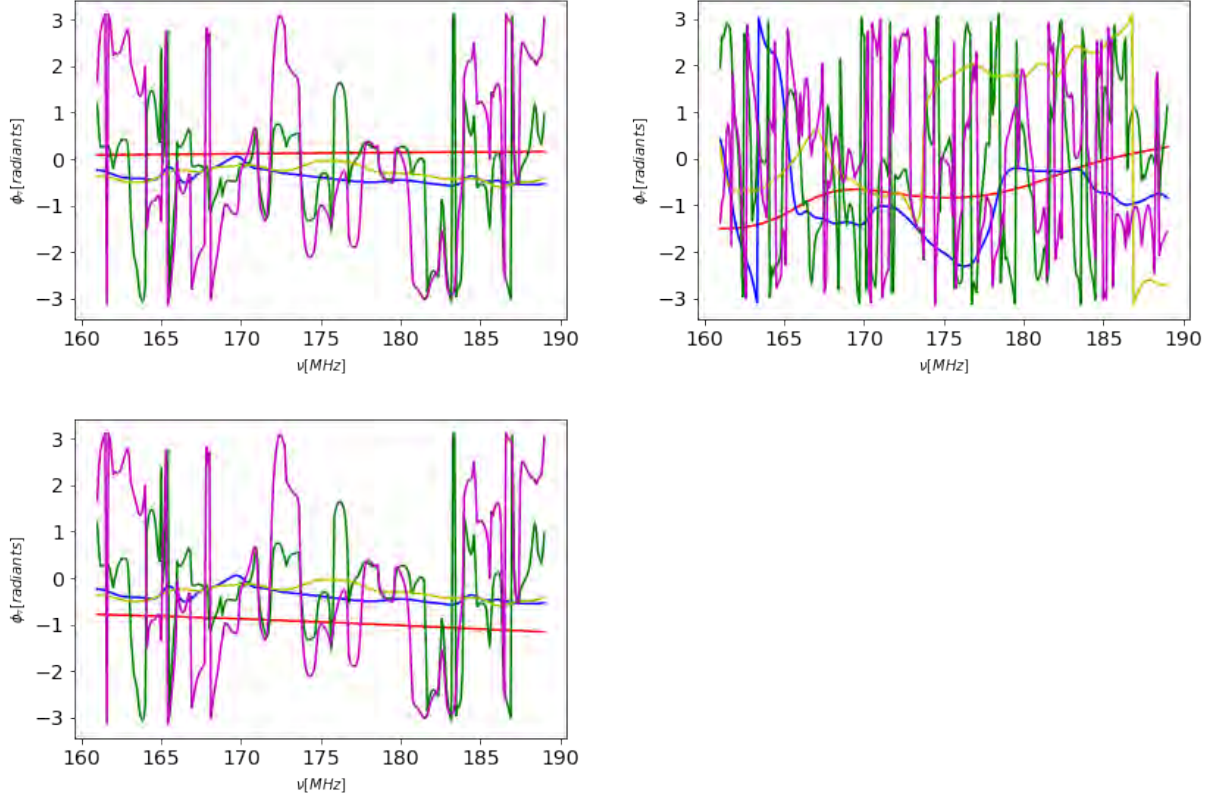
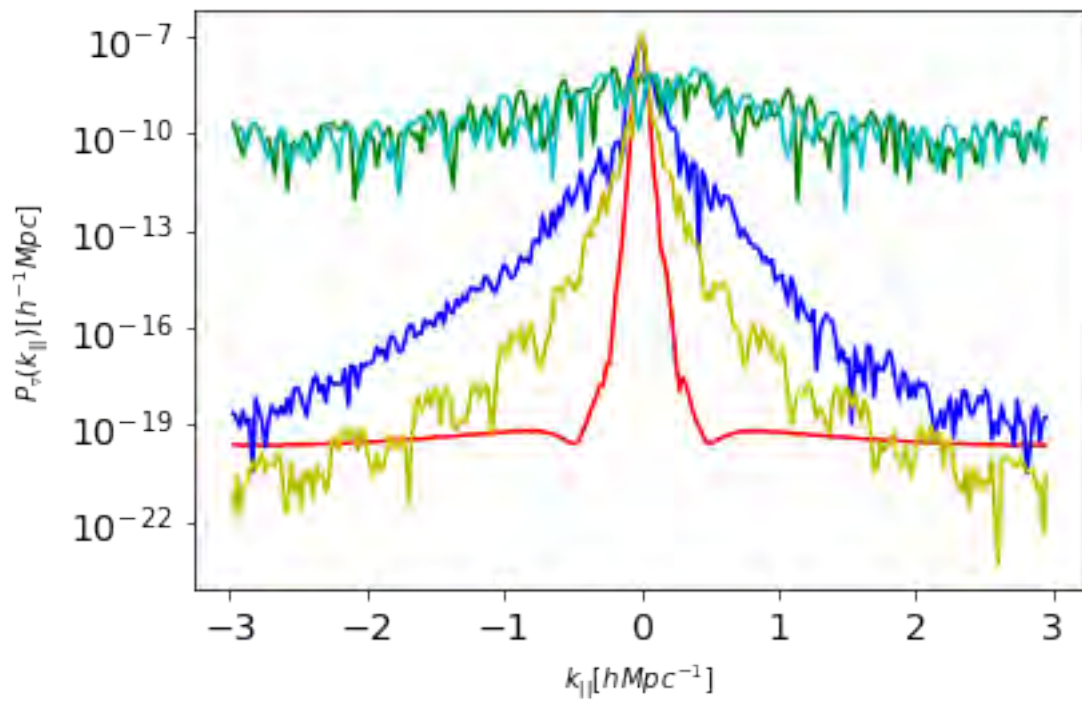
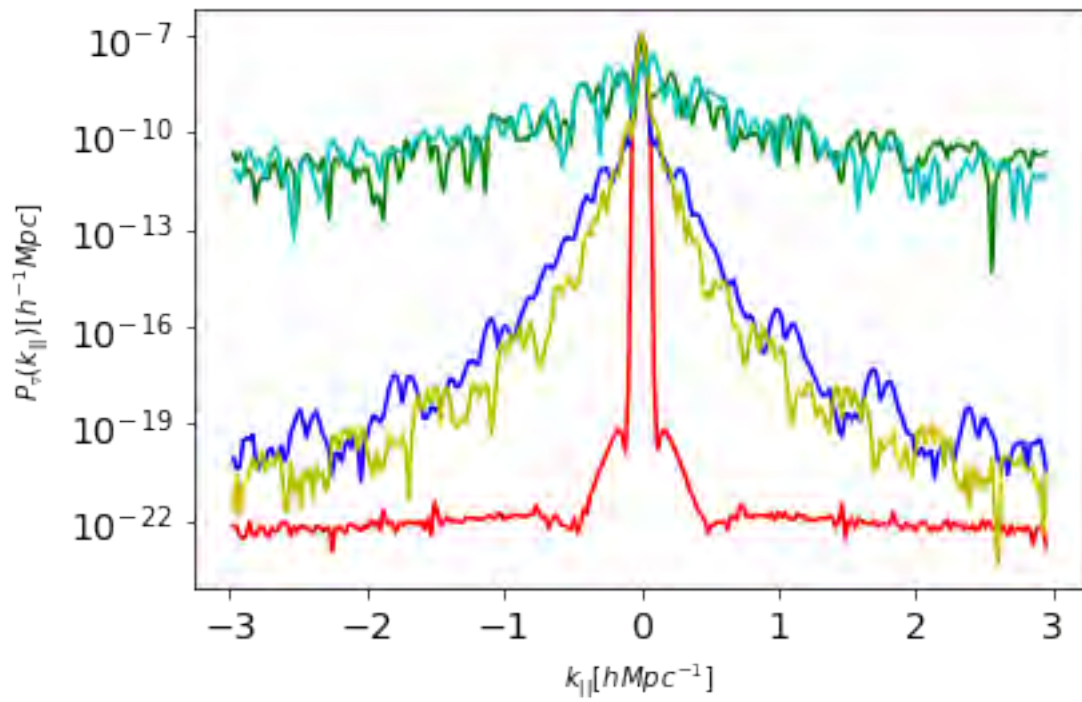


Figure 5.8: Simulated closure spectra corresponding to sky models shown in Fig 5.4: ∇_{AAA} (red), ∇_{CCC} (blue), ∇_{EEE} (yellow), ∇_{CEE} (green) and ∇_{ECC} (cyan).

5.2 Power spectrum simulations with mutual coupling beams

In this section, we use primary beam patterns with mutual coupling generated by [Fagnoni et al. \(2019\)](#). We use beams from dishes 22 and 26 (Fig 5.1) and simulate the effect of mutual coupling of an antenna placed at the centre of the array and one at the edge, respectively. Hereon we denote primary beam from dish 22, 26 and the Airy power pattern as E_C , E_E and E_A respectively. We simulate observations for a single polarisation, i.e. the Y polarisation.

We combine different primary beams to simulate five types of 14 m equilateral triads: (1) a triad at the centre of the array, with antenna primary beams E_C (∇_{CCC}); (2) one at the edge of the array with one primary beams E_C and two E_E (∇_{CEE}); (3) a second triad at the edge with two primary beams E_C and one E_E (∇_{ECC}); (4) a hypothetical isolated triad with only edge



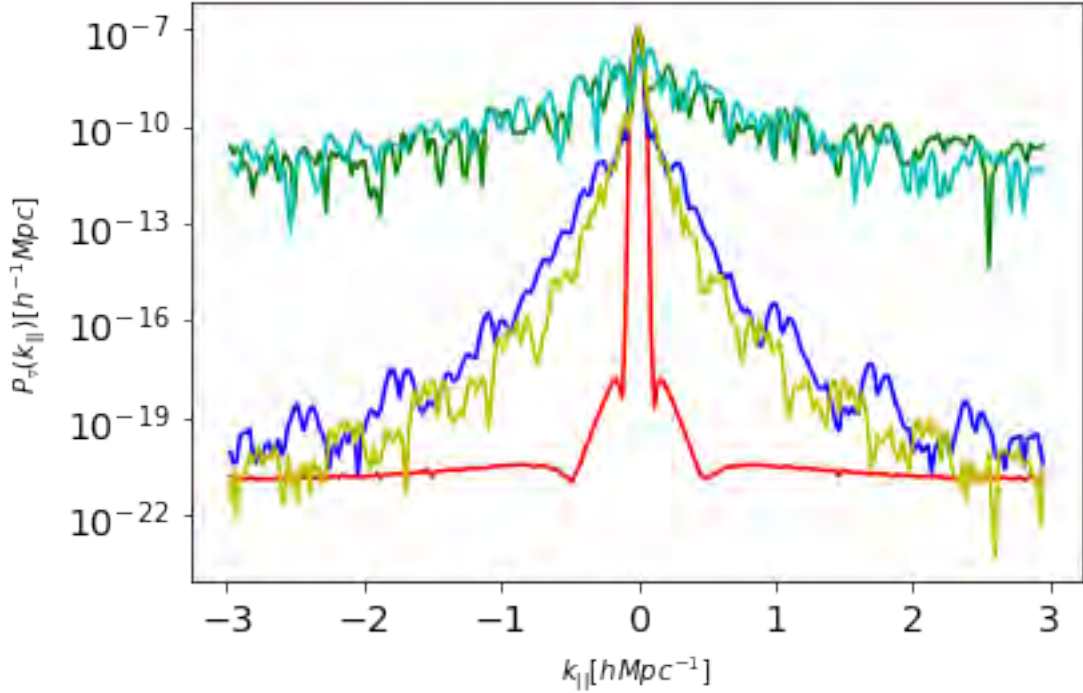


Figure 5.9: Simulated power spectra of the bispectrum phase corresponding to sky models shown in Fig 5.4. Top panel (Top right panel in Fig 5.4), center panel: (Top left panel in Fig 5.4) and bottom panel (bottom panel in Fig 5.4). Colours denote power spectrum from simulated triads; $P_{\nabla AAA}$ (red), $P_{\nabla CCC}$ (blue), $P_{\nabla EEE}$ (yellow), $P_{\nabla CEE}$ (green) and $P_{\Delta ECC}$ (cyan).

beams E_E (∇_{EEE}) and (5) a triad unaffected by mutual coupling with Airy-type primary beams E_A (∇_{AAA}). We study the impact of mutual coupling on the three sky models shown in Fig 5.4. We use equation 3.17 to simulate visibilities with primary beam effects.

Figure 5.8 and 5.9 show the corresponding power spectra and closure spectra, respectively. We first consider the sky model with sources within the main lobe. As the beam main lobe in triads ∇_{CCC} and ∇_{EEE} varies with frequency (Fig 5.10), closure spectra show pronounced frequency structure, leading to foreground power leakage. The leakage is more severe for triads with different primary beams, i.e. ∇_{ECC} (cyan) and ∇_{CEE} (green), as the phase information of the beam does not cancel out. The complex phase of mutual coupling beams has a very pronounced frequency structure, as can be seen in Fig 5.10. This inevitably leads to a pronounced

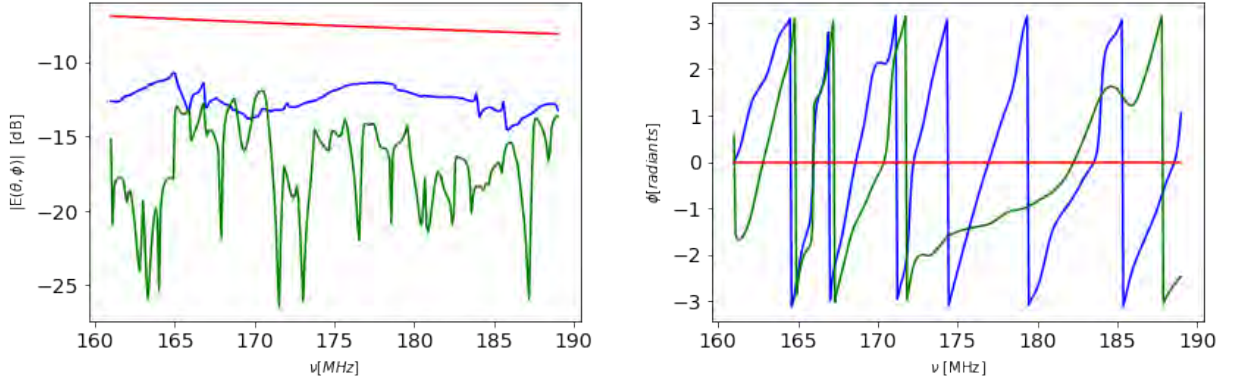


Figure 5.10: Left: beam response [dB] averaged across all source locations for the sky model with sources only in the main lobe (top left panel of Fig 5.4) as a function of frequency. Right: beam phase at zenith as a function of frequency for E_E (green), E_C (blue) and E_A (red).

frequency structure in the closure spectra, causing even greater leakage power, up to 12 orders of magnitude higher than the power from the ∇_{AAA} triad at $|k_{\parallel}| > 0.5 h \text{ Mpc}^{-1}$.

The same general behaviour of the closure spectra and power spectra is found for other sky models. However, it is worth noting that the leakage is much more severe at $|k_{\parallel}| \sim 1.5 h \text{ Mpc}^{-1}$, up to ~ 5 orders magnitude higher when there are no sources on the main lobe. We also note that models which have sources within the main lobe have nearly identical power spectra, as those sources are the main contribution to the closure spectra.

Power spectra from triad ∇_{CCC} results in the worst overall leakage compared to ∇_{EEE} , i.e. the blue line is at above the yellow line for most k_{\parallel} modes (Fig 5.9), and the difference in the leakage level is of the order of $\sim 10^{-16} h^{-1} \text{ Mpc}$, most prominent when there are no sources in the main lobe. We speculate that this may be the result of the E_E beam having fewer ripples on the side less affected by mutual coupling, resulting in a relatively smooth spectral response compared to the E_C beam which has ripples on either side of the beam (see Fig 5.3).

In our discussion so far, we always have restricted our power spectrum analysis to one field at a time; that is, each of our plots thus far only compares/shows power spectra from the same field. We now consider comparing power spectra from different sky models or fields. To do this, we need to express the power spectrum in absolute units. Consequently, this also allows

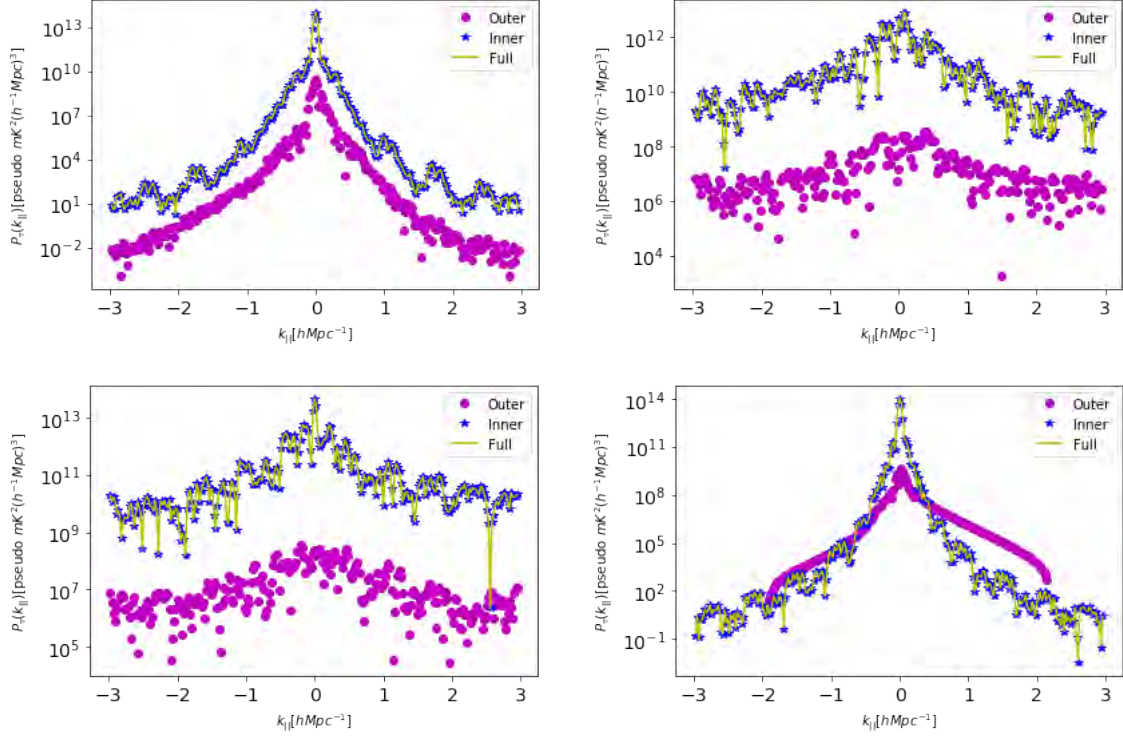


Figure 5.11: Simulated power spectrum from triads ∇_{CEE} (top left panel), ∇_{CCC} (top right panel), ∇_{ECC} (bottom left panel) and ∇_{EEE} (bottom right panel) of sky models shown in figure 5.4. Colours denote the sky model; blue (top right panel in Fig 5.4), magenta (top left panel in Fig 5.4) and yellow (bottom panel panel in Fig 5.4). The power spectrum from sky model with sources on the main lobe and sidelobes is almost identical to sky model with in-beam sources, consequently the yellow line is on top of the blue line.

us to quantify the level of leakage in absolute units, rather than to use a relative comparison power to the power spectrum of triad ∇_{AAA} . The power spectrum of the bispectrum phase can be expressed in units of $\text{mK}^2 (h^{-1} \text{Mpc})^3$ as (Thyagarajan & Carilli, 2020):

$$P_{\nabla}(k_{||}) = |\tilde{\Psi}_{\nabla}|^2 \left(\frac{\lambda^2}{2k_B} \right)^2 \left(\frac{D_c^2 \Delta D_c}{B_{eff}} \right) \left(\frac{1}{\Omega B_{eff}} \right), \quad (5.12)$$

where

$$\tilde{\Psi}_{\nabla} = \tilde{W}(\tau) * \tilde{\Xi}_{\nabla}(\tau) * V_{eff} * \delta(\tau), \quad (5.13)$$

and \tilde{W} and $\tilde{\Xi}_{\nabla}$ are delay transforms of window function W and complex closure phase Ξ_{∇}

respectively, $\delta(\tau)$ is the Dirac delta function centered delay $\tau = 0$ and V_{eff} :

$$(V_{eff})^{-2} = \sum_{p=1}^3 |V_p|^{-2}, \quad (5.14)$$

where

$$V_p = \frac{\int W(\nu) V_p'(\nu) d\nu}{\int W(\nu) d\nu}, \quad (5.15)$$

and p denotes the baseline index in a triad. V_p is a normalisation factor. The closure spectrum is a dimensionless quantity, and therefore contains no information on the relative brightness of different fields. The normalisation factor accounts for the relative brightness of different fields by scaling each individual power spectrum. We expect a bright field to have high power spectrum compared to a cold field.

Figure 5.11 shows the power spectrum in $\text{mK}^2 (h^{-1} \text{Mpc})^3$ units of simulated sky models (Fig 5.4) for all the triads with mutual coupling. The sky model with sources only across sidelobes shows the worse leakage (see Fig 5.9). However, its power spectrum has relatively low power in absolute units (Fig 5.11), up to ~ 2 orders of magnitude below the power spectrum from sky models with in-beam sources, at all k_{\parallel} modes, except for ∇_{CCC} , whereas the power spectrum from the model with sources only on the sidelobe has higher power at $|k_{\parallel}| > 0.1h \text{Mpc}^{-1}$. The power spectrum of the ∇_{CCC} triad further demonstrates that the unsmooth spectral response of the E_C sidelobes causes leakage of power from low k_{\parallel} modes, i.e. $|k_{\parallel}| < 0.5h \text{Mpc}^{-1}$ to high k_{\parallel} modes.

5.3 Power spectrum simulations with realistic foregrounds and mutual coupling beams

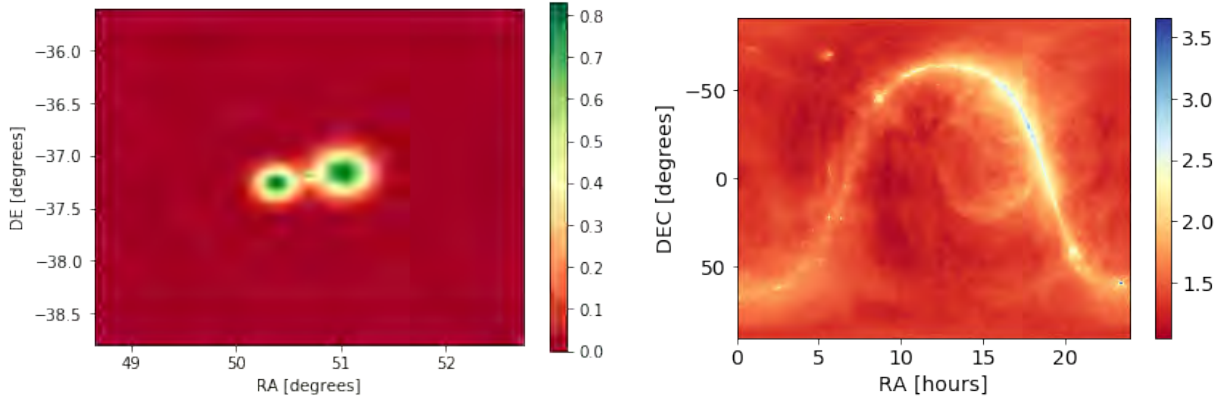


Figure 5.12: Left: Image of Fornax A at $\nu = 150$ MHz (Jy/pixel units). The model is based on observations by [McKinley et al. \(2015\)](#). Right: Galactic diffuse emission at $\nu = 408$ MHz ([Remazeilles et al., 2015](#)). The colour scale is in $\log_{10} T[\text{K}]$ units.

We conclude by simulating a realistic sky model and incorporate the effect of mutual coupling. We simulate three different pointings centred at LST = $3^{\text{h}} 44^{\text{m}} 6.7^{\text{s}}$, $6^{\text{h}} 0^{\text{m}} 6.7^{\text{s}}$ and $8^{\text{h}} 0^{\text{m}} 6.7^{\text{s}}$ that we name GLEAM 1, GLEAM 2 and GLEAM 2 respectively. We extract sources from the GLEAM catalogue brighter than 200 mJy at 151 MHz within a $110^{\circ} \times 70^{\circ}$ region and centre on each LST.

All sources are treated as point sources even if they may be resolved at the GLEAM resolution. This approximation is, however, valid given the very short baselines considered (14 m equilateral triad). The total number of sources selected are between 20 000 and 30 000 for the three pointings.

The GLEAM catalogue excludes bright sources like Fornax A. We include a model of Fornax A based on observations by [McKinley et al. \(2015\)](#), where the core and the two lobes are described by Gaussian components. The West lobe is modelled with a circular Gaussian that has a $20'$ axis and a spectral index $\alpha = 0.77$. The East lobe is modelled with a circular Gaussian that has a $15'$ and a spectral index of $\alpha = 0.77$. The core lobe is modelled with a circular Gaussian that has a $5'$ axis and a spectral index of $\alpha = 1$. From the model image cube (Fig 5.12), we treat each pixel of the image as a point source and use equation 3.17 to simulate Fornax A visibilities. Fornax A is included in GLEAM 1 and GLEAM 2 pointings but not in the GLEAM 3 pointing

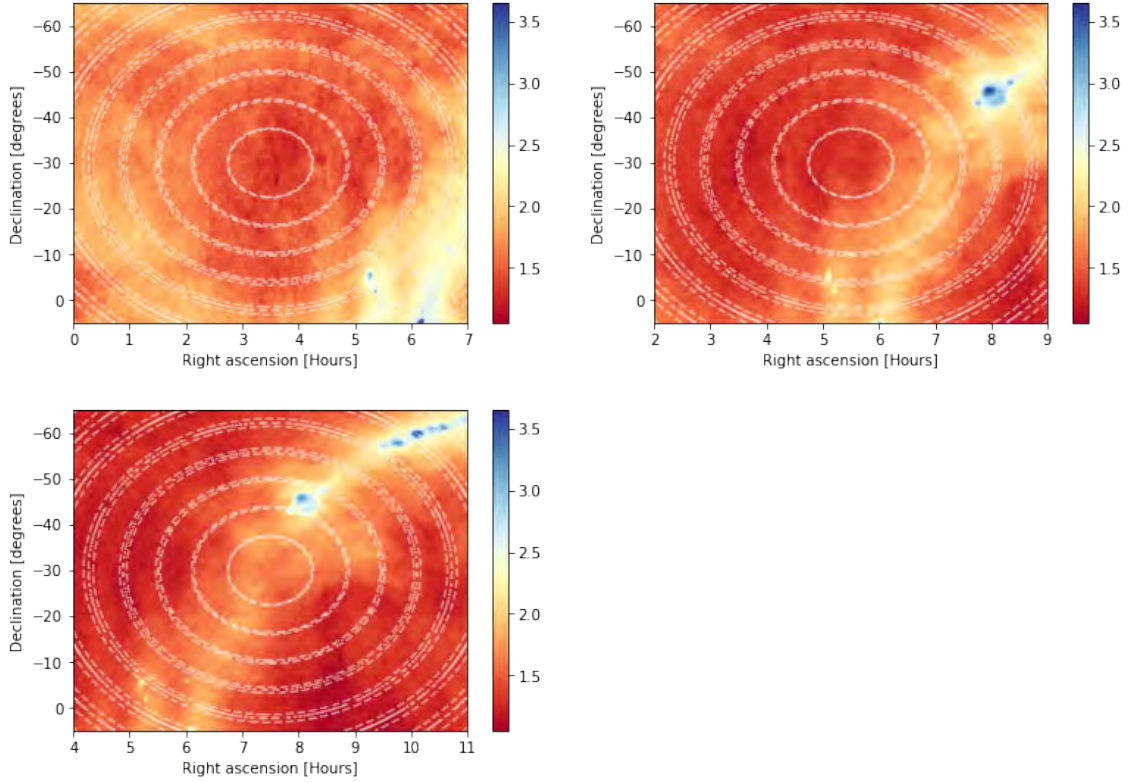


Figure 5.13: Panels show simulated Galactic diffuse emission GLEAM 1 (top left), GLEAM 2 (top right) and GLEAM 3 (bottom). White contours shows nulls of the Airy power pattern. The scale of the colour bar is $\log_{10} T[\text{K}]$

as it is outside the field of view.

We also include Galactic diffuse emission from the 408 MHz Haslam map reprocessed by [Remazeilles et al. \(2015\)](#). The map is in the Healpix coordinate system ([Zonca et al., 2019](#)), and we transform it into the celestial coordinate system by mapping each pixel to the corresponding α and δ . As a result, our transformed map (Fig 5.12) has the same resolution. We extrapolate the map to 150 MHz, using a spectral index $\alpha = 0.7$. We again treat each pixel as a point source and simulate visibilities of the Galactic diffuse emission using equation 3.17. Figure 5.13 shows the diffuse emission with respect to the pointing direction. We again simulate noiseless visibilities for a 14 m equilateral triad, centred at 175 MHz ($z = 7.1$) with a $B = 30.77$ MHz, corresponding to an effective bandwidth $B_{eff} = 9.77$ MHz. The channel width is $df = 97.66$ kHz.

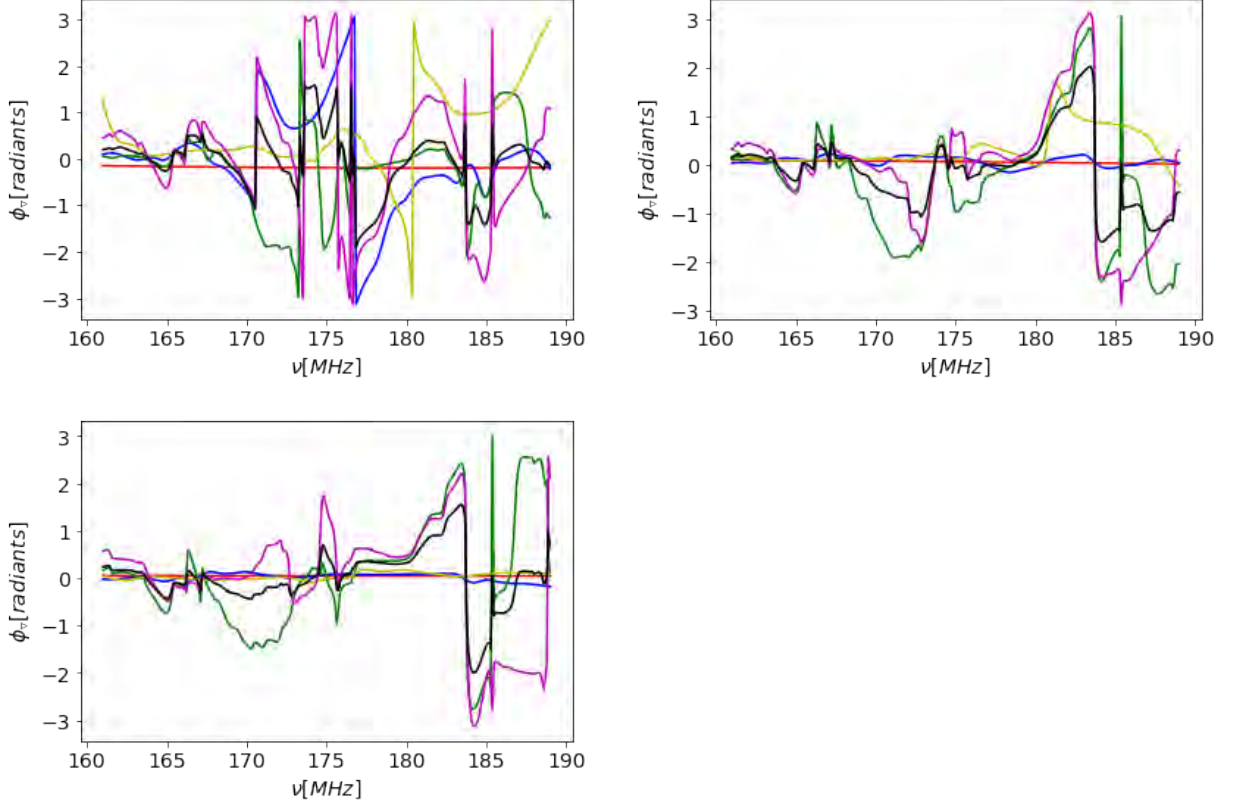
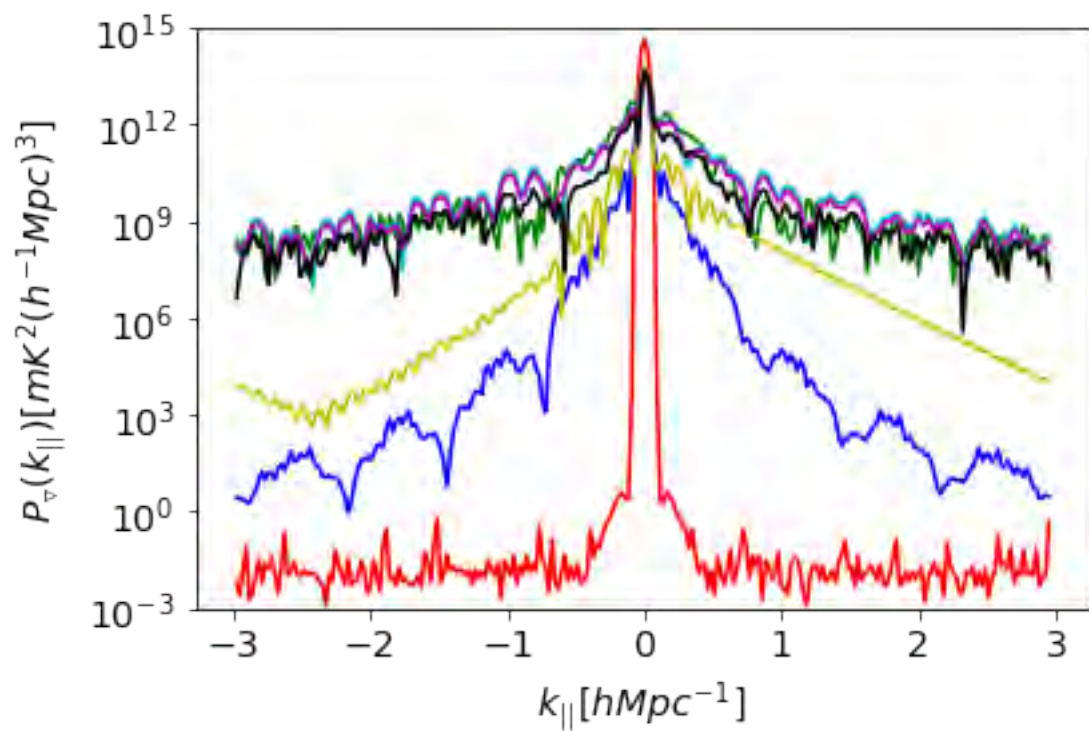
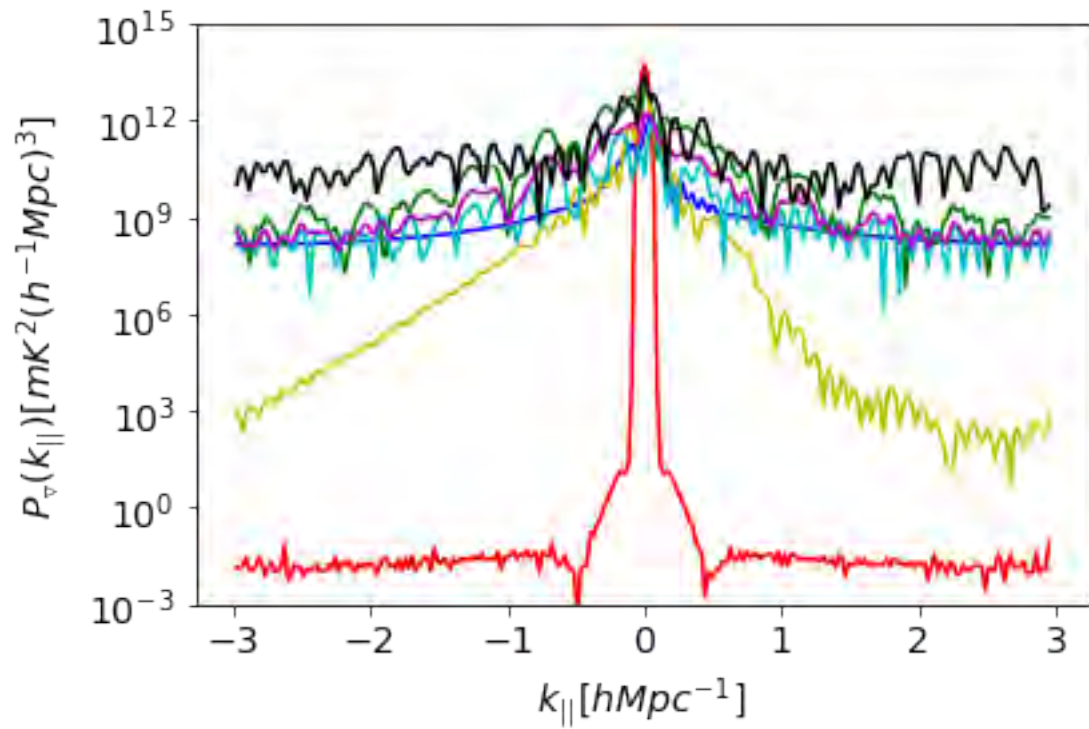


Figure 5.14: Simulated closure spectra corresponding to sky models GLEAM 1 (top left), GLEAM 2 (top right) and GLEAM 3 (bottom). The colours indicate the closure spectrum from different simulated triads: ∇_{AAA} (red), ∇_{CCC} (blue), ∇_{EEE} (yellow), ∇_{CEE} (green) and ∇_{ECC} (cyan). Black shows the average closure spectra from simulated triads ∇_{CCC} , ∇_{ECC} , ∇_{CEE} and ∇_{EEE} .

Figure 5.14 and 5.15 show the corresponding power spectra and the closure spectra, respectively. The magnitude of the leakage is severe for the GLEAM 1 pointing particularly for triad ∇_{CCC} , ∇_{ECC} and ∇_{CEE} at $|k_{\parallel}| > 0.5 h \text{ Mpc}^{-1}$. The power spectrum is ~ 10 orders of magnitude brighter than the power spectrum from the ∇_{AAA} triad. The rejection ratio at $|k_{\parallel}| \sim 1$ is only ~ 6 , with a leakage level that can compromise the detection of the 21 cm signal which is expected to be ~ 8 orders of magnitude below the $k_{\parallel} = 0$ mode (Thyagarajan et al., 2018). Indeed we expect such results for triads ∇_{ECC} and ∇_{CEE} , given their spectral properties demonstrated in the previous section. However, it is worth noting that, despite the fact that E_C beam phase is



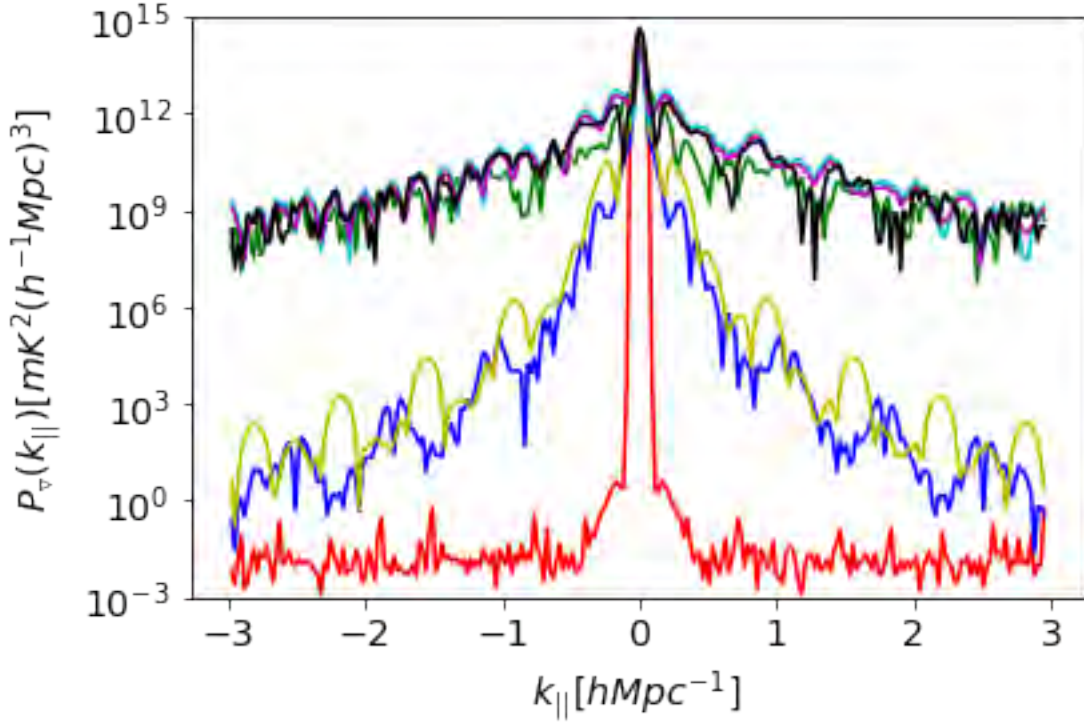


Figure 5.15: Simulated power spectra corresponding to sky models GLEAM 1 (top), GLEAM 2 (top middle) and GLEAM 3 (bottom). The colours indicate the powers spectrum from different simulated triads: ∇_{AAA} (red), ∇_{CCC} (blue), ∇_{EEE} (yellow), ∇_{CEE} (green) and ∇_{ECC} (cyan). Black shows the power spectrum of average closure spectra from simulated triads ∇_{CCC} , ∇_{ECC} , ∇_{CEE} and ∇_{EEE} , magenta shows the weighted averaged power spectrum (see equation 5.16).

cancelled out in triad ∇_{CCC} , the triad has a leakage level close to triads ∇_{ECC} and ∇_{CEE} . The power spectrum of the bispectrum phase from triad ∇_{EEE} is ~ 4 orders below the ∇_{CCC} triad at $|k_{\parallel}| > 2 h \text{ Mpc}^{-1}$. These results indeed, demonstrate again that the frequency structure of the E_C beam is much more pronounced than the E_E beam.

Moving to pointing GLEAM 2, we can see that power spectra from triads ∇_{CEE} and ∇_{ECC} are at the same level as the GLEAM 1 pointing, $\sim 10^9 \text{ mK}^3 (h^{-1} \text{ Mpc}^3)$. However, the power spectrum from ∇_{CCC} has dropped by $\sim [6 - 8]$ orders of magnitude at $|k_{\parallel}| > 2 h \text{ Mpc}^{-1}$, ~ 1 order of magnitude below the power spectrum from triad ∇_{EEE} . The explanation for this lies in the brightness distribution of the Galactic emission across the beam, which is the brightest com-

ponent in our sky models. Figure 5.13 shows that the brightest region of the Galactic emission is located beyond the third sidelobe, and the emission in the main lobe is ~ 2 orders of magnitude colder. Hence, in this field the contribution of the bright region in the sidelobes is significant, and the closure spectra shows consequently, a pronounced frequency structure (top right panel of Fig 5.14), and thus leads to overall higher power leakage. This is in contrast with the GLEAM 2, which has a strip of bright emission along the first and second sidelobe, which are spectrally smooth compared to sidelobes beyond the third sidelobe and hence, the resulting closure spectra is relatively smooth, and thus leads to relatively less power leakage (Fig 5.15).

We finally consider the GLEAM 3 pointing. Power spectra from triads ∇_{CEE} and ∇_{ECC} is at same level as the GLEAM 1 pointing, at $\sim 10^9 \text{ mK}^3 (h^{-1} \text{ Mpc}^3)$. However, similarly to the GLEAM 2 pointing, the power spectrum from ∇_{CCC} and ∇_{EEE} , has significantly less leakage compared to GLEAM 1, up to ~ 8 orders of magnitude lower at $|k_{\parallel}| > 2 h \text{ Mpc}^{-1}$. Interestingly, the leakage level at $|k_{\parallel}| \sim 1 h \text{ Mpc}^{-1}$ of the power spectrum from ∇_{CCC} in GLEAM 3 is now ~ 1 order below that of GLEAM 2. Similarly, the power spectrum of triad ∇_{EEE} has dropped by ~ 2 orders of magnitude at $|k_{\parallel}| \sim 1 h \text{ Mpc}^{-1}$. This is a consequence of the bright strip Galactic emission crossing the main lobe of the beam (see bottom panel of Fig 5.13), and thus suppressing the contribution to the closure spectra of any bright region in the sidelobes. This results in relatively smooth closure spectra, and thus less power leakage is observed.

So far, we have calculated and analysed power spectra from a single triad. However, with real observations, the power spectra from different triads are normally averaged together in order to increase the Signal to Noise Ratio (SNR). We explore two ways of averaging the data. We first consider the case that ideal redundancy is assumed, and therefore the closure spectra from redundant triads are averaged together before computing the power spectrum (coherent average). Second, we average the power spectra from different triads (incoherent average).

We evaluate the average power spectrum by first averaging closure spectra from triads with mutual coupling beams, i.e. ∇_{ECC} , ∇_{CEE} and ∇_{CCC} and then compute the power spectrum of the bispectrum phase from the average closure spectrum. Alternatively, we compute a weighted average of the power spectra from triads with mutual coupling where the weight is given by the

number of triads in the array configuration:

$$\bar{P} = \frac{10P_{\nabla_{ECC}} + 3P_{\nabla_{CCC}} + 2P_{\nabla_{CEE}}}{15}, \quad (5.16)$$

where the $P_{\nabla_{ECC}}$, $P_{\nabla_{CCC}}$ and $P_{\nabla_{CEE}}$ are the power spectra from triads ∇_{ECC} , ∇_{CCC} and ∇_{CEE} respectively. The numbers 10, 3 and 2 express the relative ratio of north facing 14 m equilateral triads - e.g. [0,1,12] - (see Fig 2.7) of type ∇_{ECC} , ∇_{CCC} and ∇_{CEE} , respectively.

Figure 5.14 and 5.15 and show the corresponding closure spectra and average power spectrum, respectively. The average closure spectra has a pronounced frequency structure, due to the frequency structure of closure spectra from triads ∇_{ECC} and ∇_{CEE} , and their average leads to closure spectra that also varies rapidly with frequency. As a result, the power spectrum of the average closure spectra is similar to power spectrum from triads ∇_{ECC} and ∇_{CEE} for GLEAM 2 and 3 pointings, and notably even higher than the GLEAM 1 pointing at $|k_{\parallel}| > 1 h \text{ Mpc}^{-1}$. This supports evidence that assuming ideal redundancy may worsen the overall leakage level.

The incoherently average power spectrum also has high power at large k_{\parallel} modes, but notably, the power spectrum is approximately one order of magnitude lower than the coherently averaged power spectrum for GLEAM 1 at $|k_{\parallel}| > 2 h \text{ Mpc}^{-1}$. As there are more triads of type ∇_{ECC} , the weighted power spectrum is more similar to the power spectrum of triad ∇_{ECC} . However, with full HERA array (350 antennas) we expect there to be more triads of type ∇_{CCC} , and hence the average power spectrum will be more similar to the power spectrum of ∇_{CCC} , which has significantly has less power at $|k_{\parallel}| > 2 h \text{ Mpc}^{-1}$, for GLEAM 2 and 3 pointings, and therefore the average power spectrum will have less power leakage at $|k_{\parallel}| > 2 h \text{ Mpc}^{-1}$ than currently simulated.

As a last note, these results show that for sky patches with bright sources across beam side-lobes, a coherent average of the closure spectra will lead to greater leakage of power into the EoR window compared to incoherent power spectrum average. The incoherent power spectrum average of different LST bins reduces mutual coupling effects, in that, fields of type GLEAM 1 and 3 will be observed, and thus the leakage level of the average power spectrum at high k_{\parallel} will reduce since power spectrum from fields of type GLEAM 1 have significantly less leakage level.

CHAPTER 6

Conclusions

Observations of the 21 cm signal from the Epoch of Reionization are challenged by the presence of bright foreground emission that requires an extremely accurate separation. In turn, this separation can only occur if interferometric calibration is very precise (e.g., [Bernardi, 2019](#)): calibration errors are limiting current 21 cm observations (e.g., [Eastwood et al., 2019](#); [Kolopanis et al., 2019](#); [Trott et al., 2020](#); [Mertens et al., 2020](#); [Gehlot et al., 2020](#)).

The use of closure quantities has recently been proposed in the literature as an alternative way to detect the 21 cm signal ([Thyagarajan et al., 2018](#); [Carilli et al., 2018](#)) as they are, to first order, insensitive to calibration errors. They are, however, affected by, for example, errors that arise from antennas that are different from each other.

In this thesis, I investigated the effect that antennas with different primary beams have on foreground closure spectra and, ultimately, on the power spectrum of the bispectrum phase - the metric used to detect the 21 cm signal ([Thyagarajan et al., 2018, 2020](#)). In particular, I intend to quantify how much foreground avoidance is affected by the presence of mutual coupling beams, i.e. how much foreground power is spread into the EoR window.

I developed a pipeline to simulate foreground closure spectra as observed by the HERA triads

that are more numerous in its highly redundant configuration, i.e. the 14 m and 29 m triads. I first validated our pipeline by simulating closure spectra of simple sky models and primary beam patterns. I also simulated calibration errors in order to reproduce the well-known result that they do not impact closure spectra. I found that structure in closure spectra is mainly due to the presence of sources across side lobes of the primary beam, as they have a strong frequency dependence. This result is in qualitative agreement with the analysis of HERA data by [Carilli et al. \(2018\)](#).

I eventually used realistic HERA beams simulated by [Fagnoni et al. \(2019\)](#) that include mutual coupling effects that arise from the closely packed array configuration. Mutual coupling beams have more pronounced side lobes and a more rapidly frequency variation compared to the unperturbed beams. I first model the mutual coupling beams via Gaussian Processes in order to gain an intuitive understanding of the mutual coupling effects and, eventually, I simulated observations with the actual mutual coupling beams. These simulations included point sources and diffuse Galactic synchrotron emission for three HERA pointing centred at LST = $3^{\text{h}} 44^{\text{m}} 6.7^{\text{s}}$, $6^{\text{h}} 0^{\text{m}} 6.7^{\text{s}}$ and $8^{\text{h}} 0^{\text{m}} 6.7^{\text{s}}$.

I found that mutual coupling beams lead to foreground closure spectra that have significantly more frequency structures than the case with unperturbed beams. In turn, the foreground leakage into the EoR window is ~ 8 orders magnitude higher than the case of an ideal (Airy pattern) beam at $k_{\parallel} > 0.5 h \text{ Mpc}^{-1}$. The foreground leakage is worse when edge antennas are included, i.e. when the antenna beams not only suffer from mutual coupling, but triads include antennas whose beams are different from each other. In this case, the power leakage is as high as ~ 12 orders of magnitude compared to unperturbed beams. In this case, the rejection ratio at $|k_{\parallel}| \sim 1$ is only ~ 6 . The isolation of the 21 cm signal from foregrounds at redshift $z = 7.1$ can only be done at $|k_{\parallel}| > 0.5 h \text{ Mpc}^{-1}$ and one needs a rejection ratio of at least ~ 8 orders of magnitude ([Thyagarajan et al., 2018](#)). Hence, the leakage level could have dire consequences on the measurements, if not addressed.

In this thesis, we have therefore demonstrated and quantified the hypothesis that beams affected by mutual coupling have a severe impact on foreground closure spectra. However, more investigation is needed in order to conclude whether or not they may represent a showstopper for

the detection of the 21 cm signal. Our simulations also provide a useful framework to interpret observations and assess which power spectrum region is expected to be most contaminated by foreground power leakage.

Bibliography

- Ali, Z. S., Parsons, A. R., Zheng, H., et al. 2015, *The Astrophysical Journal*, 809, 61
- Barkana, R., & Loeb, A. 2007, *Reports on Progress in Physics*, 70, 627
- Barry, N., Hazelton, B., Sullivan, I., Morales, M. F., & Pober, J. C. 2016, *Monthly Notices of the Royal Astronomical Society*, 461, 3135–3144
- Barry, N., Wilensky, M., Trott, C. M., et al. 2019, *The Astrophysical Journal*, 884, 1
- Bennett, C. L., Larson, D., Weiland, J. L., et al. 2013, *The Astrophysical Journal Supplement Series*, 208, 20
- Bennett, J. O. 2007, *The essential cosmic perspective*, 4th edn. (San Francisco ; London : Addison Wesley), "The kit contains instructions and a code for you to access this dynamic website"—Cover, p. 3
- Bernardi, de Bruyn, A. G., Brentjens, M. A., et al. 2009, *A&A*, 500, 965
- Bernardi, G. 2019, arXiv e-prints, arXiv:1909.11938
- Bernardi, G., McQuinn, M., & Greenhill, L. J. 2015, *The Astrophysical Journal*, 799, 90

- Bernardi, G., de Bruyn, A. G., Harker, G., et al. 2010, *aap*, 522, A67
- Beuermann, K., Kanbach, G., & Berkhuijsen, E. 1985, *Astronomy and Astrophysics*, 153, 17
- Bhatnagar, S., Cornwell, T. J., Golap, K., & Uson, J. M. 2008, *A&A*, 487, 419
- Bowman, J. D., Morales, M. F., & Hewitt, J. N. 2009, *The Astrophysical Journal*, 695, 183
- Bowman, J. D., Rogers, A. E. E., Monsalve, R. A., Mozdzen, T. J., & Mahesh, N. 2018, *Nature*, 555, 67–70
- Brandenburg, A., & Subramanian, K. 2007, *Astronomische Nachrichten*, 328, 507
- Bruyn, G. d. 2008, *Lecture notes in Radio astronomy, interferometry and aperture synthesis*
- Buras, A. J., Ellis, J., Gaillard, M. K., & Nanopoulos, D. V. 1978, *Nuclear Physics B*, 135, 66
- Callingham, J. R., Ekers, R. D., Gaensler, B. M., et al. 2017, *The Astrophysical Journal*, 836, 174
- Carilli, C. L., Nikolic, B., Thyagarayan, N., & Gale-Sides, K. 2018, *Radio Science*, 53, 845
- Chapman, E., Zaroubi, S., Abdalla, F., et al. 2014, *The Effect of Foreground Mitigation Strategy on EoR Window Recovery*, arXiv:1408.4695
- Cohen, A., Fialkov, A., Barkana, R., & Lotem, M. 2017, *Monthly Notices of the Royal Astronomical Society*, 472, 1915
- Craeye, C., & González-Ovejero, D. 2011, *Radio Science*, 46, <https://agupubs.onlinelibrary.wiley.com/doi/pdf/10.1029/2010RS004518>
- De Breuck, C., Röttgering, H., Miley, G., van Breugel, W., & Best, P. 2000, *aap*, 362, 519
- DeBoer, D. R., et al. 2017, *Publ. Astron. Soc. Pac.*, 129, 045001
- Dillon, J. S., Kohn, S. A., Parsons, A. R., et al. 2018, *Monthly Notices of the Royal Astronomical Society*, doi:10.1093/mnras/sty1060

- Eastwood, M. W., Anderson, M. M., Monroe, R. M., et al. 2019, *The Astronomical Journal*, 158, 84
- Ewall-Wice, A., Dillon, J. S., Liu, A., & Hewitt, J. 2017, *Monthly Notices of the Royal Astronomical Society*, 470, 1849
- Fagnoni, N., Acedo, E., DeBoer, D., et al. 2019, Electrical and electromagnetic co-simulations of the HERA Phase I receiver system including the effects of mutual coupling, and impact on the EoR window
- Fialkov, A., & Barkana, R. 2019, *Monthly Notices of the Royal Astronomical Society*, 486, 1763
- Fixsen, D. J. 2009, *The Astrophysical Journal*, 707, 916
- Fuchs, B. 2001, in *Dark Matter in Astro- and Particle Physics*, ed. H. V. Klapdor-Kleingrothaus (Berlin, Heidelberg: Springer Berlin Heidelberg), 25–32
- Fuller, G. M., Mathews, G. J., & Alcock, C. R. 1988, *Phys. Rev. D*, 37, 1380
- Furlanetto, S. R. 2006, *mnras*, 371, 867
- Gehlot, B. K., Mertens, F. G., Koopmans, L. V. E., et al. 2019, *Monthly Notices of the Royal Astronomical Society*, 488, 4271
- Gehlot, B. K., Mertens, F. G., Koopmans, L. V. E., et al. 2020, *mnras*, 499, 4158
- Grobler, T. L., Nunhokee, C. D., Smirnov, O. M., van Zyl, A. J., & de Bruyn, A. G. 2014, *Monthly Notices of the Royal Astronomical Society*, 439, 4030
- Harker, G., Zaroubi, S., Bernardi, G., et al. 2009, *mnras*, 397, 1138
- Haslam, C. G. T., Salter, C. J., Stoffel, H., & Wilson, W. E. 1982, 47, 1
- Haverkorn, M. 2015, *Magnetic Fields in the Milky Way*, ed. A. Lazarian, E. M. de Gouveia Dal Pino, & C. Melioli (Berlin, Heidelberg: Springer Berlin Heidelberg), 483–506
- Hills, R., Kulkarni, G., Meerburg, P. D., & Puchwein, E. 2018, *Nature*, 564, E32–E34

- Hubble, E. 1929, Proceedings of the National Academy of Science, 15, 168
- Hurley-Walker, N., Callingham, J. R., Hancock, P. J., et al. 2017, *mnras*, 464, 1146
- Intema, van der Tol, S., Cotton, W. D., et al. 2009, *A&A*, 501, 1185
- Jelić, V., Zaroubi, S., Labropoulos, P., et al. 2008, *mnras*, 389, 1319
- Kamionkowski, M. 2007, Dark Matter and Dark Energy, arXiv:0706.2986
- Kellermann, K. I., & Pauliny-Toth, I. I. K. 1969, *apjl*, 155, L71
- Kern, Nicholas, G. B. 2018
- Kolopanis, M., Jacobs, D. C., Cheng, C., et al. 2019, *The Astrophysical Journal*, 883, 133
- Koopmans, L. V. E., Pritchard, J., Mellema, G., et al. 2015, The Cosmic Dawn and Epoch of Reionization with the Square Kilometre Array, arXiv:1505.07568
- Krolik, J. H. 1998, *Active Galactic Nuclei: From the Central Black Hole to the Galactic Environment*
- Landecker, T. L., & Wielebinski, R. 1970, *Australian Journal of Physics Astrophysical Supplement*, 16, 1
- Li, R., Frenk, C. S., Cole, S., et al. 2016, *Monthly Notices of the Royal Astronomical Society*, 460, 363
- Linde, A. 2007, *Inflationary Cosmology*, ed. M. Lemoine, J. Martin, & P. Peter (Berlin, Heidelberg: Springer Berlin Heidelberg), 1–54
- Liu, A., & Shaw, J. R. 2020, *Publications of the Astronomical Society of the Pacific*, 132, 062001
- Liu, A., Tegmark, M., Bowman, J., Hewitt, J., & Zaldarriaga, M. 2009, *Monthly Notices of the Royal Astronomical Society*, 398, 401
- Loewenstein, M., & White, R. 1998, *Physics Reports*, 307, 75

- Lonsdale, C. J. 2005, in *Astronomical Society of the Pacific Conference Series*, Vol. 345, From Clark Lake to the Long Wavelength Array: Bill Erickson's Radio Science, ed. N. Kassim, M. Perez, W. Junor, & P. Henning, 399
- Mather, J. C., Cheng, E. S., Cottingham, D. A., et al. 1994, *apj*, 420, 439
- McKinley, B., Yang, R., López-Caniego, M., et al. 2015, 446, 3478
- McMullin, J. P., Waters, B., Schiebel, D., Young, W., & Golap, K. 2007, in *Astronomical Society of the Pacific Conference Series*, Vol. 376, *Astronomical Data Analysis Software and Systems XVI*, ed. R. A. Shaw, F. Hill, & D. J. Bell, 127
- Mertens, F. G., Mevius, M., Koopmans, L. V. E., et al. 2020, *Monthly Notices of the Royal Astronomical Society*, 493, 1662–1685
- Mesinger, A., Furlanetto, S., & Cen, R. 2011, *mnras*, 411, 955
- Mesinger, A., Greig, B., & Sobacchi, E. 2016, *Monthly Notices of the Royal Astronomical Society*, 459, 2342
- Natwariya, P. K., & Bhatt, J. R. 2020, *Monthly Notices of the Royal Astronomical Society: Letters*, 497, L35–L39
- Neben, A. R., Hewitt, J. N., Bradley, R. F., et al. 2016, *The Astrophysical Journal*, 820, 44
- Pacholczyk, A. G. 1970, *Radio astrophysics. Nonthermal processes in galactic and extragalactic sources*
- Paciga, G., Chang, T.-C., Gupta, Y., et al. 2011, *Monthly Notices of the Royal Astronomical Society*, 413, 1174
- Paciga, G., Albert, J. G., Bandura, K., et al. 2013, *Monthly Notices of the Royal Astronomical Society*, 433, 639
- Park, J., Mesinger, A., Greig, B., & Gillet, N. 2019, *Monthly Notices of the Royal Astronomical Society*, 484, 933–949

- Parsons, A. R., Pober, J. C., Aguirre, J. E., et al. 2012, *The Astrophysical Journal*, 756, 165
- Parsons, A. R., Backer, D. C., Foster, G. S., et al. 2010, *aj*, 139, 1468
- Parsons, A. R., Liu, A., Aguirre, J. E., et al. 2014, *The Astrophysical Journal*, 788, 106
- Patil, A. H., Yatawatta, S., Koopmans, L. V. E., et al. 2017, *The Astrophysical Journal*, 838, 65
- Peebles, P. J. E. 1968, *apj*, 153, 1
- Philip, L., Abdurashidova, Z., Chiang, H. C., et al. 2019, *Journal of Astronomical Instrumentation*, 08, 1950004
- Planck Collaboration, Aghanim, N., Akrami, Y., et al. 2018, arXiv e-prints, arXiv:1807.06209
- Poher, J. C., Parsons, A. R., Aguirre, J. E., et al. 2013, *The Astrophysical Journal*, 768, L36
- Poher, J. C., Hazelton, B. J., Beardsley, A. P., et al. 2016, *apj*, 819, 8
- Price, D. C., Greenhill, L. J., Fialkov, A., et al. 2018, *Monthly Notices of the Royal Astronomical Society*, 478, 4193
- Procopio, P., Wayth, R. B., Line, J., et al. 2017, *Publications of the Astronomical Society of Australia*, 34, doi:10.1017/pasa.2017.26
- Rasmussen, C. E., & Williams, C. K. I. 2005, *Gaussian Processes for Machine Learning (Adaptive Computation and Machine Learning)* (The MIT Press)
- Remazeilles, M., Dickinson, C., Banday, A. J., Bigot-Sazy, M. A., & Ghosh, T. 2015, *mnras*, 451, 4311
- Riess, A. G., Casertano, S., Yuan, W., Macri, L. M., & Scolnic, D. 2019, *The Astrophysical Journal*, 876, 85
- Rybicki, G. B., & Lightman, A. P. 1979, *Radiative processes in astrophysics*
- Santos, M. G., Cooray, A., & Knox, L. 2005, *The Astrophysical Journal*, 625, 575

- Sims, P. H., Lentati, L., Alexander, P., & Carilli, C. L. 2016, *Mon. Not. Roy. Astron. Soc.*, 462, 3069
- Singh, S., & Subrahmanyan, R. 2019, *The Astrophysical Journal*, 880, 26
- Singh, S., Subrahmanyan, R., Shankar, N. U., et al. 2017, *The Astrophysical Journal*, 845, L12
- . 2018, *The Astrophysical Journal*, 858, 54
- Smeenk, C., & Ellis, G. 2017, in *The Stanford Encyclopedia of Philosophy*, winter 2017 edn., ed. E. N. Zalta (Metaphysics Research Lab, Stanford University)
- Smirnov, O. M. 2011, *aap*, 527, A107
- Storey, W. V., J., C. B. Ashley, M., Naray, M., & Lloyd, J. 1994, *American Journal of Physics - AMER J PHYS*, 62, 1077
- Thompson, A. R., Moran, J. M., & Swenson Jr, G. W. 2008, *Interferometry and synthesis in radio astronomy* (John Wiley & Sons)
- Thyagarajan, N., Carilli, C., & Nikolic, B. 2018, *Phys. Rev. Lett.*, 120, 251301
- Thyagarajan, N., & Carilli, C. L. 2020, *Physical Review D*, 102, doi:10.1103/physrevd.102.022001
- Thyagarajan, N., et al. 2013, *Astrophys. J.*, 776, 6
- Thyagarajan, N., Carilli, C. L., Nikolic, B., et al. 2020, *Physical Review D*, 102, doi:10.1103/physrevd.102.022002
- Trott, C. M., Pindor, B., Procopio, P., et al. 2016, *The Astrophysical Journal*, 818, 139
- Trott, C. M., Jordan, C. H., Midgley, S., et al. 2020, *Monthly Notices of the Royal Astronomical Society*, 493, 4711
- Van Haarlem, M. P., Wise, M. W., Gunst, A. W., et al. 2013, *aap*, 556, A2

Wang, J., Xu, H., An, T., et al. 2013, *The Astrophysical Journal*, 763, 90

Wang, T., Elbaz, D., Daddi, E., et al. 2016, *The Astrophysical Journal*, 828, 56

Wang, X., Tegmark, M., Santos, M. G., & Knox, L. 2006, *apj*, 650, 529

Wijnholds, S. J., Grobler, T. L., & Smirnov, O. M. 2016, *Monthly Notices of the Royal Astronomical Society*, 457, 2331

Wouthuysen, S. A. 1952, *aj*, 57, 31

Yatawatta, S. 2010, 2010 IEEE Sensor Array and Multichannel Signal Processing Workshop, SAM 2010, doi:10.1109/SAM.2010.5606769

Yatawatta, S., de Bruyn, A. G., Brentjens, M. A., et al. 2013, *aap*, 550, A136

Zeldovich, Y. B. 1972, *Monthly Notices of the Royal Astronomical Society*, 160, 1P

Zhao, J.-H., Morris, M. R., & Goss, W. M. 2019, *The Astrophysical Journal*, 875, 134

Zonca, A., Singer, L., Lenz, D., et al. 2019, *Journal of Open Source Software*, 4, 1298

Zwicky, F. 1933, English and Spanish Translation of Zwicky's (1933) *The Redshift of Extragalactic Nebulae*, arXiv:1711.01693